DISSERTATION

ROTOR POSITION SYNCHRONIZATION CONTROL METHODS IN CENTRAL-CONVERTER MULTI-MACHINE ARCHITECTURES WITH APPLICATION TO AEROSPACE ELECTRIFICATION

Submitted by

Cláudio de Andrade Lima

Department of Electrical and Computer Engineering

In partial fulfillment of the requirements

For the Degree of Doctor of Philosophy

Colorado State University

Fort Collins, Colorado

Summer 2024

Doctoral Committee:

Advisor: James Cale

Edwin Chong
Daniel Herber
Michael Kirby

ABSTRACT

ROTOR POSITION SYNCHRONIZATION CONTROL METHODS IN CENTRAL-CONVERTER MULTI-MACHINE ARCHITECTURES WITH APPLICATION TO AEROSPACE ELECTRIFICATION

With the continuous advancement of the aerospace industry, there has been a significant shift towards More Electric Aircraft (MEA). Some of the advantages of the electrification of some actuation systems in an aircraft include lower weight — hence, lower fuel consumption, — robustness, flexibility, ease of integration, and higher availability of sensors to achieve better diagnostics of the system. One cannot ignore the challenges of the electrification process, which encompasses finding appropriate hardware architectures, and control schemes, and obtaining at least the same reliability as traditional drives.

The thrust reverser actuation system (TRAS), which acts during landing to reduce the necessary runway for the aircraft to fully decelerate, has a big potential to be replaced by an electromechanical version, the so-called EM-TRAS. Among the different hardware architectures, the central-converter multi-machine (CCMM) stands out for employing a single power converter that drives multiple machines in parallel, saving weight and room usage inside the aircraft. This solution comes with its challenges related to the requirement of ensuring position synchronization among all the machines, even under potentially unbalanced mechanical loads. Since there is only one central converter, all the machines are subject to its common output, limiting the control independence of each machine. Moreover, the lack of position synchronization among the machines can cause harmful stresses to the mechanical structure of the EM-TRAS.

This work proposes a solution for position synchronization under CCMM architectures, for aerospace applications. The proposed method utilizes three-phase external and variable resistors connected in series with each of the machines, which increases the degrees of freedom (DOF)

to control independently each machine under different demands. Mathematical modeling for the different components of the system is presented, from which the proposed solution is derived. Numerical simulations are used to show the working capabilities of the external resistor method. The performance of the position synchronization is enhanced via H-infinity control design methods. Hardware experiments are also presented, obtained from an experimental testbed that was partially designed and constructed during this work. Both numerical and experimental results are in agreement. Initial findings show that the method is promising and works well under some operating conditions. However, some limitations of the method are presented, such as the unstable operation under negative loads.

An alternative position synchronization method for CCMM systems is proposed at the end of this work. The method is based on independently controlled induced voltages on each machine's power cables through low-power auxiliary converters and three-phase compact transformers, resulting in independent terminal voltages applied to each machine. This work describes the method and validates it through numerical simulations. Initial findings show that the method overcomes some of the limitations of the external resistors method, while keeping – and, in some cases, improving – the overall performance in terms of convergence time and peak position error.

ACKNOWLEDGEMENTS

A wise man once said

> "In a piece of paper where one reads from top to bottom and from left to right, one mistakenly assigns more importance to what is positioned towards the top and left. Let it be noted that the order of the following statements is irrelevant; this order is merely a product of the paper on which I write."

I just can't find a reason to refute it.

Prof. Cale, my advisor, my teacher, my professor, my mentor, my academic foster father, my friend – thank you for everything. I should make this short but is not possible to use such a small piece of paper to describe what "everything" really means. Even if I had all the hundreds of pages of this whole document, it would still not be enough. So, I'll content myself with a plain and simple "thank you". I'm sure you know the gigantic number of meanings – both explicit and hidden – encompassed by these two words. Thank you, thank you, and thank you!

Prof. Chong – you were one of those unexpected encounters we have in life, a bump in the subway, an accidental trip while waiting in line, an unpretentious nod on the street. Thank you for sharing with me some of your vast and eclectic knowledge. Thank you for the deep conversations, for listening, for making me feel important. Thank you for showing me that even the greatest – like you – have doubts, fail, and learn from it, with no sign of pique. I'm ever grateful for our fortuitous encounter.

Mom and Dad – again, this whole thing is only a reality because you give all your body and soul to whatever Joca and I decide to put our minds to. Thank you for the insane efforts you devote to us. Thank you for coming twice. Thank you for bringing that piece of me that always stayed – and always will be – in Brazil. Again, one more finished and dedicated to you, as everything I do in life.

Arthur and Roberta – thank you for opening all the doors for us, from that car door in the airport when you went to pick us up three years ago, to your home door. The keys to open CSU doors were given to us by you, our beloved key-master friends.

Karla – my partner, my confidant. Only you know the whole thing. Only you know what happened. Only you were here the whole time. The raw reality, naked and deprived of any hint of romanticism – that was our third partner, and ours alone. Thank you for being there every minute, for supporting me in my falls, for nursing my wounds, for cheering and celebrating my accomplishments together, for never stopping believing in me. Thank you for embracing this journey with me. My love is yours.

CEFET-MG is my first home. Thank you for letting me experience such a privileged journey. I'm coming back to tell you how it was.

CSU is now my third home, my green and flat and warm and calm and idyllical place where never-before-imagined adventurous took place. I'll be back for a visit or two, you can count on that. Thank you!

Woodward, who accepted me, taught me a lot, and helped fund my studies – thank you!

For all the ones who didn't make it to these pages, I'll quote another piece of thought by that wise man from the beginning:

> "To wait is to suffer, to realize is to joy, to feel all of that is to live, indeed."

You can be sure that I realize how important you were and how grateful I am that you were part of it. Thank you!

DEDICATION

To my mom,

to my dad.

To them, everything.

TABLE OF CONTENTS

LIST OF TABLES

LIST OF FIGURES

Chapter 1

Introduction

1.1 Motivation

Over the past few decades, the transportation sector has become increasingly electrified [1–5]. This movement towards electrification has been largely enabled by power-electronic drives, energy storage, and advanced control of rotating electrical machinery [1–4, 6, 7]. The transition from mechanical (e.g., pneumatic or hydraulic) drives to full- or hybrid-electric drives – already seen in naval and vehicle transportation – is expected to revolutionize the aerospace industry in coming years [1,2,5–8]. The trend towards More Electric Aircraft (MEA) for aerospace applications is partially inspired by the potential for reduced weight (with associated fuel impacts) and maintenance of existing mechanical drive systems.

As an example of the electrification trend in the aerospace industry, electromechanical drive alternatives are currently being considered as a replacement to pneumatic and/or hydraulic thrust reverse actuation systems (TRAS) in future aircraft [8–10]. The purpose of a TRAS is to provide deceleration of the aircraft on the runway, particularly after touchdown. This deceleration is accomplished by extending/retracting mechanical members housed in the nacelle to divert the flow of exhaust so that thrust opposes motion. An example of a mechanical TRAS using a 'pivoting-door' concept is depicted in Fig. 1.1. In Fig. 1.1, f_t represents the forward thrust of the aircraft; f_d represents the equivalent drag force produced by the doors, which are extended/retracted by the actuators; f_{tr} is the redirected thrust force that acts to help the aircraft to slow down faster when the doors are opened.

Although there are different design implementations for TRAS, a critical aspect of any TRAS design is that the aerodynamic and structural characteristics (e.g., flexibility) of the nacelle may result in the extended members being subjected to unequal drag forces. For this reason, TRAS are typically designed so that each member may be extended with an independently-controlled

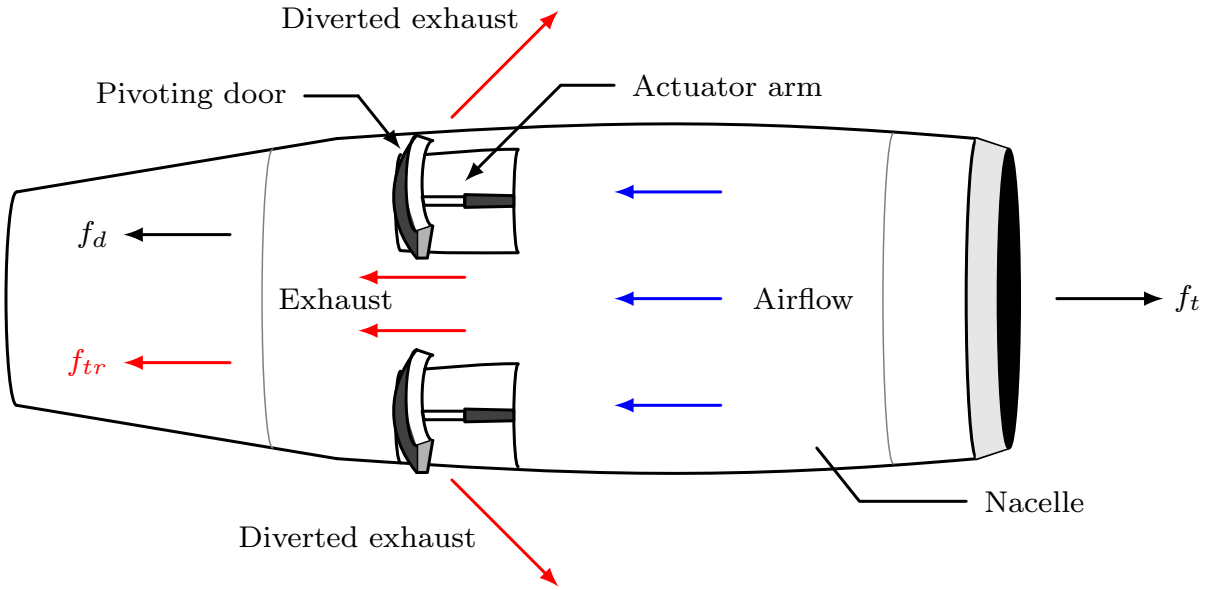

Figure 1.1: Notional illustration of pivoting-door TRAS.

compensating force by its actuator that results in a synchronous extension of all members, resulting in a more uniform net drag force on the nacelle.

Electromechanical thrust reverse actuation systems, EM-TRAS, refers herein to a means of providing reverse thrust in aircraft where actuation is accomplished using a combination of electrical and mechanical components. Electrical components include power-electronic drives, electrical motors, and possibly energy storage; mechanical components include gear-trains and actuators. The principle difference between EM-TRAS and traditional (i.e., fully mechanical) TRAS is that the primary actuation force is provided by electromagnetic force/torque rather than hydraulic or pneumatic force. For this reason, EM-TRAS may offer several potential advantages including (*a*) the elimination of maintenance tasks and costs associated with servicing hydraulic fluid or pneumatic air lines (*b*) reduced weight and (*c*) increased controllability and diagnostics from additional electrical sensing and controls available in power-electronic drives. However, to serve as a viable alternative, EM-TRAS must provide equivalent or better functional performance, safety, and reliability than traditional TRAS.

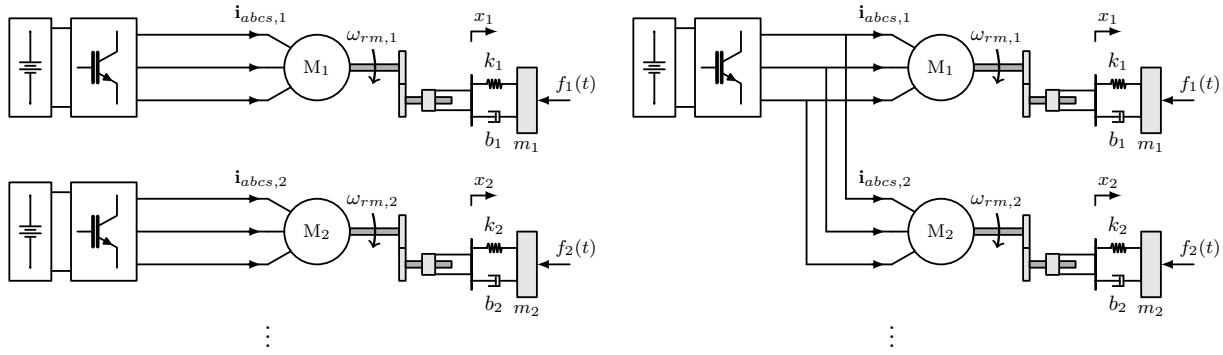

(a) DCMM architecture.

(b) CCMM architecture.

Figure 1.2: Notional depiction of DCMM (a) and CCMM (b) architecture.

Several possible electrical architectures and electrical motor types could be used to implement EM-TRAS. Perhaps the most direct approach for EM-TRAS is to provide one electromechanical actuator subsystem (EAS) per extending/retracting member. In this context, EAS refers to a (sub)system comprised of a power-electronic converter, single electrical motor, and mechanical drive. The power-electronic converter provides alternating current (AC) to the stator windings of the motor; the motor produces an electromagnetic torque and angular speed/position; the mechanical drive converts the motor output shaft rotation into a linear displacement that drives the mechanical load. Because each motor is driven by its own converter, this architecture is referred to herein as the distributed converter multiple-motor (DCMM) architecture, depicted in Fig. 1.2a.

In Fig. 1.2a, $\mathbf{i}_{abcs,n}$ is the set of three-phase stator currents, $\omega_{rm,n}$ the mechanical angular velocity, x_n the linear position, k_n the equivalent spring constant, b_n the equivalent damping constant, m_n the equivalent mass, and $f_n(t)$ the equivalent input force for actuation line $n \in \mathcal{N}$, where $\mathcal{N} = \{1, 2, \ldots, N\}$ is the set of actuation line numbers.

Alternatively, another architecture employs a single ("central") power-electronic converter to simultaneously control the parallel set of motors, thereby eliminating the cost and space needed for distributed converters, as depicted in Fig. 1.2b. In this approach, herein called the central-converter multi-motor (CCMM) architecture, the trade-off for the reduced number of converters is that the CCMM drive must be able to control the motors simultaneously to meet the (generally unequal) load torques while maintaining required position synchronization. An additional design

consideration is the type of electrical motor used in the EM-TRAS; several types of synchronous or asynchronous motors could be used for this application. However, the asynchronous induction machine (IM) is a physically robust and low-cost alternative which makes it a desirable candidate for EM-TRAS and is, therefore, the type of motor examined in this research.

The main problem investigated in this work is the speed and position synchronization of multiple IMs within a CCMM architecture. A novel method to achieve synchronization using controllable stator resistors is proposed. The method is described and validated via simulation results and experimental tests. Its performance is evaluated in terms of maximum position error and convergence time. This work also proposes an optimal control design to improve the synchronization method performance using the $\mathcal{H}_\infty$ method. The $\mathcal{H}_\infty$ control design method [11] is used to solve an optimal control synthesis problem to determine the best-stabilizing controller for the CCMM plant model, resulting in an optimal closed-loop response in terms of tracking error (e.g., normed rotor position error) and disturbance rejection (e.g., load torques). The approach employs linearized IM models and a selection of plant weighting functions. Both non-optimal and optimal controls are compared through switch-level, time-domain numerical simulation.

An alternative position synchronization method for CCMM systems is proposed at the end of this work. The so-called "voltage-boost" method possesses an extra level of flexibility compared to the "controllable stator resistors" and some practical implementation benefits. The method is described, and different case studies performed through numerical simulations demonstrate the method's operation.

1.2 Contributions

The key contributions of this work are as follows:

1. Introduction of a novel control strategy for achieving simultaneous speed and position synchronization in a set of parallel IMs with unequal torque loads within a CCMM architecture;

2. Proposal of an optimal control synthesis to improve the performance of the novel synchronization control strategy;

3. Description of the IM linearization process and weighting function selections for the modified plant model;

4. Validation of the control approach in several case studies, demonstrating position synchronization error being driven to zero using both voltage-based and current-based primary control strategies;

5. Comparison between non-optimal and optimal control strategies using detailed numerical case studies;

6. Description of a testbed that was designed and constructed to support the development and validation of new architectures and control algorithms for aerospace electromechanical actuation system alternatives;

7. Presentation of hardware validation of the new aerospace actuation testbed;

8. Proposal of a potentially low-cost, low-weight, and robust architecture and control for implementation of EM-TRAS for future aircraft;

9. Introduction of an alternative position synchronization method for CCMM systems, presented as the voltage-boost method;

10. Validation of the alternative method through numerical simulations.

This research has led so far to five publications, as described below:

1. C. d. A. Lima, J. Cale, and K. E. Shahroudi, "Rotor position synchronization in central-converter multi-motor electric actuation systems," *Energies*, vol. 14, no. 22, 2021 [12].

2. C. Lima, et. al., "Testbed for emulation of aerospace actuation systems," in *Pipeline Research Council International (PRCI) Meeting*, Fort Collins, CO (USA), May 10, 2022 [13].

3. C. Lima and J. Cale, "Rotor position synchronization control in central-converter multi-motor topologies," in I*EEE Power and Energy Systems General Meeting*, 2022, Denver, CO (USA), July 17-21, 2022 [14].

4. C. Lima, et. al., "A novel electromechanical actuation testbed for emulation of aerospace actuation systems," in *33rd Aerospace Testing Seminar*, El Segundo, CA (USA), May 15, 2023 [15].

5. C. Lima and J. Cale, "Control design for position synchronization in central converter multi-machine actuators," in *Proc. of the International Conference on Electrical, Computer, Communications and Mechatronics Engineering (ICECCME 2023)*, Tenerife, Spain, July 19-21, 2023 [16].

6. C. Lima, C. Lute, and J. Cale, "Experimental Validation of Rotor Position Synchronization Control in Central-Converter Multi-Motor Architectures for Aerospace Applications'," in *Proc. of the IEEE Energy Conversion Congress & Expo (ECCE 2024)*, Phoenix, USA, Oct. 20-24, 2024 (*accepted, to appear*).

1.3 Dissertation Structure

This dissertation is structured within seven chapters, including this introductory one. Chapter 2 provides a review of the literature regarding multi-motor control strategies. Chapter 3 gives an overview of the main technical topics discussed throughout this dissertation, such as induction machines and their control strategies, and the $\mathcal{H}_\infty$ control design method. Chapter 4 presents a novel method for achieving speed and position synchronization of multiple IMs within a CCMM architecture. It also develops the framework necessary for applying the $\mathcal{H}_\infty$ control design method to the system under investigation. Chapter 5 shows numerical results used to validate the proposed control method and the optimal control design. Chapter 6 describes the new aerospace actuation testbed and experimental results. In Chapter 7, an alternative position synchronization method is described, and numerical results are presented to demonstrate the effectiveness and performance of the method. Finally, Chapter 8 concludes the dissertation and presents future work perspectives.

Chapter 2

Literature Review

Prior research investigating multi-motor control approaches using DCMM and CCMM architectures has been broadly discussed in the literature. What follows is a review of the most relevant works that address this topic.

In [17], the authors address the transient and steady-state torque production of each 3-phase induction motor (IM) drive with parallel connected stator windings fed by a single power converter. Typical application for that kind of control is in electrical vehicles. The expected benefits are a simple drive train design (no mechanical differential required); traction and regenerative braking control; lower cost and smaller size compared to a two inverter, two IM alternative. The authors were probably the first to address the issue of two IM driven by a single power converter, with different load conditions. They used a simple approach to control average and/or differential variables, such as torque, rotor flux, and rotor velocity. The results shown are relevant and promising since they indicate the technique worked. However, since it was one of the first papers about it, some things were left without being explored, such as the difference in parameters of the motors; implementation of closed-loop speed control, instead of a torque command, to verify speed and position synchronization issues; applications where more than two IM are being controlled by the same power converter.

The authors in [18] propose a new technique to control the speed of two motors connected in parallel to a single power converter, using vector control. They use adaptive rotor flux and speed observers to eliminate sensors. The proposed technique is compared to a conventional method. The authors present several results for unbalanced load tests and commanded speed. The proposed technique does not require speed and flux sensors, as it uses observers. Moreover, the speed response is not unstable, as observed for the conventional method. One limitation is that the speeds do not follow the commanded values under unbalanced load conditions.

The work presented in [19] analyzes the dynamic model of combined electrical, mechanical, and control system of a bogie of a train traction system using Simulink. The bogie consists of two induction motors driven by a single power converter, each motor driving one axle (rear and front). The work compares the conventional method and the proposed one: weighted vector control to control speed. The employment of vector control is justified by the fast acceleration and deceleration requirements of a drive train, and vector control can provide quick and accurate motor torque response. The work shows simulation results for the two control methods in a drive train system. After acceleration, train speed is commanded to a fixed value. Unbalanced load torque in both motors is forced by changing the adhesion coefficient in the front wheels, a condition that simulates the train going out of a tunnel on a rainy day. For the conventional method, the system becomes unstable after the unbalanced load torque condition. For the proposed method, stability is achieved, since the control adapts itself by commanding more torque to the second motor. This results in the train maintaining the desired speed, while the motors' speeds and torques are different. The proposed method benefits from having an inherent anti-slip control. However, the method does not achieve speed synchronization of both motors for unbalanced load torque conditions, even though the train's linear speed follows the commanded set point.

The focus of the work presented in [20] is to analyze and compare multi-machine field-oriented control methods from the standpoint of dynamic performance. The work performs a small-signal analysis and verifies it through simulations and experiments. It is considered a drive comprised of a single power converter feeding two identical parallel-connected three-phase induction motors, with differences in their mechanical loads, which prevents both motors from being field-oriented simultaneously. Two different control strategies are compared: master-slave and mean control. The dynamics of the resulting transfer functions are evaluated via step change and eigenvalues analysis. The results are compared with numerical simulation and experimental results. Different rated machines are used in the studies, which result in valid and consistent characteristics for each scenario. The main limitations of the work are: speed control loop is not considered, since the authors argue the focus is on the torque response, which is faster than the speed response; loads on

the machines are considered constant, although different for each motor; the work uses a symbolic mathematics package to evaluate the transfer functions and does not show them, despite presenting a considerable work to obtain them; it also does not investigate speed synchronization problem, since the focus is on torque response.

The goal in [21] is to propose a new method for controlling speed and torque of two motors using a single power converter. It is used a matrix converter combined with direct torque control, space vector modulation (DTC-SVM), with an additional flux dead-beat scheme. The proposed method seeks to reduce torque ripple, maintain speed stability under unbalanced load conditions, and obtain unit input power factor. The authors compare the proposed DTC-SVM method with conventional DTC via simulations using $200\,\text{hp}$ induction motors. The results showed that the proposed method reduced torque and current ripple while attaining unit input power factor. The proposed method also resulted in a slightly faster response compared to the conventional method and kept both motors at approximately reference speed, even for unbalanced load conditions. However, speed synchronization is not achieved, in spite of being more difficult to implement, in the authors' words.

Applications such as electric traction and steel processing sectors demand multiple motors in parallel operation fully controlled by a single power converter. Unbalanced load conditions can arise if the machines have dissimilar characteristics or unequal couple-wheel diameters, for example. This can lead to speeds deviating from the commanded values. This is the motivation presented by the series of works in [22–26]. They all share the same goal, which is to apply vector control to control the speed of two induction motors using a single power converter. Vector control of the induction motors is carried out to control the averages of flux and torque. Sensorless speed control is proposed under the justification of equipment reliability, cost-effectiveness, and less maintenance since this kind of control dismisses the use of speed sensors. To achieve sensorless speed control, a "natural" observer is proposed to estimate speed and other variables of interest. The observer is based on the electrical real power of the motors to estimate load torques, which in turn are used for speed estimation. Simulation and experimental tests are performed

to assess the performance of the proposed observer and the vector control. The results are also compared with the use of different observers, such as Kubota's method [27, 28] and conventional adaptive observer. In general, the results presented in the papers show that the proposed observer successfully estimates key variables of the motor, such as torques, currents, and speeds. The results in [22], for example, show that the proposed observer is both accurate and stable, and outperforms Kubota's method in terms of transient response. The work in [23] demonstrates the robustness and efficiency of the vector control using the proposed observer. Variations in the motors' stator resistance and in the DC power supply are considered in the simulation tests. The experimental results in [24–26] further validate the performance of the natural observer and of the vector control of two induction motors fed by a single power converter. In [24], speed deviation was reduced under unbalanced load conditions using the proposed observer when compared to a conventional adaptive observer. However, except for [26], all the works in this series were not able to achieve speed synchronization under unbalanced load conditions.

It is worthwhile exploring the results presented in [26]. The work uses a natural observer to estimate speed, rotor flux, and load torque, and a direct field-oriented vector control to control the average torque and flux of both motors. An experimental set-up was carried out using two $1\,\mathrm{hp}$ induction motors controlled with direct field-oriented sensorless control and estimated rotor flux to accomplish field orientation. For unbalanced load condition, where one motor is kept with no-load and the other with 80% of rated torque, it is firstly shown that the *estimated* speed of the loaded motor drops, but after a while it goes back to the commanded value, even when unbalanced load condition is kept. However, it is not clear if the actual speed presented the same behavior, or if it was just the estimated one. If the former is true, it seems that this work managed to solve the speed synchronization problem.

In [29], the authors propose an electronic (virtual) line-shafting (EVLS) that dismisses the conventional mechanical line-shaft. Each mechanical section of a sectional drive system is driven by a drive with an individual motor and control. The work aims to improve existing electronic line shafting to cope with severe load disturbances and current limiting while keeping speed synchro-

nization. Experimental tests were performed on a four-section mechanical setup. It is demonstrated that the system response to loads is fast and that the angular error between different sections is low. The proposed technique, whose control topology is quite simple, managed to maintain speed synchronization under changes in speed reference, current limiters, and disturbance load torques. However, the system is based on a DCMM topology, where each motor has its own power converter.

The works in [30, 31] are motivated by industrial applications such as paper machines, offset printing, and textiles that make use of multi-motor drive systems. In [31], a novel EVLS topology is proposed, and both simulation and experimental tests are performed. The work modifies the classic EVLS (shown in [29]) in order to achieve equal speed response and zero relative position angles for all motors, in the initial transient response and under load torque disturbances. The proposed method resulted in a considerable improvement in the position synchronization response. The position error is zero at steady-state, even under unbalanced load conditions (which was not achieved in [29]), and the maximum and minimum error values, in load steps, are significantly reduced. This improvement is accounted for by the included position PI controllers in parallel for each motor. Experimental tests were also performed, with faster speed response and lower position synchronization error. The structure proposed is simpler than the classic EVLS. The work in [30] compares several synchronization techniques, such as master-slave, cross-coupling, bi-axial cross-coupled control method, EVLS, and relative coupling strategy. Both simulation and hardware results are presented, showing the methods' ability to synchronize the speed of two induction motors. However, the drive topology employed for all the methods is based on DCMM, where each motor is driven by an individual power converter.

In the context of electric vehicles and traction systems, the works in [32, 33] propose a "smart switching" technique to independently control the speed of two motors with a single power converter. Two different speed control strategies were tested, Volts-per-Hertz (VHz) [32] and indirect field-oriented control (IDFOC) [33]. Using three-phase switches in series with each motor, the motors were connected/disconnected to the central power converter in each sample period. Simu-

lation results showed that the technique accomplished maintaining speed control under unbalanced torque load conditions, with the motors given independent speed commands. A drawback is the high ripple in the electromagnetic torque for both motors. Additionally, the "smart switching" technique requires additional electronic switches to break the connection between the motors and the central converter. Moreover, the work in [32,33] did not demonstrate position synchronization, which is the chief focus of this dissertation.

A patent that proposes a method to attain a synchronous (or a near synchronous) operation in some aircraft actuators is presented in [34]. The distributed electromechanical actuators are driven by a single drive with a common bus. These actuators act on primary (such as elevators, rudder, and ailerons) and secondary (such as flaps, slats, and spoilers) flight control surfaces. The method relies on the steep behavior of the torque vs. speed characteristic of induction motors and uses an open-loop VHz strategy control. It is based on the fact that near the synchronous speed, the motor speed will vary only about 2% when load torque is applied. The main contribution is that the patent proposes a method to replace conventional actuators (such as hydraulic) with distributed electromechanical actuators driven by a central converter. The proposed method is quite simple, relying only on the induction motor's natural characteristics to attain speed synchronization. There are no closed-loop control and control parameters to be tuned. The only concern is with speed synchronization and not position. However, the synchronization proposal is rather poor, since there is no closed-loop control, and the speed synchronization relies on the motor's natural behavior (steep torque vs. speed characteristic near synchronous speed).

As demonstrated, none of the prior literature has described simultaneous speed and position synchronization of IMs in a CCMM architecture with unequal load torques.

Chapter 3

Technology Background

This chapter provides background about induction machines, and induction machine drives and control systems. It also presents a brief overview of more advanced control design methods, like the $\mathcal{H}_\infty$.

3.1 Induction Machines and Control Drives

This section provides a brief background on IMs, followed by two commonly-employed IM control strategies, a voltage-control, and a current-control strategy.

3.1.1 Induction Machines

The IM can operate as a motor or generator (its application as a motor is the focus of this research). It is composed of stationary stator windings and rotor windings mounted inside the rotor. The rotor shaft has roller bearings on both ends, which allows the rotor to rotate while providing a fixed air gap distance between stator and rotor. Fig. 3.1 illustrates a cross-sectional view of a three-phase, two-pole IM. The outside portion is the stator, which contains sinusoidally-distributed windings with peak turns displaced by $120°$. For phase a, denoted as and as', current enters into the page at as (designated by crosses) and exits at as' (designated by dots), and similarly for other stator and rotor windings. In this work, it is assumed that the rotor windings consist of short-circuited rotor bars ("squirrel-cage" rotor). The arrows in Fig. 3.1 correspond to the primary magnetic axes of the windings, corresponding to the location of peak magnetic flux for assumed positive current. In Fig. 3.1, the rotational "electrical" angular velocity, ω_r, is related to (actual) mechanical angular velocity, ω_{rm}, as $\omega_r = (P/2)\omega_{rm}$ where P is the number of magnetic poles. Electrical angular position θ_r is:

$$\theta_r = \int_0^t \omega_r(\tau)\, d\tau + \theta_r(0), \tag{3.1}$$

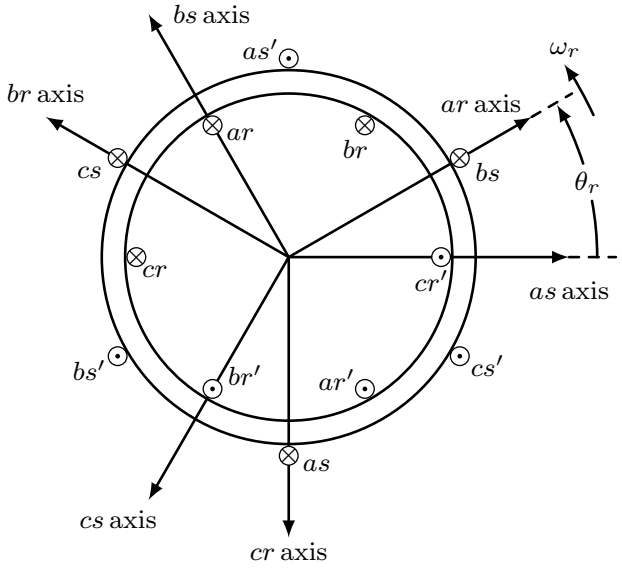

Figure 3.1: Cross-section of a three-phase, two-pole induction machine.

where $\theta_r(0)$ is the initial electrical angular position. Voltage equations for the IM with external stator resistances in series with each winding are expressed as:

$$\mathbf{v}_{abcs} = (\mathbf{r}_s + \mathbf{r}_e)\,\mathbf{i}_{abcs} + p\boldsymbol{\lambda}_{abcs} \tag{3.2a}$$

$$\mathbf{v}_{abcr} = \mathbf{r}_r \mathbf{i}_{abcr} + p\boldsymbol{\lambda}_{abcr}, \tag{3.2b}$$

where $\mathbf{v}_{abcs(r)}$, $\mathbf{i}_{abcs(r)}$, and $\boldsymbol{\lambda}_{abcs(r)}$ are stator (rotor) voltage, current and flux linkages vectors, respectively; $\mathbf{r}_s, \mathbf{r}_e, \mathbf{r}_r$ are resistance matrices for the stator windings, external stator resistances, and rotor windings, respectively, expressed as:

$$\mathbf{r}_s = \begin{bmatrix} r_s & 0 & 0 \\ 0 & r_s & 0 \\ 0 & 0 & r_s \end{bmatrix}, \quad \mathbf{r}_e = \begin{bmatrix} r_e & 0 & 0 \\ 0 & r_e & 0 \\ 0 & 0 & r_e \end{bmatrix}, \quad \mathbf{r}_r = \begin{bmatrix} r_r & 0 & 0 \\ 0 & r_r & 0 \\ 0 & 0 & r_r \end{bmatrix}, \tag{3.3}$$

where r_s, r_e, r_r are the scalar resistances of the stator windings, external resistors, and rotor windings, respectively. As indicated in (3.3), it is assumed herein that each winding of the stator, each

of the external resistors, and each winding of the rotor have equal resistance values on all electrical phases (although generally $r_s \neq r_e \neq r_r$).

Flux linkages in (3.2) for the motor depicted in Fig. 3.1 are expressed as:

$$\boldsymbol{\lambda}_{abcs} = \mathbf{L}_s \mathbf{i}_{abcs} + \mathbf{L}_{sr} \mathbf{i}_{abcr} \tag{3.4a}$$

$$\boldsymbol{\lambda}_{abcr} = \mathbf{L}_r \mathbf{i}_{abcr} + \mathbf{L}_{sr}^T \mathbf{i}_{abcs}, \tag{3.4b}$$

where the self inductance matrices, $\mathbf{L}_s, \mathbf{L}_r$, respectively, are:

$$\mathbf{L}_s = \begin{bmatrix} L_{ls} + L_{ms} & -\frac{1}{2}L_{ms} & -\frac{1}{2}L_{ms} \\ -\frac{1}{2}L_{ms} & L_{ls} + L_{ms} & -\frac{1}{2}L_{ms} \\ -\frac{1}{2}L_{ms} & -\frac{1}{2}L_{ms} & L_{ls} + L_{ms} \end{bmatrix}, \tag{3.5}$$

$$\mathbf{L}_r = \begin{bmatrix} L_{lr} + L_{mr} & -\frac{1}{2}L_{mr} & -\frac{1}{2}L_{mr} \\ -\frac{1}{2}L_{mr} & L_{lr} + L_{mr} & -\frac{1}{2}L_{mr} \\ -\frac{1}{2}L_{mr} & -\frac{1}{2}L_{mr} & L_{lr} + L_{mr} \end{bmatrix}, \tag{3.6}$$

where L_{ls}, L_{lr} are the stator and rotor leakage inductances, respectively; L_{ms}, L_{mr} are the stator and rotor magnetizing inductances, respectively. The mutual inductance matrix is expressed as:

$$\mathbf{L}_{sr} = L_{sr} \begin{bmatrix} \cos\theta_r & \cos\left(\theta_r + \frac{2\pi}{3}\right) & \cos\left(\theta_r - \frac{2\pi}{3}\right) \\ \cos\left(\theta_r - \frac{2\pi}{3}\right) & \cos\theta_r & \cos\left(\theta_r + \frac{2\pi}{3}\right) \\ \cos\left(\theta_r + \frac{2\pi}{3}\right) & \cos\left(\theta_r - \frac{2\pi}{3}\right) & \cos\theta_r \end{bmatrix} \tag{3.7}$$

where L_{sr} is the amplitude of the mutual inductance between stator and rotor windings. To eliminate the angular dependence in the machine equations arising from (3.7), transformation of the equations to a rotating reference frame is employed. Transformation of the stationary variables to

$qd0$ variables in the arbitrary rotating reference frame is achieved by the transformation:

$$\mathbf{f}_{qd0s} = \mathbf{K}_s \mathbf{f}_{abcs}, \tag{3.8}$$

where $\mathbf{f}$ can represent voltage, current, or flux linkage, and matrix $\mathbf{K}_s$ is defined as:

$$\mathbf{K}_s := \frac{2}{3} \begin{bmatrix} \cos\theta & \cos\left(\theta - \frac{2\pi}{3}\right) & \cos\left(\theta + \frac{2\pi}{3}\right) \\ \sin\theta & \sin\left(\theta - \frac{2\pi}{3}\right) & \sin\left(\theta + \frac{2\pi}{3}\right) \\ \frac{1}{2} & \frac{1}{2} & \frac{1}{2} \end{bmatrix}, \tag{3.9}$$

where the arbitrary reference frame position angle is computed as:

$$\theta = \int_0^t \omega(\tau)\, d\tau + \theta(0), \tag{3.10}$$

where ω is the speed of the reference frame and $\theta(0)$ is its initial angular position.

Transformation of the rotor variables to $qd0$ variables in the arbitrary rotating reference frame is performed by the transformation:

$$\mathbf{f}_{qd0r} = \mathbf{K}_r \mathbf{f}_{abcr}, \tag{3.11}$$

where $\mathbf{K}_r$ is defined as:

$$\mathbf{K}_r := \frac{2}{3} \begin{bmatrix} \cos(\beta) & \cos\left(\beta - \frac{2\pi}{3}\right) & \cos\left(\beta + \frac{2\pi}{3}\right) \\ \sin(\beta) & \sin\left(\beta - \frac{2\pi}{3}\right) & \sin\left(\beta + \frac{2\pi}{3}\right) \\ \frac{1}{2} & \frac{1}{2} & \frac{1}{2} \end{bmatrix}, \tag{3.12}$$

where $\beta := \theta - \theta_r$. An additional step is the referral of variables based on the turns ratio between stator and rotor windings; herein the voltage, flux linkages, currents and electrical parameters of

the rotor are referred to the stator side as:

$$\mathbf{v}'_{qdr} = \frac{N_s}{N_r}\mathbf{v}_{qdr} \tag{3.13a}$$

$$\boldsymbol{\lambda}'_{qdr} = \frac{N_s}{N_r}\boldsymbol{\lambda}_{qdr} \tag{3.13b}$$

$$\mathbf{i}'_{qdr} = \frac{N_r}{N_s}\mathbf{i}_{qdr} \tag{3.13c}$$

$$\mathbf{r}'_r = \left(\frac{N_s}{N_r}\right)^2 \mathbf{r}_r \tag{3.13d}$$

$$\mathbf{L}'_{lr} = \left(\frac{N_s}{N_r}\right)^2 \mathbf{L}_{lr}, \tag{3.13e}$$

where N_s, N_r are the equivalent turns of the stator and rotor windings, respectively. After transformation of (3.2)-(3.4) to the arbitrary rotating reference frame using (3.8)-(3.12) and referral of variables from (3.13), the voltage equations in qd variables are expressed as:

$$v_{qs} = (r_s + r_e)\, i_{qs} + \omega\lambda_{ds} + p\lambda_{qs} \tag{3.14a}$$

$$v_{ds} = (r_s + r_e)\, i_{ds} - \omega\lambda_{qs} + p\lambda_{ds} \tag{3.14b}$$

$$v'_{qr} = r'_r i'_{qr} + (\omega - \omega_r)\lambda'_{dr} + p\lambda'_{qr} \tag{3.14c}$$

$$v'_{dr} = r'_r i'_{dr} - (\omega - \omega_r)\lambda'_{qr} + p\lambda'_{dr}, \tag{3.14d}$$

and flux linkages as:

$$\lambda_{qs} = L_{ls} i_{qs} + L_M(i_{qs} + i'_{qr}) \tag{3.15a}$$

$$\lambda_{ds} = L_{ls} i_{ds} + L_M(i_{ds} + i'_{dr}) \tag{3.15b}$$

$$\lambda'_{qr} = L'_{lr} i'_{qr} + L_M(i_{qs} + i'_{qr}) \tag{3.15c}$$

$$\lambda'_{dr} = L'_{lr} i'_{dr} + L_M(i_{ds} + i'_{dr}), \tag{3.15d}$$

where $L_M = (3/2)L_{ms}$. Note that in (3.14)-(3.15), and the remainder of this dissertation, balanced operation is assumed, i.e., $0s(r)$ variables are zero and therefore neglected. By inspection of

(3.14)-(3.15), the differential equations for the qd variables for the stator and rotor circuits can be represented by the equivalent circuits shown in Fig. 3.2. The electromagnetic torque produced by

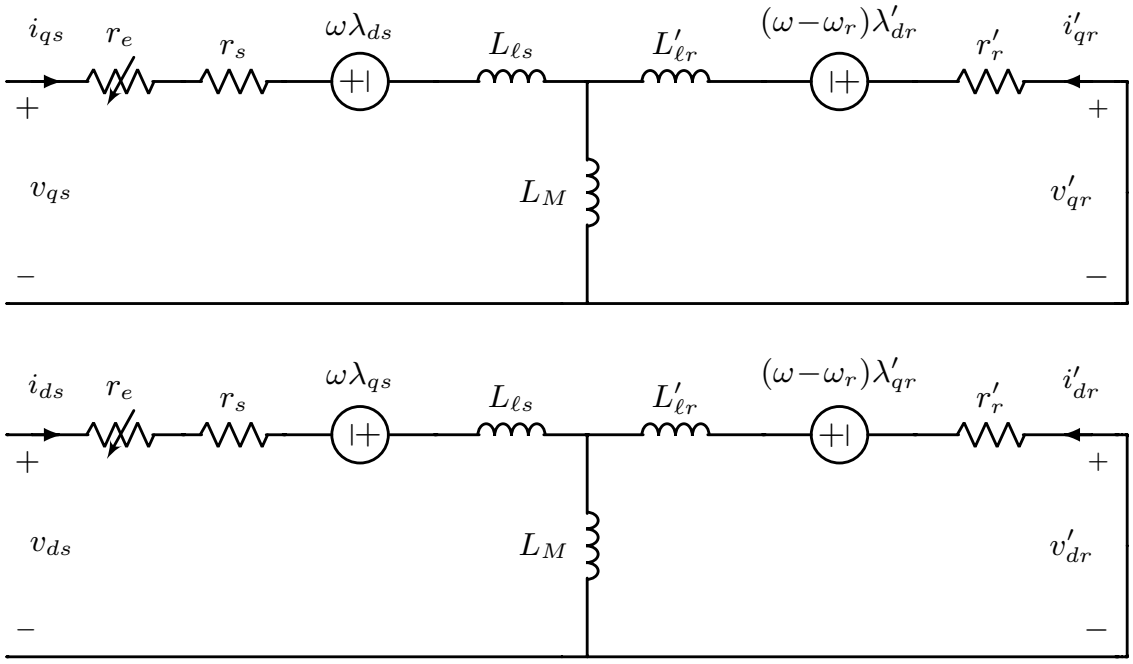

Figure 3.2: Induction machine equivalent $qd0$ circuits with external variable stator resistance r_e.

the induction machine (acting counter-clockwise in Fig. 3.1 by convention) can be expressed in qd variables [35] as:

$$T_e = \frac{3}{2}\frac{P}{2}\frac{L_M}{L'_{rr}}\left(i_{qs}\lambda'_{dr} - i_{ds}\lambda'_{qr}\right), \tag{3.16}$$

where $L'_{rr} := L_M + L'_{lr}$ is the rotor self-inductance. Finally, the electrical and mechanical torques on the rotor are related as:

$$T_e - T_L = Jp\omega_{rm} + B_m\omega_{rm}, \tag{3.17}$$

where T_L is the mechanical load torque (acting clockwise in Fig. 3.1 by convention), J is the rotor inertia, and B_m is a loss coefficient associated with windage and friction.

3.1.2 Compensated Voltz-per-Hertz Control

Because IMs generally operate near synchronous speed, ω_e, (the radial frequency of the electrical source), a common voltage-source control strategy for regulating rotor speed in IMs is accomplished by altering the frequency of the electrical supply voltage. However, this change in frequency must be offset by a change in the voltage source magnitude to avoid magnetic saturation. To achieve these two objectives, the *voltz-per-hertz* control strategy [35] is designed to keep the magnetic flux in the motor constant; this is achieved by holding the following ratio constant:

$$\frac{V_s}{\omega_e} = \frac{V_b}{\omega_b}, \tag{3.18}$$

where V_s is the (rms) magnitude of the voltage source; V_b and ω_b are the rated ("base") voltage (rms) magnitude and frequency, respectively. An improvement upon basic volts-per-hertz control that improves performance at lower speeds is the *compensated voltz-per-hertz* (CVHz) strategy [35]. In CVHz, the voltage source amplitude V_s is updated to compensate for the voltage drop across the stator resistance as:

$$V_s = V_b \sqrt{\frac{\hat{r}_s^2 + \omega_e^2 \hat{L}_{ss}^2}{\hat{r}_s^2 + \omega_b^2 \hat{L}_{ss}^2}}, \tag{3.19}$$

where $L_{ss} := L_M + L_{ls}$ is the stator self-inductance; $\hat{r}_s, \hat{L}_{ss}$ are estimated stator resistance and self-inductance, respectively. The CVHz also includes current feedback to determine the electrical frequency to reduce the speed error of the control. The synchronous speed is computed as:

$$\omega_e = \frac{\omega_r^* + \sqrt{\max\left(0, \omega_r^{*2} + X_{corr}\right)}}{2} \tag{3.20}$$

where ω_r^* is the commanded rotor speed, $X_{corr} = H_{LPF}(s)\chi_{corr}$ is a correction factor where $H_{LPF}(s)$ is a low-pass filter transfer function, and:

$$\chi_{corr} = \frac{3P\left(v_{qs}^{e*} i_{qs}^e - 2r_s I_s^2\right)}{K_{tv}}, \tag{3.21}$$

where the constant K_{tv} in (3.21) is computed as:

$$K_{tv} = \frac{3PL_M^2V_b^2}{2r_r'(r_s^2 + \omega_b^2 L_{ss}^2)} \tag{3.22}$$

and the (rms) source current I_s in (3.21) is computed as

$$I_s = \frac{1}{\sqrt{2}}\sqrt{(i_{qs}^e)^2 + (i_{ds}^e)^2}. \tag{3.23}$$

A block diagram of the CVHz strategy is shown in Fig. 3.3.

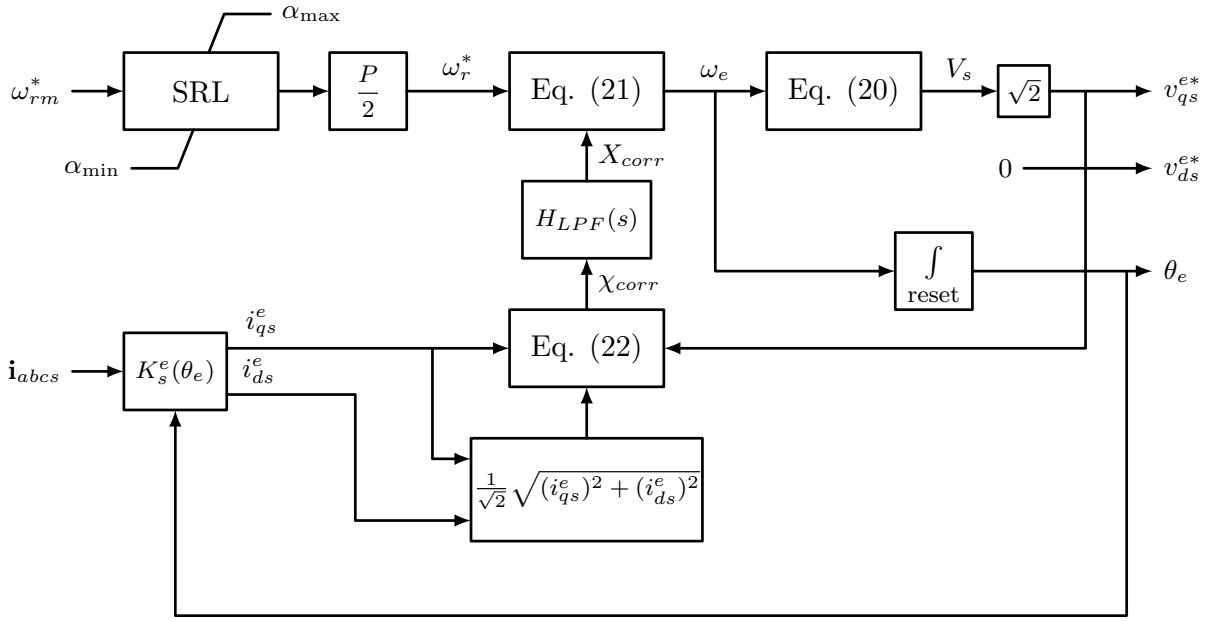

Figure 3.3: Block diagram of the compensated volts-per-hertz control algorithm.

In Fig. 3.3, commanded mechanical rotor speed ω_{rm}^* is used to obtain electrical frequency, ω_e, and voltage magnitude, V_s. The slew rate limiter (SRL) limits the ramp rate of the commanded speed within limits $\alpha_{\min}$ and $\alpha_{\max}$. Note that reference frame transformation of the stationary current variables is specified as the synchronous reference frame, i.e., $\omega = \omega_e$; this is indicated by the superscript "e" on the qd current and voltage variables. The electrical position angle θ_e

is obtained by integrating the electrical angular frequency ω_e and bounding its range to $[0, 2\pi)$. Realization of the commanded voltages in the converter is depicted in Fig. 3.4.

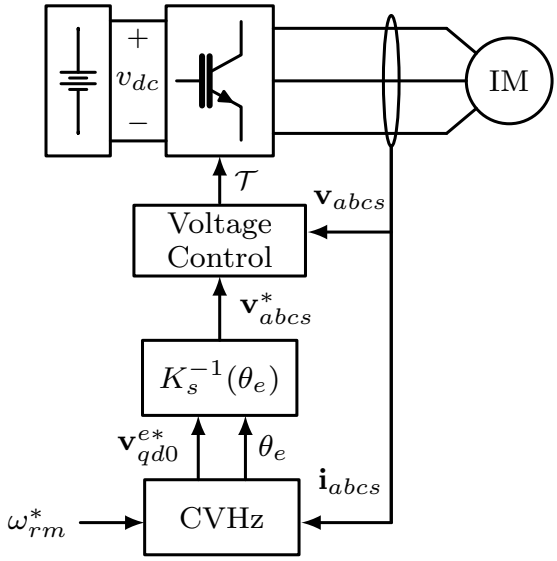

Figure 3.4: Compensated volts-per-hertz control drive block diagram.

In Fig. 3.4, the desired phase voltages in the stationary reference frame, $\mathbf{v}^*_{abcs}$, are obtained by the inverse transformation $\mathbf{v}^*_{abcs} = \mathbf{K}_s^{-1}(\theta_e)\mathbf{v}^{e*}_{qd0s}$; these desired voltages are then synthesized by the switching states $\mathcal{T}$ derived by the "Voltage Control," e.g., implementing pulse-width or space-vector modulation [36] to invert the DC input voltage v_{dc}.

3.1.3 Indirect Field-Oriented Control

Another IM control technique referred to in this dissertation is a current-control strategy called *indirect field-oriented control* (IDFOC). Field-oriented control methods generally operate by establishing and maintaining orthogonality between the rotor flux and current vectors, expressed in the qd reference frame. (The "indirect" method of field-oriented control refers to the lack of direct magnetic flux sensing in the motor, which eliminates the expense of the sensors; rather, flux is estimated in the control algorithm.) Derivation of the control equations to achieve conditions for orthogonality are given in [35]; a summary of the control and interface to the converter is depicted in block diagram form in Fig. 3.5.

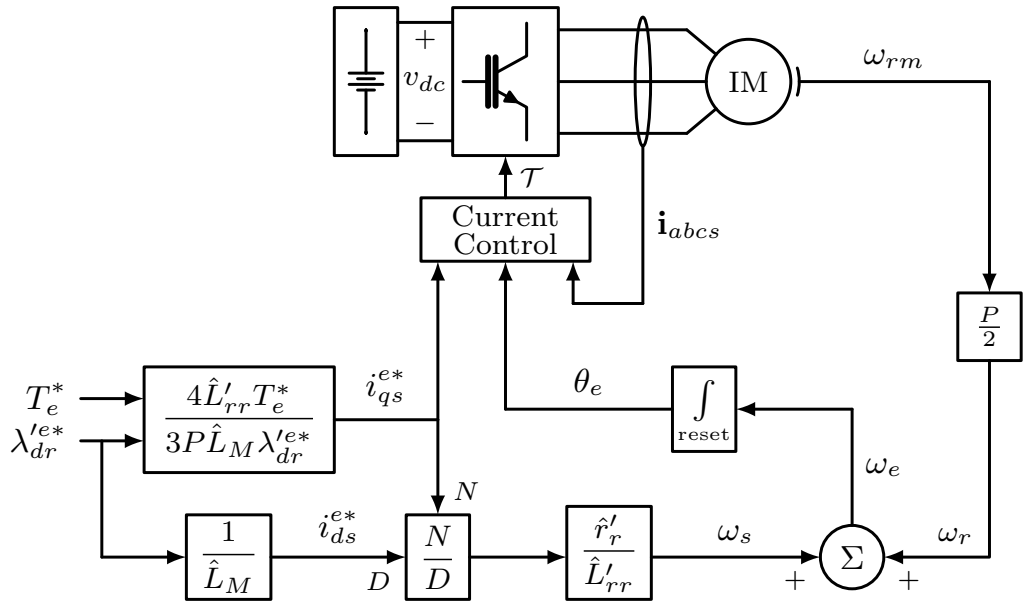

Figure 3.5: Indirect field-oriented control drive block diagram.

In Fig. 3.5, T_e^* and $\lambda_{dr}'^{e*}$ are the commanded electromagnetic torque and d axis rotor flux linkage in the synchronous reference frame, respectively; these quantities serve as inputs to the control algorithm; i_{qs}^{e*}, i_{ds}^{e*}, are derived stator current commands for the q and d axis in the synchronous reference frame, respectively; $\hat{r}_r'$, $\hat{L}_{rr}'$, $\hat{L}_M$ are estimated values for the rotor winding resistance, rotor self inductance, and mutual inductance, respectively; $\omega_s := \omega_e - \omega_r$ is the slip speed. The power-electronic converter provides three-phase AC currents to the stator winding of the IM. Switching states, $\mathcal{T}$, are computed in the "Current Control" block to ensure the desired currents match the measured currents, e.g., achieved by a hysteresis-band switching scheme. The commanded torque in Fig. 3.5 is obtained from a speed control loop, such as the one shown in Fig. 3.6.

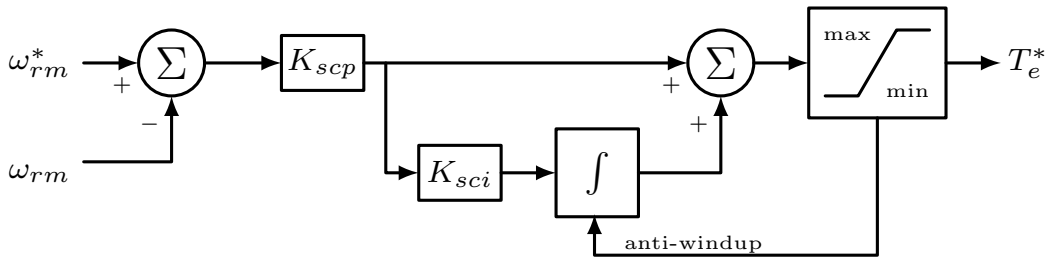

Figure 3.6: Closed-loop speed control block diagram.

In Fig. 3.6, K_{scp}, K_{sci} are the proportional and integral gains of the speed control respectively; $\max, \min$ are the maximum and minimum electromagnetic torques, respectively. The PI gains of the closed-loop speed control are tuned in such a way as to achieve a desirable closed-loop response in terms of both tracking error and load rejection. Once determined the required bandwidth and damping factor (associated with the oscillatory response), the pole placement technique is usually employed [37, 38].

3.1.4 Three-Phase Power Converters

In the previous sections, the speed control techniques presented make use of a central and important component to power the induction machines, which is a three-phase power converter. In the voltage-control strategy, the power converter is responsible for synthesizing the commanded voltages output by the control algorithm (e.g., $\mathbf{v}^*_{abcs}$ in the CVHz.) On the other hand, for the current-control strategy, the power converter must deliver the commanded currents that the control algorithm calculates (e.g., $\mathbf{i}^*_{abcs}$ in the indirect field-oriented control.) There are several three-phase power converter topologies that can be used to power an induction machine [39, 40]. The AC/AC type goes without a DC link, like a matrix converter, which is powered directly by an AC voltage source. For the DC/AC type, a DC voltage must be provided, either by means of a battery bank or a voltage rectifier. Three-phase power converters also vary in terms of the number of switches employed, which determines how many voltage levels it can produce. More levels usually result in lower harmonic distortion, at the expense of higher cost and control complexity. In this work, a DC/AC two-level power converter is employed.

Fig. 3.7 shows the equivalent circuit of such a power converter. It produces controllable AC voltage and currents from the DC source as follows. The DC voltage source, V_{DC}, is connected across three identical parallel-connected "legs," one for each electrical phase, through a "DC link" capacitor, C_0 (the DC link capacitor was included to accommodate in-rush currents to avoid overloading the DC supply). In Fig. 3.7, the individual power-electronic switches are labeled S_1 to S_6. Each switch also includes parallel "fly-back" diodes. By selectively commanding the on- and off-

states of the switches, the three-phase output voltage or current (depending on the control strategy) of the power converter can be fully controlled in terms of amplitude, frequency, and electrical phase angle. In addition, with the parallel switch and diode combination, the converter is bi-directional, i.e., it can provide power flow in either direction. Each phase of the converter is connected to the stator winding of the drive machine ("M"). The voltage between two different phases, say v_{AB}, can assume two non-zero values, depending on the combination of the switch states: either $+V_{DC}$ (for S_1 and S_5 on) or $-V_{DC}$ (for S_1 and S_5 off). Hence this power converter is classified as a two-level one.

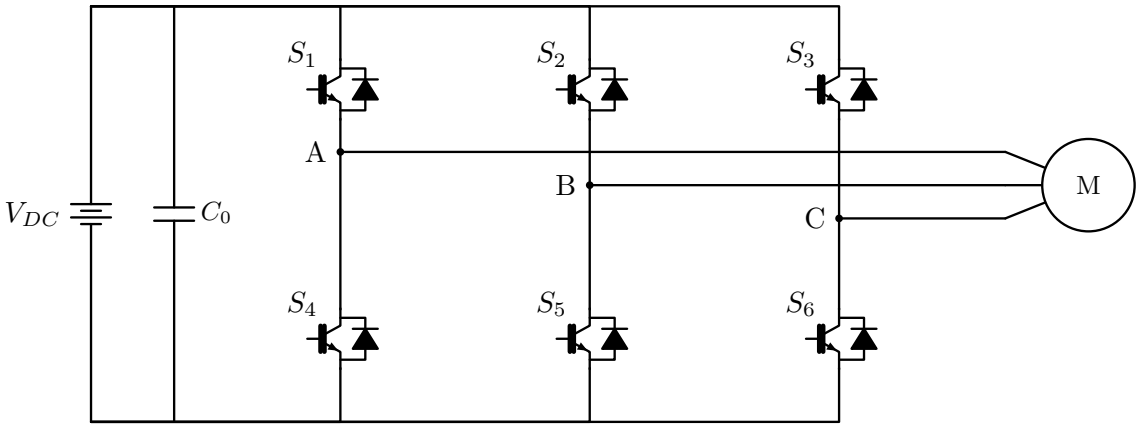

Figure 3.7: Three-phase, two-level, fully-controllable bi-directional power converter.

3.2 Background on $\mathcal{H}_\infty$ Control Design Method

The $\mathcal{H}_\infty$ method has been demonstrated in the literature for the design of controls for applications including rotorcrafts [41], autonomous vehicles [42], uninterruptible power supplies [43], DC servo motors [44], robotics with a focus on uncertainties [45] and others. Some of the advantages of the method are its applicability to multi-input multi-output (MIMO) systems and inclusion of system uncertainties [46]. However, the extant literature does not include a demonstration of the $\mathcal{H}_\infty$ method applied to the design of a control approach for combined speed and rotor position syn-

chronization of parallel electrical machines. This section provides a brief overview of the general control synthesis problem using the $\mathcal{H}_\infty$ method, importance weights, and their selection.

3.2.1 Description of the General Control Synthesis Problem

Consider the general MIMO control system in Fig. 3.8. In Fig. 3.8, $\mathbf{P}(s)$ represents the system plant in the Laplace domain; $\mathbf{K}(s)$ represents the controller; $\mathbf{w}(s), \mathbf{z}(s)$ are vectors of exogenous input signals and controlled output signals, respectively; $\mathbf{u}(s), \mathbf{y}(s)$, are vectors of manipulated and measured signals, respectively. The system is written in matrix form as:

$$\begin{bmatrix} \mathbf{z}(s) \\ \mathbf{y}(s) \end{bmatrix} = \mathbf{P}(s) \begin{bmatrix} \mathbf{w}(s) \\ \mathbf{u}(s) \end{bmatrix} = \begin{bmatrix} P_{11}(s) & P_{12}(s) \\ P_{21}(s) & P_{22}(s) \end{bmatrix} \begin{bmatrix} \mathbf{w}(s) \\ \mathbf{u}(s) \end{bmatrix} \tag{3.24a}$$

$$\mathbf{u}(s) = \mathbf{K}(s)\mathbf{y}(s). \tag{3.24b}$$

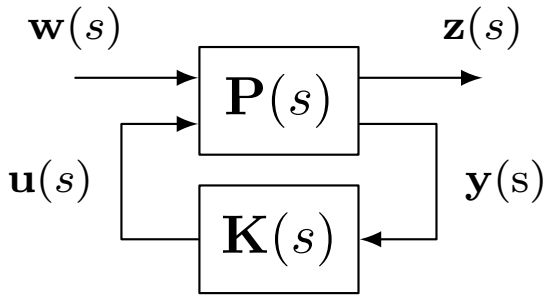

Figure 3.8: Block diagram of general control system.

The closed-loop transfer function of the system in Fig. 3.8 (with s argument suppressed) can be written [47]:

$$\mathbf{z} = F_l(\mathbf{P}, \mathbf{K})\mathbf{w}, \tag{3.25}$$

where:

$$F_l(\mathbf{P}, \mathbf{K}) := P_{11} + P_{12}\mathbf{K}(\mathbf{I} - P_{22}\mathbf{K})^{-1}P_{21}, \tag{3.26}$$

where $\mathbf{I}$ is the appropriately sized identity matrix.

The control synthesis optimization problem seeks to minimize the $\mathcal{H}_\infty$ norm of $F_l(\mathbf{P}, \mathbf{K})$, which optimizes control system performance in terms of tracking error (with respect to a commanded external signal) and disturbance rejection. The optimization problem is stated as follows:

$$\mathbf{K} = \arg\min_{\mathbf{K}\in\mathcal{K}} ||F_l(\mathbf{P}, \mathbf{K})||_\infty, \tag{3.27}$$

where $\mathcal{K}$ is the set of all controllers that stabilize the plant and the $\mathcal{H}_\infty$ norm is defined as:

$$||G(s)||_\infty := \sup_\omega \bar{\sigma}(G(j\omega)), \tag{3.28}$$

where $G(s)$ is the transfer function of interest, ω is frequency, and $\bar{\sigma}$ denotes the maximum singular value of a square matrix [47]. The $\mathcal{H}_\infty$ norm is therefore the highest input/output gain for a MIMO system, for the worst possible choice of the input vector. For the case of $F_l(\mathbf{P}, \mathbf{K})$, it can also be written [47]:

$$||F_l(\mathbf{P}, \mathbf{K})||_\infty = \max_{\mathbf{w}(t)\neq 0} \frac{||\mathbf{z}(t)||_2}{||\mathbf{w}(t)||_2}, \tag{3.29}$$

where $||\mathbf{x}(t)||_2 := \sqrt{\int_0^\infty \sum_i |x_i(t)|^2\, dt}$ is the ℓ^2-norm of the vector signal $\mathbf{x}(t)$.

3.2.2 Importance Weights and Their Selection

Modification of the control system in Fig. 3.8 can be employed to assign weights to relative importance in system performance, e.g., noise rejection or other desired performance within a specified bandwidth. Fig. 3.9 depicts the modified control system with 'importance' weights.

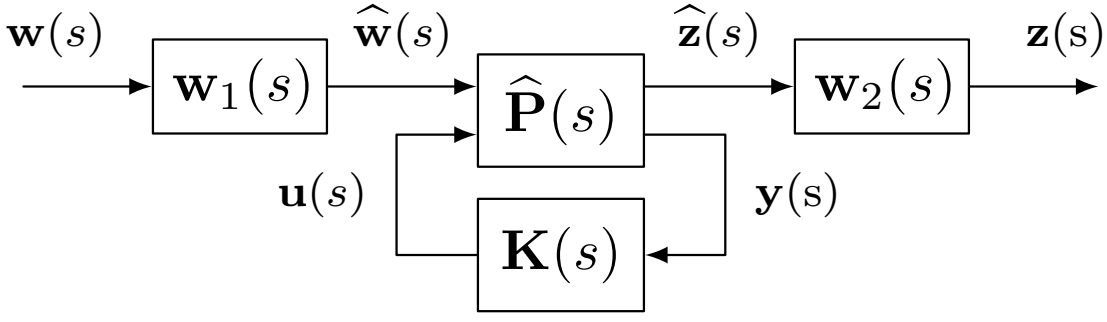

Figure 3.9: Control system with importance weights.

In Fig. 3.9, weight vectors $\mathbf{w}_1(s), \mathbf{w}_2(s)$ are applied to the input and output vectors signals, respectively; $\widehat{\mathbf{w}}(s), \widehat{\mathbf{z}}(s)$ are modified input and output signals; $\widehat{\mathbf{P}}(s)$ is the internal modified plant:

$$\widehat{\mathbf{P}}(s) := \begin{bmatrix} \widehat{P}_{11}(s) & \widehat{P}_{12}(s) \\ \widehat{P}_{11}(s) & \widehat{P}_{22}(s) \end{bmatrix} \tag{3.30}$$

and the overall plant transfer function is:

$$\mathbf{P}(s) = \begin{bmatrix} \mathbf{w}_2(s)\widehat{P}_{11}(s)\mathbf{w}_1(s) & \mathbf{w}_2(s)\widehat{P}_{12}(s) \\ \widehat{P}_{11}(s)\mathbf{w}_1(s) & \widehat{P}_{22}(s) \end{bmatrix}. \tag{3.31}$$

Solution of the control synthesis problem in (3.27) with importance weights is then performed using the modified plant description in (3.31).

Chapter 4

Speed and Position Synchronization

This chapter describes the proposed method for achieving speed and position synchronization in CCMM architectures. It also develops the necessary framework to be used for the $\mathcal{H}_\infty$ control synthesis.

4.1 A Novel Synchronization Method

As shown in Fig. 1.2a, in the DCMM architecture each mechanical actuation line is supplied by a dedicated power-electronic converter. Although each actuator may experience a different force, voltage (current) control of the converters may be implemented independently to supply the appropriate commanded voltage (current) waveform magnitudes and phase shifts to achieve position synchronization.

In the CCMM architecture in Fig. 1.2b however, the central power-electronic converter supplies all of the mechanical actuation lines of the system in parallel. Converter output voltages are therefore applied to the stator terminals of each IM equally, with total phase current divided between the motors. Therefore, in order to achieve position synchronization in CCMM under unequal mechanical forces, the feedback control method proposed herein changes the effective input impedance of the IMs independently to enable control of rotor speeds and positions.

Induction machines are designed to operate under rated load near—but not exactly at—synchronous speed; synchronous speed being $\omega_r = \omega_e$. From (3.17), steady-state equilibrium of the motor (neglecting windage and friction) is achieved when $T_e = T_L$. Fig. 4.1 illustrates steady-state electromagnetic torque versus normalized rotor speed, for a 15 hp (11.19 kW) induction machine. (See Appendix A for the motor parameters.) In Fig. 4.1, the dashed line represents the applied load torque. The steady-state operating speed, $\omega_{r,ss}$, can be found by the intersection of the electromagnetic torque curve and the load torque on the negative slope of the T_e curve. (The restriction to negative slopes on the T_e curve is required to ensure stable equilibrium, see [35].)

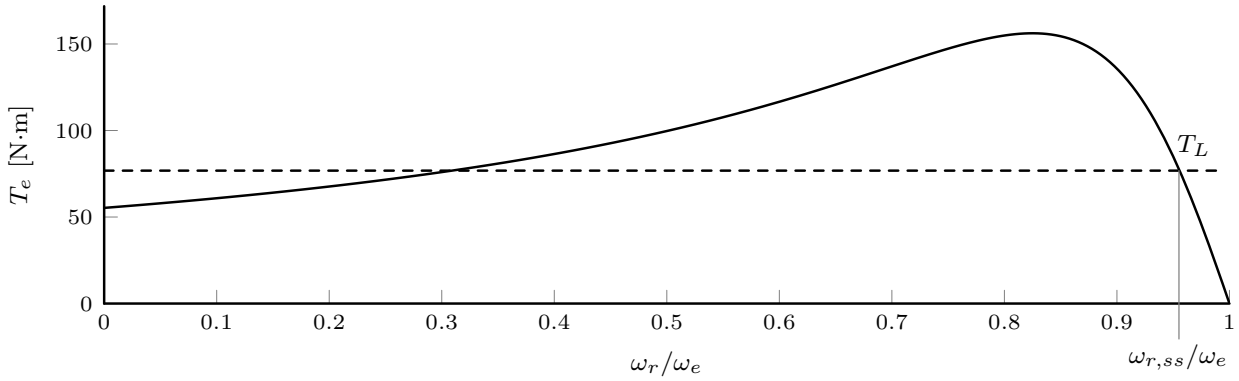

Figure 4.1: Steady-state torque vs. normalized speed curve, indicating steady-state operating speed, $\omega_{r,ss}$, for applied torque load, T_L.

Examination of Fig. 4.1 indicates a method to alter steady-state rotor speed in an IM for a given load torque. In particular, if the slope of the T_e curve near synchronous speed (i.e., $\omega_r/\omega_e = 1$) is modified, the corresponding steady-state rotor speed will also be altered. A method to achieve a change in the slope of the T_e curve is through the addition of external stator resistances placed in series with the stator windings, which changes the steady-state motor input impedance seen by the power supply (refer to Fig. 3.2). Fig. 4.2 illustrates this concept for various values of external stator resistance. As shown in Fig. 4.2, increasing the external stator resistance—which changes the total

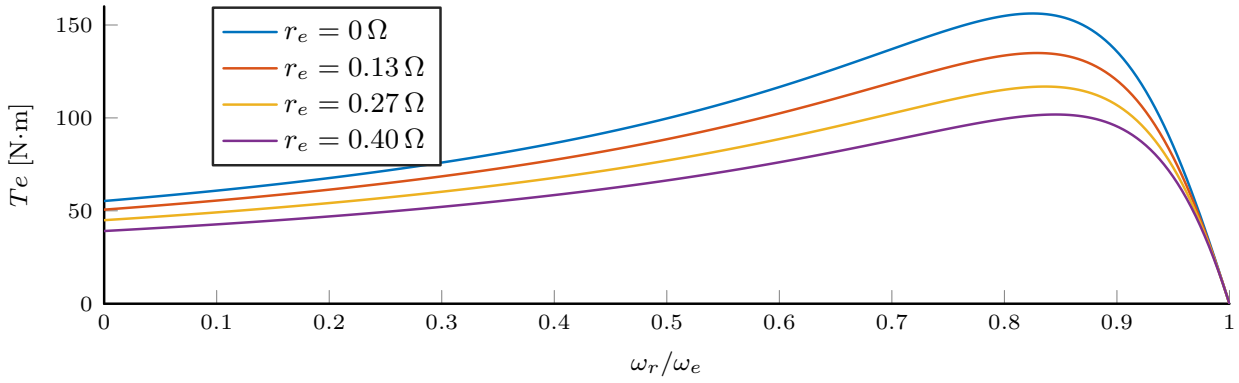

Figure 4.2: Steady-state torque vs. speed for different values of external stator resistance.

machine input impedance seen by the source—results in a decreasing slope of the equivalent T_e vs. speed curve. The observations described in the foregoing provide the motivation for the simul-

taneous speed and position synchronization approach for parallel IMs in a CCMM architecture in this research. In particular, simultaneous speed and position synchronization in a CCMM topology with unequal torque loads on each motor can be achieved through a combination of speed control utilizing a primary voltage or control strategy (e.g., CVHz or IDFOC) with position synchronization achieved through independent feedback control of variable external three-phase resistances in series with each IM in the system.

Control of the inline stator resistances can be achieved by mechanical means (e.g., linear or rotary rheostat mechanisms) or by using power-electronic circuitry, where the electronic switches are rated for the current on a single motor phase. In the case studies that follow, the power-electronic circuit with bi-directional MOSFET arrangement shown in Fig. 4.3 was used to vary the inline stator resistances.

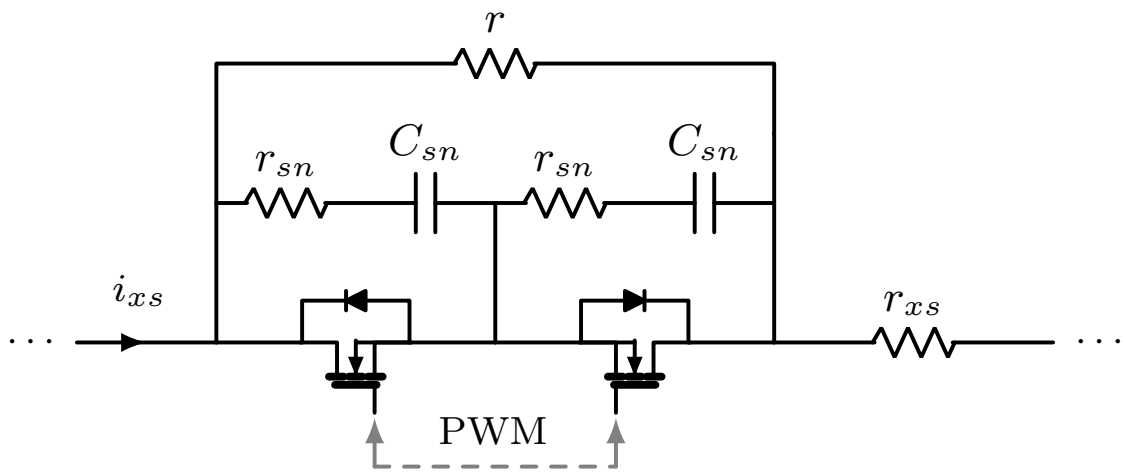

Figure 4.3: Steady-state torque vs. speed for different values of external stator resistance.

In Fig. 4.3, r_{sn}, C_{sn} are snubber resistances and capacitances, respectively; i_{xs}, r_{xs} are the current into and (nominal) resistance of the x-phase stator winding of the drive machine, respectively; r is the "base" external resistance. The MOSFETs receive the same PMW (fully-on or fully-off) signal; their bi-directional arrangement allows current to flow in the stator in both directions. Ne-

glecting snubber impedance, the circuit in Fig. 4.3 places either base resistance r or $0\,\Omega$ in series with the nominal stator resistance. Using PWM modulation, a desired external resistance $\bar{r}_e$ can be achieved in a *fast-average* sense, where the fast-average of a signal $f(t)$ is defined as:

$$\bar{f}(t) := \frac{1}{T_s}\int_0^{T_s} f(t)\,dt, \tag{4.1}$$

where $T_s = 1/f_s$ is the time period of the PWM switching cycle with switch frequency f_s.

Consider the CCMM system depicted in Fig. 1.2b. Suppose external variable resistances are added in series with the three stator windings, for each of the N motors. The external resistance of motor $n \in \mathcal{N}$ is a function of time, denoted herein as $r_{e,n}(t)$. As indicated in Figs. 4.1-4.2, an increase in external resistance of a motor will decrease the slope of its T_e curve, and therefore act to reduce its rotor speed. The first step in the control method is to identify the motor to be designated as "primary"; index $p \in \mathcal{N}$ is used to designate this motor. The voltage/current control on the central converter uses measurements obtained on motor p for implementation of its primary speed control feedback algorithm. The set of indices $\mathcal{S} = \mathcal{N} \setminus \{p\} = \{\, s_1,\, s_2,\, \ldots, s_{N-1} \,\}$ are used to designate all other ("secondary") motors.

Now, define primary and secondary mechanical angular position vectors as:

$$\boldsymbol{\theta}_{rm,p} = \mathbb{1}\theta_{rm,p} = \begin{bmatrix} \theta_{rm,p} \\ \vdots \\ \theta_{rm,p} \end{bmatrix}, \quad \boldsymbol{\theta}_{rm,s} = \begin{bmatrix} \theta_{rm,s_1} \\ \vdots \\ \theta_{rm,s_{N-1}} \end{bmatrix}, \tag{4.2}$$

where $\mathbb{1}$ is a $(1 \times N-1)$ vector of ones, $\theta_{rm,p}$ is the angular position of the primary motor, and $\theta_{rm,s_i}, s_i \in \mathcal{S}$ are the angular positions of the secondary motors.

For the CCMM system depicted in Fig. 1.2b, let $\mathcal{T}$ be the set of transistor states of the central converter. Collecting the external resistances into vector $\mathbf{R}_e(t) := \begin{bmatrix} r_{e,1}(t) & \cdots & r_{e,N}(t) \end{bmatrix}^T$, the central control problem for simultaneous speed and position synchronization is to determine the

switching states $\mathcal{T}$ and resistance signals $\mathbf{R}_e(t)$ to achieve the conditions:

$$\omega_{rm,n} = \omega^*_{rm}, \quad \forall n \in \mathcal{N} \tag{4.3a}$$

$$\Delta\theta_{rm} := ||\boldsymbol{\theta}_{rm,p} - \boldsymbol{\theta}_{rm,s}||_2 \to 0, \tag{4.3b}$$

where ω^*_{rm} is the commanded mechanical rotor speed, $\Delta\theta_{rm}$ is the "normed" angle difference, and $||\cdot||_2$ is the vector ℓ^2-norm. Denote the "individual" angular differences, referenced between secondary and primary motors, as:

$$\delta\theta_{rm,s_i}(t) = \theta_{rm,s_i} - \theta_{rm,p}, \tag{4.4}$$

where:

$$\theta_{rm,s_i}(t) = \int_0^t \omega_{rm,s_i}(\tau)\, d\tau + \theta_{rm,s_i}(0), \quad \forall s_i \in \mathcal{S} \tag{4.5a}$$

$$\theta_{rm,p}(t) = \int_0^t \omega_{rm,p}(\tau)\, d\tau + \theta_{rm,p}(0), \tag{4.5b}$$

and $\theta_{rm,s_i}(0), \theta_{rm,p}(0)$ are the initial mechanical angular position references for the secondary and primary motors, respectively; in (4.5), the $t = 0$ reference designates when the primary and secondary motor designations are assigned.

The position synchronization condition between all secondary rotor angles and the primary rotor angle stated in (4.3b) can be achieved by using $\delta\theta_{rm,s_i}$ to determine the value of $r_{e,s_i}(t)$, e.g., using proportional-integral (PI) feedback control. In particular, the values of the external variable resistances of the secondary motors are updated via PI feedback as:

$$r_{e,s_i}(t) = K_{P,s_i}\delta\theta_{rm,s_i} + K_{I,s_i}\int \delta\theta_{rm,s_i}\, dt, \quad \forall s_i \in \mathcal{S} \tag{4.6}$$

where K_{P,s_i} is the proportional gain and K_{I,s_i} is the integral gain of the PI controller for secondary motor $s_i \in \mathcal{S}$. During the update in (4.6), the external resistance for the primary motor, $r_{e,p}(t)$,

is held at a constant value (the value it had when the motor was designated as primary). Note that while various control strategies could be used to determine the external resistance signals, for initial feasibility and proof-of-concept of the proposed synchronization solution, a PI control was used as a first try for its simplicity. As demonstrated in the following chapters, the PI control performance can be improved by means of more sophisticated control design techniques.

4.2 Model Linearization

This section describes and validates the linearized three-phase induction machine model used in the control design.

4.2.1 Modified Induction Machine Model

The three-phase induction machine model expressed in the arbitrary reference frame, as presented in Section 3.1, is rewritten here for convenience:

$$v_{qs} = r_s i_{qs} + \omega\lambda_{ds} + p\lambda_{qs} \tag{4.7a}$$

$$v_{ds} = r_s i_{ds} - \omega\lambda_{qs} + p\lambda_{ds} \tag{4.7b}$$

$$v_{qr} = r_r i_{qr} + (\omega - \omega_r)\lambda_{dr} + p\lambda_{qr} \tag{4.7c}$$

$$v_{dr} = r_r i_{dr} - (\omega - \omega_r)\lambda_{qr} + p\lambda_{dr}, \tag{4.7d}$$

Note that in (4.7), the prime symbol in the rotor quantities was omitted, but it is still assumed that those quantities are referred to the stator.

Flux linkages and currents are expressed as:

$$\lambda_{qs} = L_{ls} i_{qs} + L_M (i_{qs} + i_{qr}) \tag{4.8a}$$

$$\lambda_{ds} = L_{ls} i_{ds} + L_M (i_{ds} + i_{dr}) \tag{4.8b}$$

$$\lambda_{qr} = L_{lr} i_{qr} + L_M (i_{qs} + i_{qr}) \tag{4.8c}$$

$$\lambda_{dr} = L_{lr} i_{dr} + L_M (i_{ds} + i_{dr}), \tag{4.8d}$$

The electromagnetic torque, T_e, produced by the induction machine can be expressed as:

$$T_e = \frac{3}{2}\frac{P}{2}\frac{L_M}{\sigma L_{ss} L_{rr}} \left(\lambda_{qs}\lambda_{dr} - \lambda_{ds}\lambda_{qr}\right), \tag{4.9}$$

where P is the number of magnetic poles, $L_{ss} := L_{ls} + L_M$, $L_{rr} := L_{lr} + L_M$, and $\sigma := 1 - {L_M^2}/{(L_{ss} L_{rr})}$. Finally, the electrical and mechanical coupling equation is:

$$T_e - T_L = Jp\omega_{rm} + B_m \omega_{rm}, \tag{4.10}$$

where T_L is the mechanical load torque, J is the rotor inertia, B_m is a loss coefficient for windage and friction, and $\omega_{rm} = p\theta_{rm} = ({2}/{P})\omega_r$ is the actual mechanical rotor speed, where θ_{rm} denotes the actual rotor position.

Setting the arbitrary reference frame speed as $\omega = \omega_e$ ('synchronous' speed), where ω_e is the electrical frequency, and alignment of the arbitrary reference frame and the electrical reference position $\theta(0) = \theta_e(0)$ results in $v_{ds}^e = 0$; further assuming short-circuited rotor bars, i.e., $v_{qr}^e = v_{dr}^e = 0$, (4.7) can be written as:

$$v_{qs}^e = (\mu_s + p)\lambda_{qs}^e + \omega_e \lambda_{ds}^e - \mu_s \frac{L_M}{L_{rr}} \lambda_{qr}^e \tag{4.11a}$$

$$0 = (\mu_s + p)\lambda_{ds}^e - \omega_e \lambda_{qs}^e - \mu_s \frac{L_M}{L_{rr}} \lambda_{dr}^e \tag{4.11b}$$

$$0 = (\mu_r + p)\lambda_{qr}^e + (\omega_e - \omega_r)\lambda_{dr}^e - \mu_r \frac{L_M}{L_{ss}} \lambda_{qs}^e \tag{4.11c}$$

$$0 = (\mu_r + p)\lambda_{dr}^e - (\omega_e - \omega_r)\lambda_{qr}^e - \mu_r \frac{L_M}{L_{ss}} \lambda_{ds}^e, \tag{4.11d}$$

where $\mu_s := {}^{r_s}/_{(\sigma L_{ss})}$, $\mu_r := {}^{r_r}/_{(\sigma L_{rr})}$ and superscript e denotes the synchronous reference frame.

4.2.2 Linearization of the Induction Machine Model

With rotor resistance control (4.7) is nonlinear because of the multiplication of variable stator resistances with stator currents; (4.11) is nonlinear because of the multiplication of rotor speed and fluxes; (4.9) is nonlinear because of the multiplication of fluxes. What follows is a procedure for obtaining the small-signal linearized machine equations.

First, variable $f(t)$ is written using Taylor expansion as:

$$f(t) = f_0 + \widetilde{f}(t), \tag{4.12}$$

where f_0 is the DC component, and $\widetilde{f}(t)$ denotes the small-signal component. In the induction machine model, variables to be linearized consist of (*i*) states: stator and rotor flux linkages, rotor speed and position, and (*ii*) inputs: stator voltage, external resistance, and load torque. Since the modified equations in (4.11) use the parameter μ_s instead of r_s, herein $\widetilde{\mu}_s$ is used instead of external resistance, given their linear relationship. Grouping these variables into state vector, $\widetilde{\mathbf{x}}$, and input vector, $\widetilde{\mathbf{u}}$:

$$\widetilde{\mathbf{x}} = \begin{bmatrix} \widetilde{\lambda}^e_{qs} & \widetilde{\lambda}^e_{ds} & \widetilde{\lambda}^e_{qr} & \widetilde{\lambda}^e_{dr} & \widetilde{\omega}_r & \widetilde{\theta}_r \end{bmatrix}^T \tag{4.13a}$$

$$\widetilde{\mathbf{u}} = \begin{bmatrix} \widetilde{v}^e_{qs} & \widetilde{\mu}_s & \widetilde{T}_L \end{bmatrix}^T. \tag{4.13b}$$

Linearization of (4.13) is obtained by differentiating each state variable about its DC operating point and extracting the small-signal equations which are summarized as:

$$\begin{aligned}\widetilde{v}_{qs}^{e} &= \left(\lambda_{qs0}^{e} - \frac{L_M}{L_{rr}}\lambda_{qr0}^{e}\right)\widetilde{\mu}_s + (\mu_{s0}+p)\widetilde{\lambda}_{qs}^{e} + \omega_e\widetilde{\lambda}_{ds}^{e} \\ &\quad -\mu_{s0}\frac{L_M}{L_{rr}}\widetilde{\lambda}_{qr}^{e} \qquad (4.14a)\\ \widetilde{v}_{ds}^{e} &= \left(\lambda_{ds0}^{e} - \frac{L_M}{L_{rr}}\lambda_{dr0}^{e}\right)\widetilde{\mu}_s + (\mu_{s0}+p)\widetilde{\lambda}_{ds}^{e} - \omega_e\widetilde{\lambda}_{qs}^{e} \\ &\quad -\mu_{s0}\frac{L_M}{L_{rr}}\widetilde{\lambda}_{dr}^{e} \qquad (4.14b)\\ \widetilde{v}_{qr}^{e} &= (\mu_r+p)\widetilde{\lambda}_{qr}^{e} - \lambda_{dr0}^{e}\widetilde{\omega}_r + (\omega_e-\omega_{r0})\widetilde{\lambda}_{dr}^{e} - \mu_r\frac{L_M}{L_{ss}}\widetilde{\lambda}_{qs}^{e} \qquad (4.14c)\\ \widetilde{v}_{dr}^{e} &= (\mu_r+p)\widetilde{\lambda}_{dr}^{e} + \lambda_{qr0}^{e}\widetilde{\omega}_r - (\omega_e-\omega_{r0})\widetilde{\lambda}_{qr}^{e} - \mu_r\frac{L_M}{L_{ss}}\widetilde{\lambda}_{ds}^{e} \qquad (4.14d)\\ \widetilde{T}_e &= K_T(\lambda_{dr0}^{e}\widetilde{\lambda}_{qs}^{e} + \lambda_{qs0}^{e}\widetilde{\lambda}_{dr}^{e} - \lambda_{ds0}^{e}\widetilde{\lambda}_{ds}^{e} - \lambda_{qr0}^{e}\widetilde{\lambda}_{ds}^{e}), \qquad (4.14e)\end{aligned}$$

where $K_T := (3P/4)(L_M/(\sigma L_{ss}L_{rr}))$. Since (4.10) is already linear, its small-signal model is obtained by inspection as:

$$\widetilde{T}_e - \widetilde{T}_L = J'p\widetilde{\omega}_r + B'_m\widetilde{\omega}_r, \qquad (4.15)$$

where $J' := J(2/P)$, $B'_m := B_m(2/P)$, and $\widetilde{\omega}_r = p\widetilde{\theta}_r$.

The small-signal model may now be represented in state-space form:

$$p\widetilde{\mathbf{x}} = \mathbf{A}\widetilde{\mathbf{x}} + \mathbf{B}\widetilde{\mathbf{u}}, \qquad (4.16)$$

where input matrix:

$$\mathbf{A} = \begin{bmatrix} -\mu_{s0} & \omega_e & \frac{\mu_r L_M}{L_{ss}} & 0 & \left(\frac{K_T}{J'}\right)\lambda^e_{dr0} & 0 \\ -\omega_e & -\mu_{s0} & 0 & \frac{\mu_r L_M}{L_{ss}} & -\left(\frac{K_T}{J'}\right)\lambda^e_{qr0} & 0 \\ \frac{\mu_{s0} L_M}{L_{rr}} & 0 & -\mu_r & s_0\omega_e & -\left(\frac{K_T}{J'}\right)\lambda^e_{ds0} & 0 \\ 0 & \frac{\mu_{s0} L_M}{L_{rr}} & -s_0\omega_e & -\mu_r & \left(\frac{K_T}{J'}\right)\lambda^e_{qs0} & 0 \\ 0 & 0 & \lambda^e_{dr0} & -\lambda^e_{qr0} & -\frac{B'_m}{J'} & 1 \\ 0 & 0 & 0 & 0 & 0 & 0 \end{bmatrix}^T, \tag{4.17}$$

where $s_0 := {}^{(\omega_e - \omega_{r0})}/_{\omega_e}$ and output matrix:

$$\mathbf{B} = \begin{bmatrix} 1 & (L_M/L_{rr})\lambda^e_{qr0} - \lambda^e_{qs0} & 0 \\ 0 & (L_M/L_{rr})\lambda^e_{dr0} - \lambda^e_{ds0} & 0 \\ 0 & 0 & 0 \\ 0 & 0 & 0 \\ 0 & 0 & -1/J' \\ 0 & 0 & 0 \end{bmatrix}. \tag{4.18}$$

4.2.3 Validation of Linear Induction Machine Model

To validate the linear induction machine model, the machine response using the standard and linear models under typical transient conditions were compared. Both models were first initialized by reaching steady-state under the following conditions: $\omega_e = 1\,\text{pu}$, $v_{qs} = 1\,\text{pu}$, $T_L = 1\,\text{pu}$, and equivalent external resistance $\bar{r}_e = 0\,\Omega$. The machine parameters used are given in Table A.1. The DC operating points for the linear model described by (4.16)-(4.18) are computed and held constant for the remainder of the studies.

In the first study, the load torque is instantaneously reduced to 0.2 pu while holding the external resistance at $\bar{r}_e = 0\,\Omega$. Figs. 4.4-4.6 show the computed rotor speeds, stator and rotor fluxes, respectively. As shown in Figs. 4.4-4.6 the transient speed and flux responses are very similar in

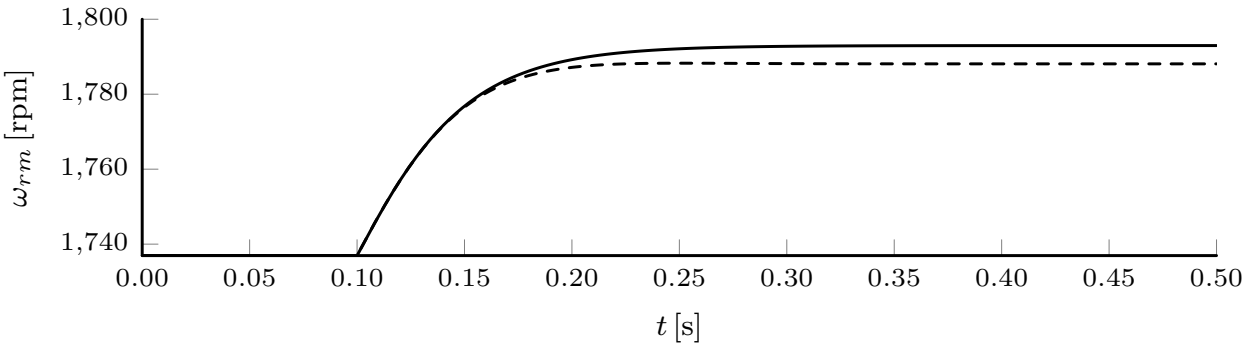

Figure 4.4: Comparison of rotor speed after step change in load torque using linear (solid) and complete (dashed) models.

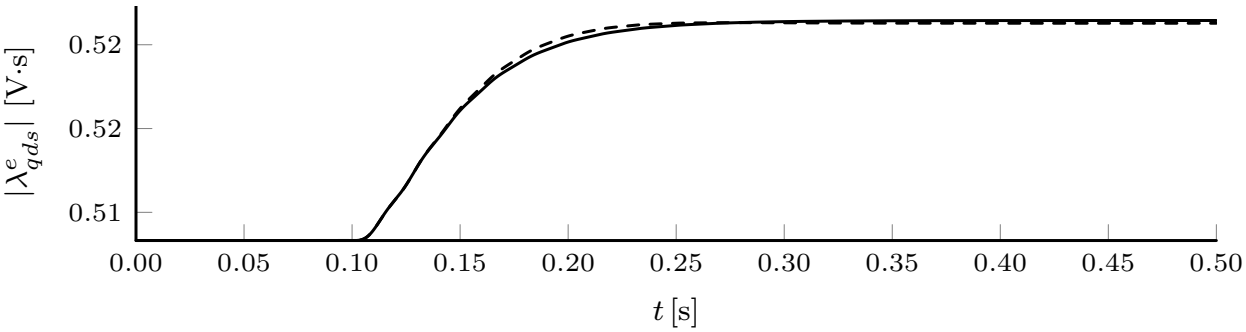

Figure 4.5: Comparison of stator flux linkage after step change in load torque using linear (solid) and complete (dashed) models.

shape, with small steady-steady deviations of 0.27% (speed), 0.01% (stator flux), and 2.7% (rotor flux). It can be concluded that the small-signal linear model is reasonably valid for this large step in load torque.

In the second study, the external resistance is instantaneously increased to 4.0 pu while holding the load torque at $T_L = 1$ pu. Figs. 4.7-4.9 show the computed rotor speeds, stator and rotor fluxes in these scenarios, respectively.

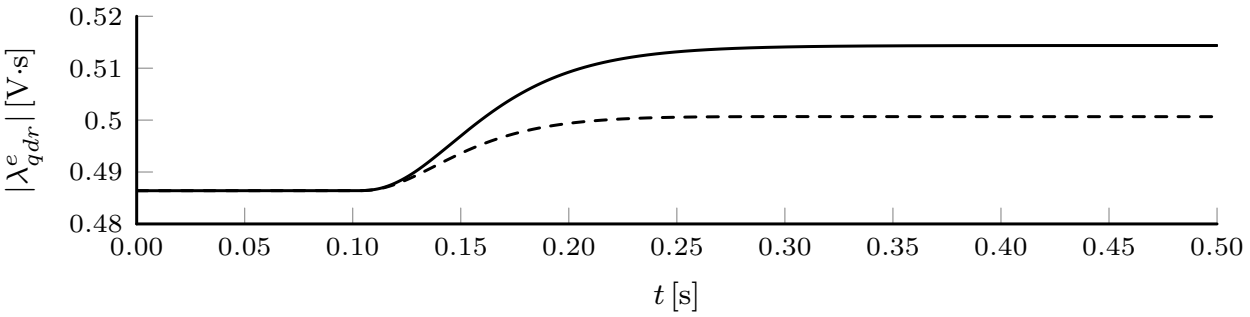

Figure 4.6: Comparison of rotor flux linkage after step change in load torque using linear (solid) and complete (dashed) models.

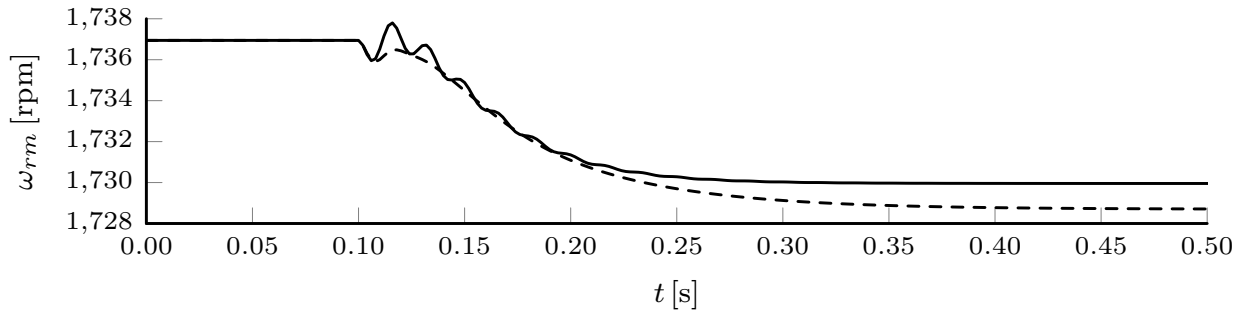

Figure 4.7: Comparison of rotor speed after step change in external resistance using linear (solid) and complete (dashed) models.

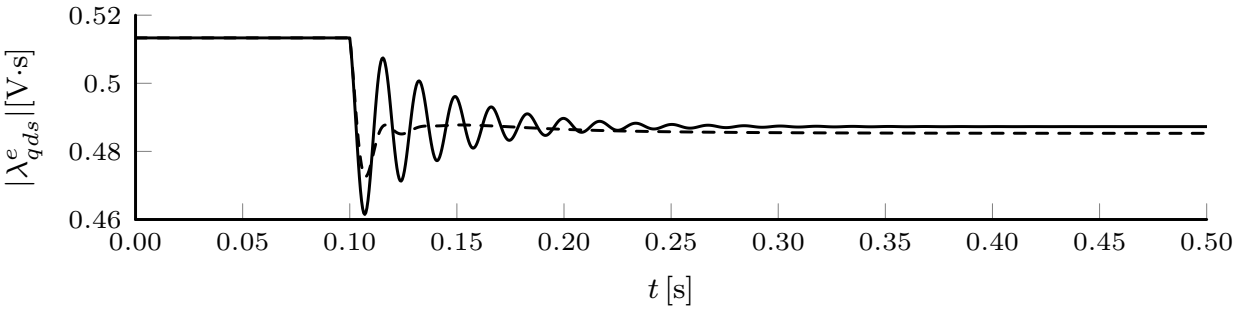

Figure 4.8: Comparison of stator flux linkage after step change in external resistance using linear (solid) and complete (dashed) models.

As shown in Figs. 4.7-4.9 the transient speed and flux responses are similar in shape, with small differences in damping and steady-steady deviations of 0.7% (speed), 0.4% (stator flux), and 0.4% (rotor flux). In this case, although the differences in the dynamic response are more prominent compared to that observed during torque load steps, the differences in steady-steady state error are lower. This study indicates that the small-signal linear model is also reasonably valid for this large

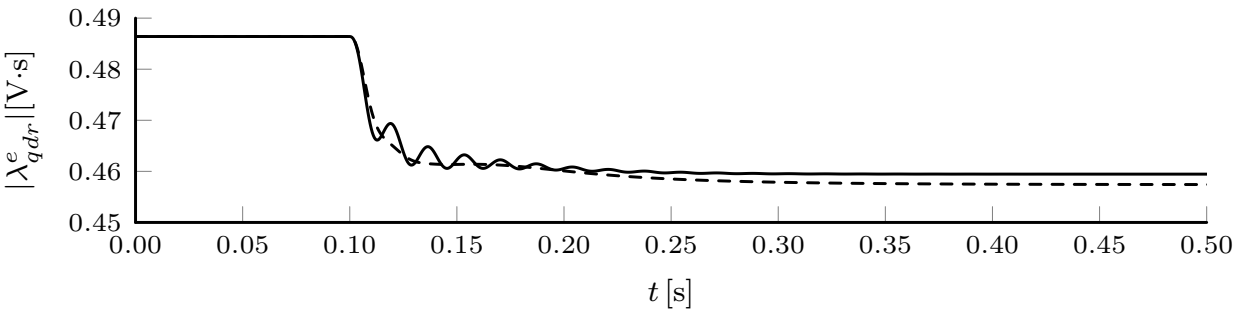

Figure 4.9: Comparison of rotor flux linkage after step change in external resistance using linear (solid) and complete (dashed) models.

step in external resistance. Based on the foregoing studies, the linear induction machine model described in section 4.2.2 was used in the optimal control design described in this dissertation.

4.3 Modified Plant Design

Design of the modified plant $\widehat{\mathbf{P}}(s)$ using optimal control synthesis for the IM position synchronization problem was performed as follows. Herein, it was assumed that synchronization was applied to two IMs in a CCMM configuration; without loss of generality machine $n = 1$ was designated primary and $n = 2$ as secondary. Each IM was represented by the linear model described in section 4.2.2, both with identical electrical parameters, given in Table A.1.

First, the vector $\mathbf{w}$ in Fig. 3.9 consists of exogenous inputs which was defined as:

$$\mathbf{w} := \begin{bmatrix} \widetilde{T}_{L,1} & \widetilde{T}_{L,1} & \widetilde{n} \end{bmatrix}^T, \tag{4.19}$$

where $\widetilde{T}_{L,1}, \widetilde{T}_{L,2}$ are small-signal mechanical load torques for the primary and secondary IMs respectively, and $\widetilde{n}$ is measurement noise.

Next, the vector $\mathbf{z}$ in Fig. 3.9, corresponds to signals for which the small-signal norm minimization is to be applied ('controlled variables'), was defined as:

$$\mathbf{z} := \begin{bmatrix} \delta\widetilde{\theta}_{rm} & \widetilde{\mu}_{s,2} \end{bmatrix}^T, \tag{4.20}$$

where small-signal position error $\delta\widetilde{\theta}_{rm} := \widetilde{\theta}_{rm,1} - \widetilde{\theta}_{rm,2}$, and $\widetilde{\mu}_{s,2}$ is a control variable for the external resistance of the secondary machine.

The vectors $\mathbf{y}$ and $\mathbf{u}$ in Fig. 3.9 consist of measured and 'manipulated' signals, respectively. In this case, the measured signal was taken as the small-signal position error with measurement noise:

$$\mathbf{y} := \begin{bmatrix} \delta\widetilde{\theta}_{rm} + \widetilde{n} \end{bmatrix} \tag{4.21}$$

and the manipulated variable for the external resistance:

$$\mathbf{u} := \begin{bmatrix} \widetilde{\mu}_{s,2} \end{bmatrix}. \tag{4.22}$$

Using the defined signals in (4.19)-(4.22), the generalized plant representation was determined using the Robust Control Toolbox in MATLAB® version R2022b. The full plant representation is shown in (B.1)-(B.11) of the Appendix.

Selection of weight vectors $\mathbf{w}_1, \mathbf{w}_2$ in Fig. 3.9 was determined as follows. Measurement noise is included in (4.19) and (4.21), so the determined weight transfer functions are not strictly proper, ensuring the optimal synthesis problem is solvable [48]. For load torques inputs, there is no constraint on the weight assignments. However, since it was desirable to have strong disturbance rejection to this signal, weights for the load torques were used to increase their importance in the optimization problem. The position error is a controlled variable, so its weight transfer function must be strictly proper; the performance of this controlled variable was therefore defined over a limited bandwidth. In addition, weight selection for the position error was selected to limit the maximum gain at zero frequency, to avoid ill-conditioning of the optimization problem. The manipulated variable for the secondary resistance cannot have a large gain at high frequencies, since that would imply a large energy expenditure by the physical actuator; the weight for this variable was therefore selected to have a small (but non-zero) gain at high frequencies.

Using an iterative process to evaluate the system response in terms of peak position error and settling time, suitable weight vectors were determined as:

$$\mathbf{w}_1 = \begin{bmatrix} w_{1,1} & w_{1,2} & w_{1,3} \end{bmatrix} = \begin{bmatrix} 0.16 & 0.16 & 5.73\times10^{-6} \end{bmatrix}, \tag{4.23}$$

where $w_{1,1}, w_{1,2}$ are weights applied to load torques $\widetilde{T}_{L,1}$ and $\widetilde{T}_{L,2}$, respectively; $w_{1,3}$ is applied to the noise signal $\widetilde{n}$; and:

$$\mathbf{w}_2 = \begin{bmatrix} w_{2,1} & w_{2,2} \end{bmatrix} = \begin{bmatrix} \frac{100}{s+0.1} & \frac{0.2s}{s+6283} \end{bmatrix}, \tag{4.24}$$

where $w_{2,1}$ is applied to position error control variable $\delta\widetilde{\theta}_r$ and $w_{2,2}$ is applied to the external resistance manipulated variable $\widetilde{\mu}_{s,2}$. Note that $w_{2,1}$ serves as an integrator with cut-off frequency 0.1 rad/s and DC gain of 1000, while $w_{2,1}$ serves to limit the actuation bandwidth to 1000 Hz.

Chapter 5

Numerical Validation

This chapter describes transient simulation studies used to numerically validate the control strategies outlined in Chapter 4, applied to the CCMM drive with parallel IMs and unequal torque loads under various control and operating conditions. In the case studies that follow, time-domain simulations were performed in MATLAB®, version R2021b. The central converter was modeled as a six-switch, four-quadrant inverter with ideal (fully-on or fully-off) switches. The external resistor circuits were also modeled as ideal switches and snubbing was neglected; it was also assumed herein that the value of r in Fig. 4.3 was suitably large to meet the desired fast-average external resistance command. Firstly, the proposed synchronization method is tested using the proportional-integral control described in section 4.1. Then, the optimal control design is verified under the same conditions applied to the PI case.

5.1 Proportional-Integral Controller

In the first two case studies, the CCMM system contained three actuation lines. The drive motor for each actuation line consisted of identical 15 hp IMs. Motor $n = 1$ was arbitrarily selected to be the primary motor in these studies; motors $n = \{2, 3\}$ served as secondary motors. The mechanical load connected to each drive motor shaft was represented by an equivalent load torque. Parameters for the motors and all control algorithms used in these studies are listed in the Appendix A. The purpose of this first set of numerical results is to show the feasibility of the position synchronization method and serve as a proof of concept. Therefore, the PI gains were tunned in an iterative way until the transient response of the position synchronization error was considered satisfactory.

5.1.1 Case Study I: Unequal Torque Loads with Voltage-Controlled Drive

In this case study, all IMs were driven by the central converter using the CVHz strategy described in section 3.1.2 and depicted in Figs. 3.3-3.4, in combination with the position synchro-

nization scheme outlined in section 4.1. Converter switching states for implementing the voltage control were generated using sine-triangle modulation with 3rd harmonic injection [35].

In this study, commanded speed of $\omega_{rm}^{*} = 188.5\,\text{rad/s}$ was first applied at $t = 0.1\,\text{s}$, with zero torque load applied to each motor. After reaching steady-state commanded rotor speed, at $t = 4.0\,\text{s}$, torque loads of $T_{L,1} = 1.0T_{\text{rated}}, T_{L,2} = 0.8T_{\text{rated}}, T_{L,3} = 0.7T_{\text{rated}}$ were then applied, where $T_{\text{rated}} = 67.5\,[\text{N·m}]$ was the torque rating of the (identical) IMs. Transient responses are shown in Figs. 5.1-5.7.

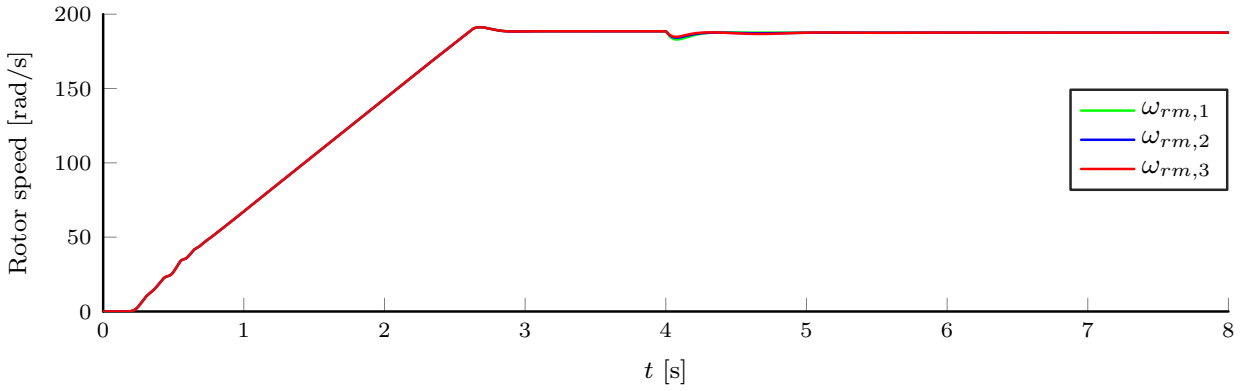

Figure 5.1: Mechanical rotor velocities, including start-up; voltage-source control.

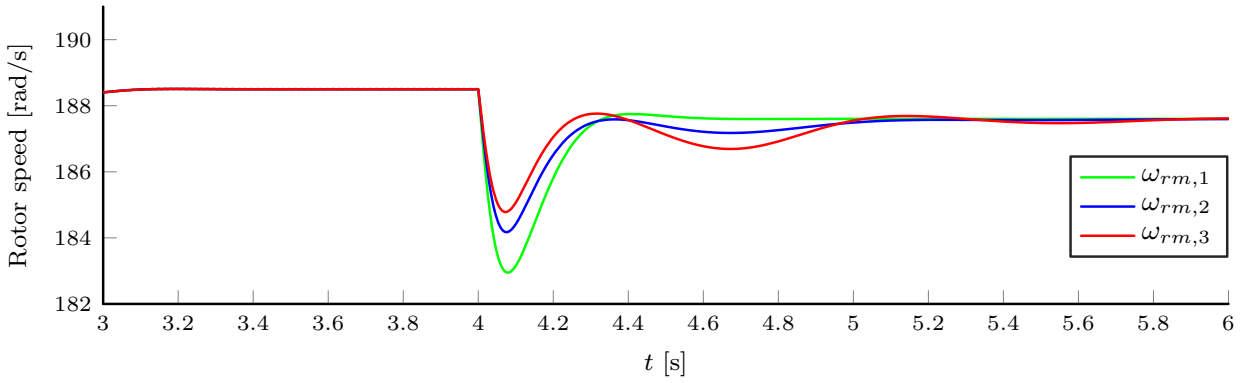

Figure 5.2: Mechanical rotor velocities (zoomed-in); voltage-source control.

Fig. 5.1 shows mechanical rotor speed for all motors including the initial start-up period; Fig. 5.2 provides a zoomed-in view of the response after the unequal torque loads are applied. As

shown in Fig. 5.2, the transient rotor response resolves in approximately 2 s. All IM rotor speeds reach approximately 187.6 rad/sec after reaching steady-state; the small steady-state speed error (0.5%) is a result of the open-loop speed control used in this study (see Fig. 3.3).

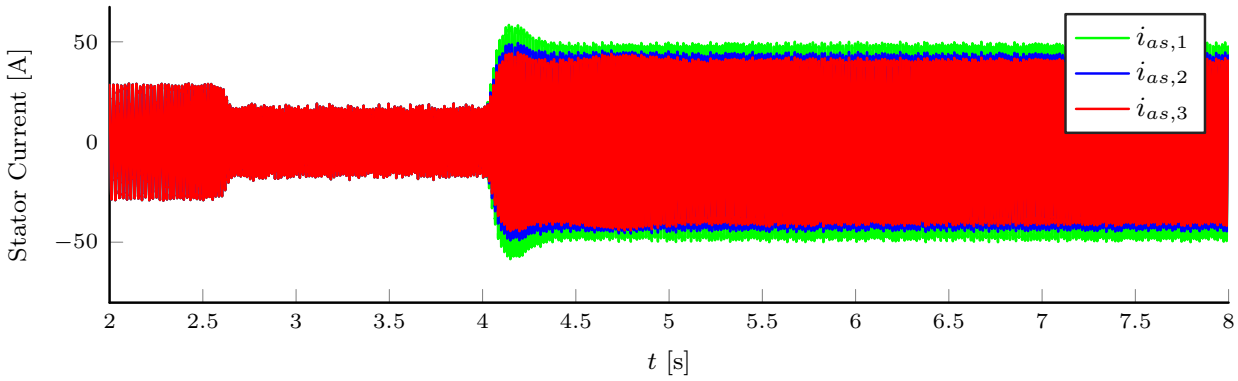

Figure 5.3: Phase a stator currents; voltage-source control.

In Fig. 5.3, $a-$phase stator currents are shown for all motors. After 4 s, the motor currents display different peak currents; these differences correspond to the application of unequal load torques and differences in motor input impedances.

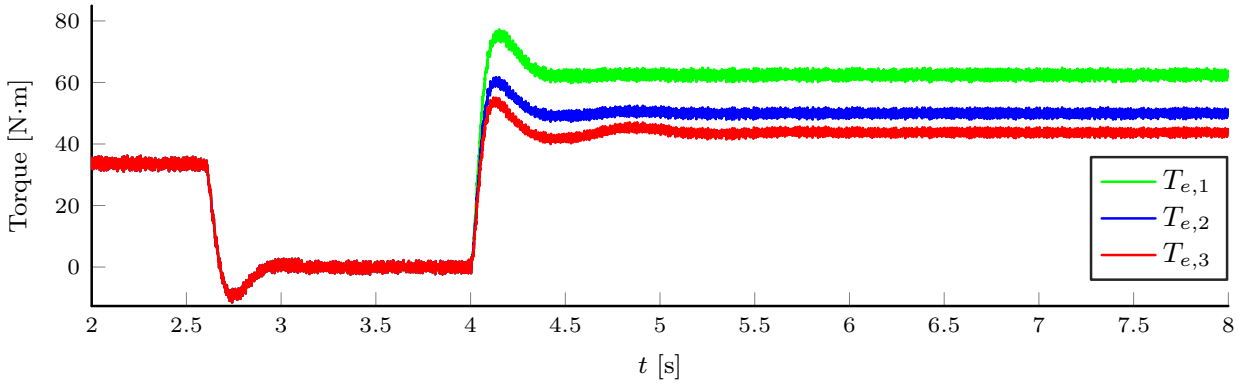

Figure 5.4: Electromagnetic torques; voltage-source control.

Fig. 5.4 shows electromagnetic torque for all motors. The initial electromagnetic torques ($t < 4$ s) are responsible for initial acceleration of the motors. After $t = 4$ s, each motor produces a different electromagnetic torque response, corresponding to the differences in load torques and motor input impedances.

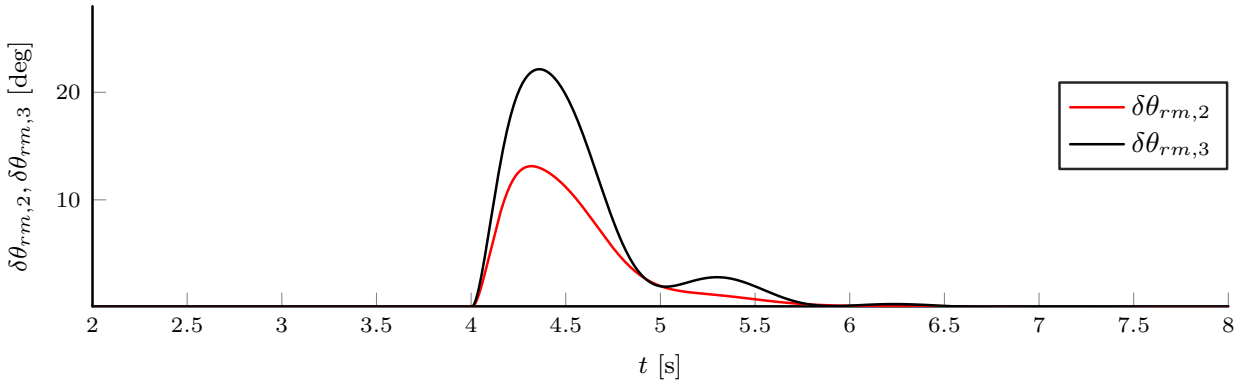

Figure 5.5: Individual angle differences; voltage-source control.

Individual rotor angle differences for the secondary motors, referenced from the primary motor, are shown in Fig. 5.5. Just after $t = 4\,\text{s}$, synchronization errors are initially observed, before being resolved by the proposed control scheme after approximately 1.5 s. Initial transient angular difference behavior is a result of unequal applied load torques; larger torque differences between primary motor load torque and each secondary motor load torque result in a correspondingly higher peak transient angle difference. In this case study, the maximum angle differences relative to the second and third motor, respectively, were 13.1 and 22.1 deg.

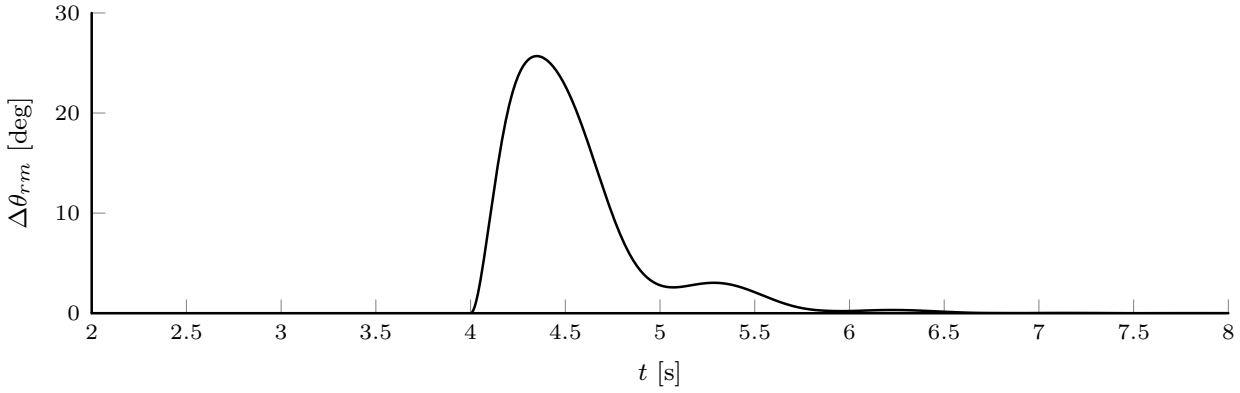

Figure 5.6: Normed angle difference; voltage-source control.

Fig. 5.6 shows the normed angle error; the normed error was observed to reach a peak value of 25.7 deg after the load torques are applied. As shown in Fig. 5.6, the normed error is then driven

to zero by the proposed control; $\Delta\theta_{rm} < 0.5$ deg approximately 1.5 s after the torques are applied, eventually converging to $\Delta\theta_{rm} \approx 0$.

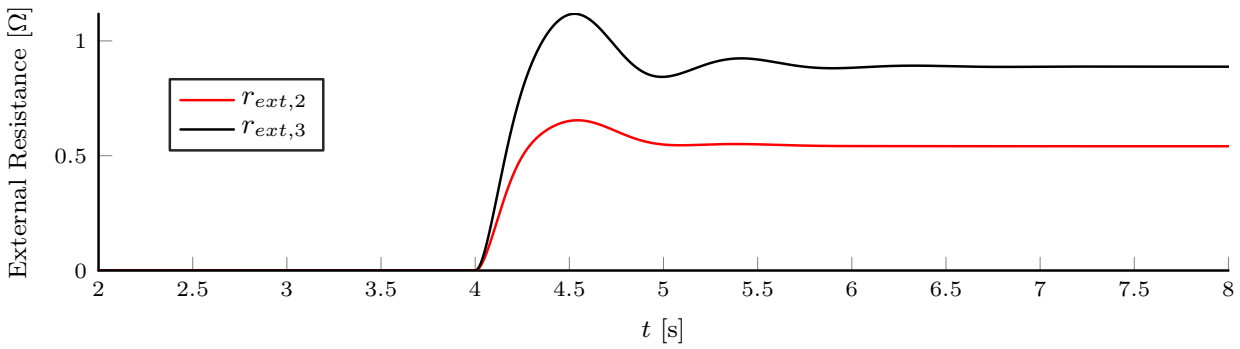

Figure 5.7: External resistance values; voltage-source control.

Finally, Fig. 5.7 shows the external resistance values for the two secondary motors. For $t < 4\,\text{s}$, no external resistance is needed since the load torques are balanced (all zero). For $t \geq 4\,\text{s}$, external resistances are applied to provide position synchronization; higher differences between primary load torque and secondary load torque result in a higher value of external resistance to ensure steady-state position synchronization. Motor 2 presents a maximum resistance value of $0.65\,\Omega$ and a steady-state value of $0.54\,\Omega$, while for motor 3 the values are $1.12\,\Omega$ and $0.88\,\Omega$.

5.1.2 Case Study II: Unequal Torque Loads with Current-controlled Drive

In this case study, the IMs were all driven by the central converter using the IDFOC control strategy described in section 3.1.3 and depicted in Figs. 3.5-3.6, in combination with the position synchronization scheme described in section 4.1. Switching states of the converter to achieve the desired current commands in this case study were generated using a hysteresis-band modulation strategy [35].

The identical speed commands and torque loading conditions used in case study I were applied to the IMs after reaching steady-state, again at $t = 4\,\text{s}$. Transient responses are shown in Figs. 5.8-5.14.

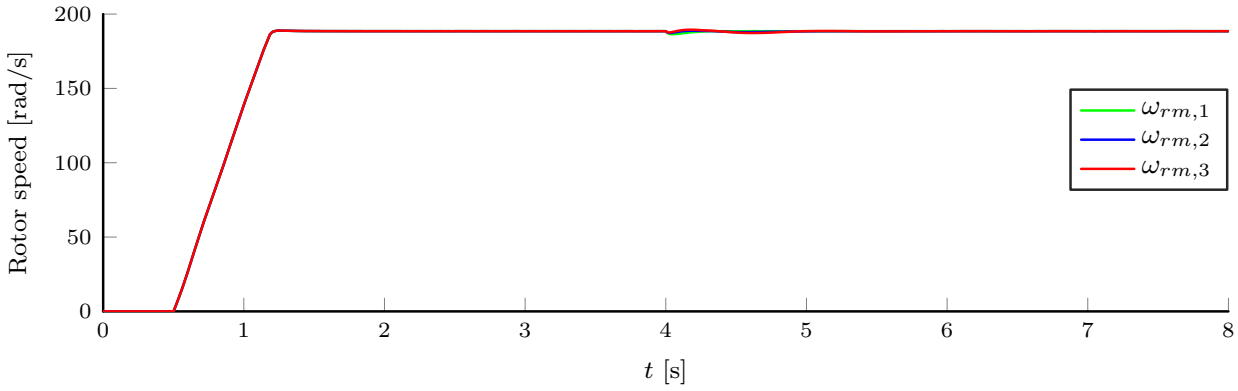

Figure 5.8: Mechanical rotor velocities, including start-up; current-source control.

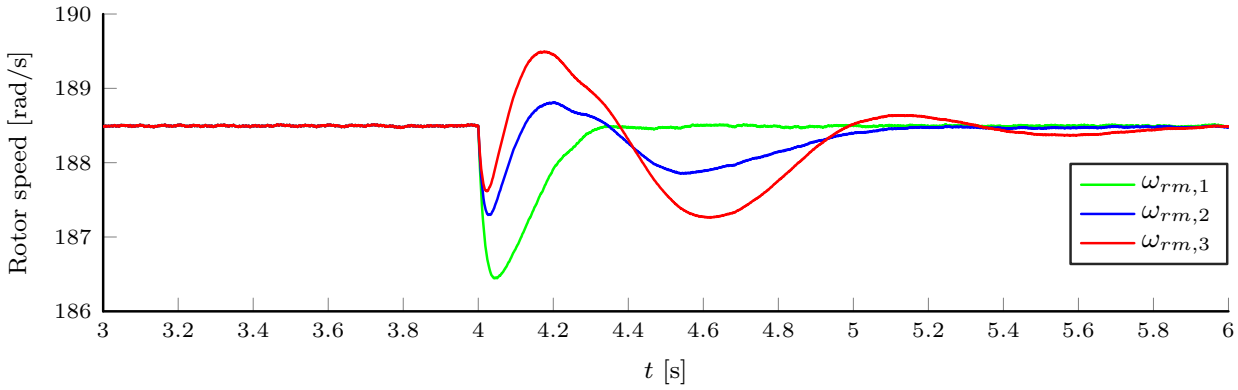

Figure 5.9: Mechanical rotor velocities (zoomed-in); current-source control.

Fig. 5.8 shows mechanical rotor speed for all motors including the initial start-up period; Fig. 5.9 provides a zoomed-in view of the response after the unequal torque loads are applied at $t = 4.0\,\text{s}$. As shown in Fig. 5.9, the transient rotor response resolves in approximately 2 s. All IM rotor speeds reached approximately 188.5 rad/sec in steady-state; close speed tracking (compared to the previous case study) was a result of the closed-loop speed control used in this study (see Fig. 3.6).

In Fig. 5.10, $a-$phase stator currents are shown for all motors. After $t = 4\,\text{s}$, the motor currents display different peak currents; these differences correspond to the application of unequal load torques.

Fig. 5.11 shows electromagnetic torque for all motors. The initial electromagnetic torques ($2 \leq t < 4\,\text{s}$) is zero for all motors since they have already reached free-acceleration speed (refer

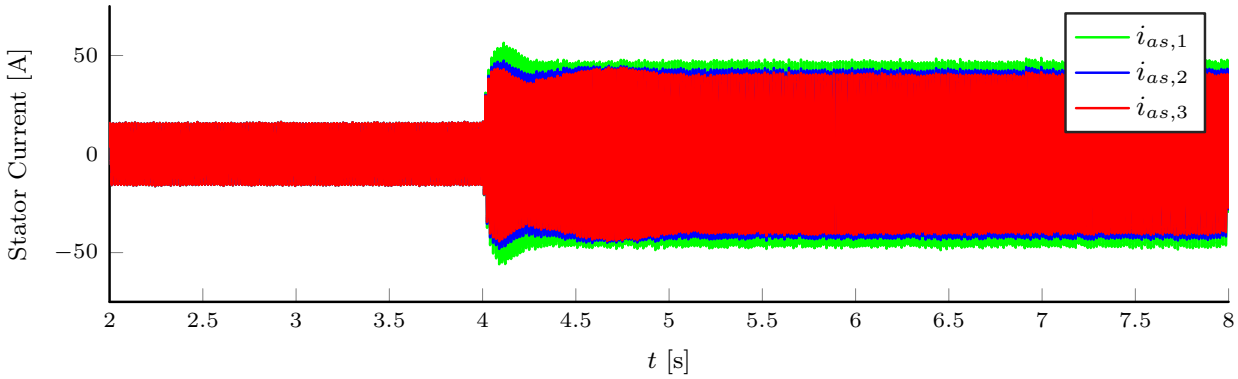

Figure 5.10: Phase a stator currents; current-source control.

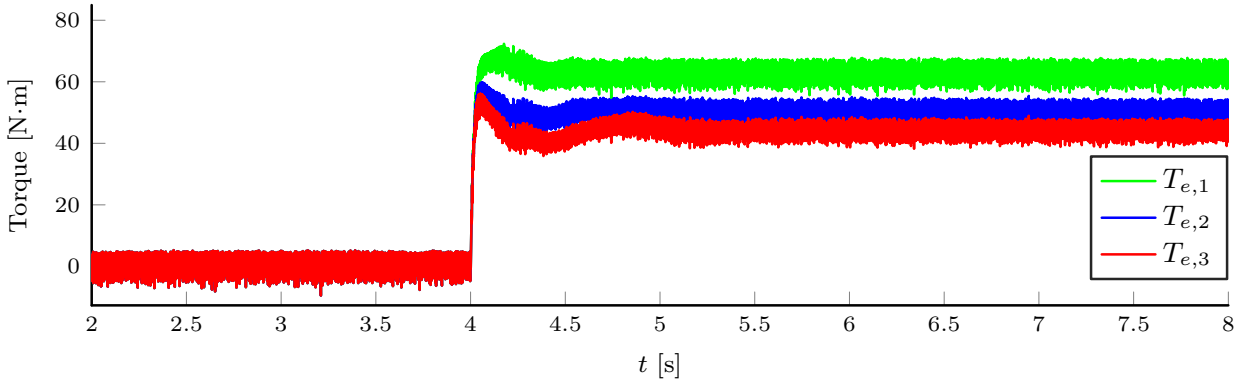

Figure 5.11: Electromagnetic torques; current-source control.

to Fig. 5.8). After $t = 4\,\text{s}$, each motor produces a different electromagnetic torque response, corresponding to the differences in load torques and motor impedances.

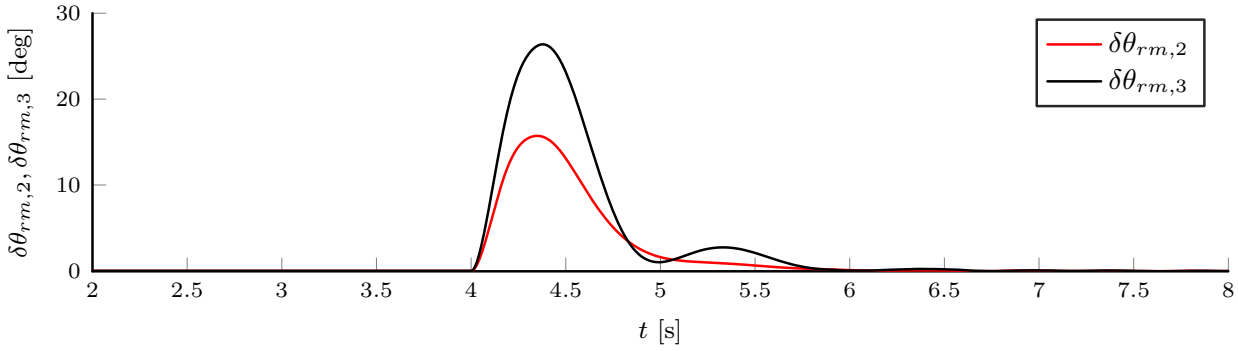

Figure 5.12: Individual angle differences; current-source control.

Individual rotor angle differences for the secondary motors, referenced from the primary motor, are shown in Fig. 5.12. Just after $t = 4\,\text{s}$, synchronization errors are initially observed, before

being resolved by the proposed control scheme after approximately 1.5 s. As in the previous case study, transient angular difference behavior in the IDFOC with combined synchronization control is a result of unequal applied load torques; larger torque differences between primary motor load torque and each secondary motor load torque result in a correspondingly higher peak transient angle difference. In this case study, the maximum angle differences relative to the second and third motor, were 15.7 and 26.4 deg, respectively.

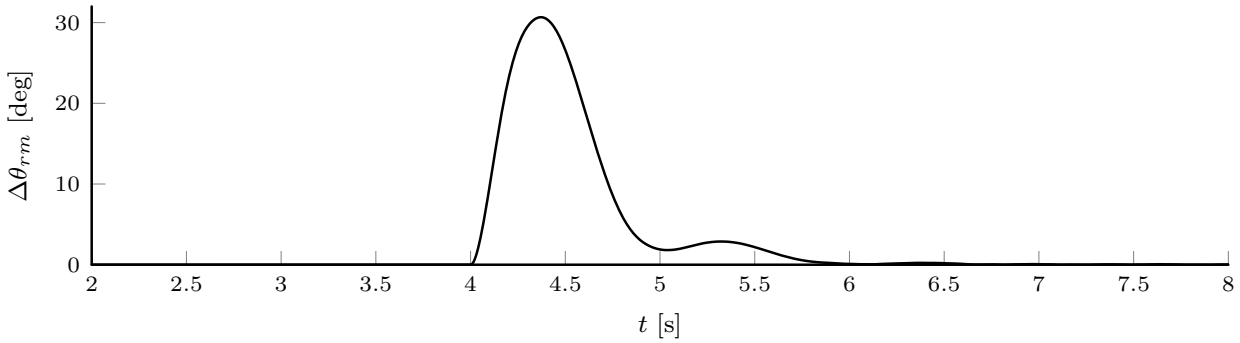

Figure 5.13: Normed angle difference; current-source control.

Fig. 5.13 shows the normed angle error; the normed error was observed to reach a peak value of 30.7 deg after the load torques are applied. As shown in Fig. 5.13, the normed error is then driven to zero by the proposed control; $\Delta\theta_{rm} < 0.25$ deg approximately 1.5 s after the torques are applied, eventually converging to $\Delta\theta_{rm} \approx 0$.

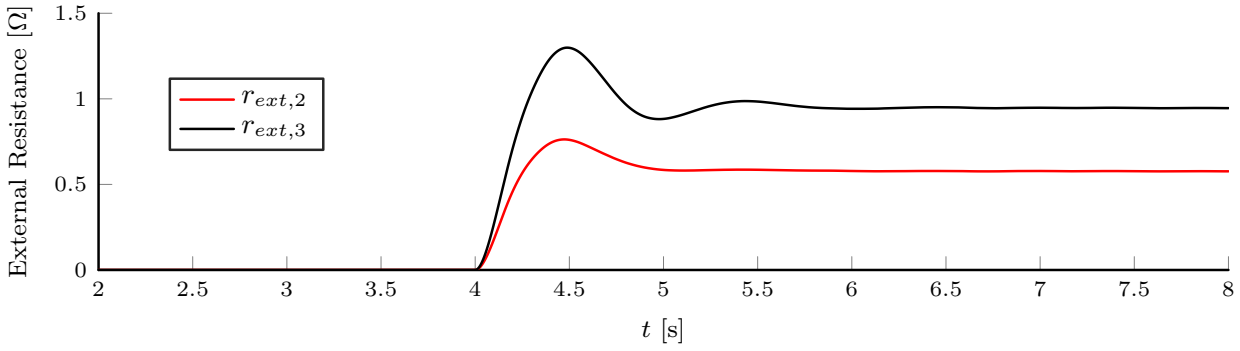

Figure 5.14: External resistance values; current-source control.

Finally, Fig. 5.14 shows the external resistance values for the two secondary motors. For $t < 4\,\mathrm{s}$, no external resistance is needed since the load torques are balanced (all zero). For $t \geq 4\,\mathrm{s}$, external resistances are applied to provide position synchronization; higher differences between primary load torque and secondary load torque result in a higher value of external resistance to ensure steady-state position synchronization. Motor 2 presents a maximum resistance value of $0.76\,\Omega$ and a steady-state value of $0.58\,\Omega$, while for motor 3 the values are $1.30\,\Omega$ and $0.94\,\Omega$.

5.1.3 Case Study III: Maximum Torque Sufficiency

As described in section 4.1, and also indicated in Figs. 4.1-4.2, IM position synchronization achieved by changing external stator resistances results in a subsequent change in the maximum steady-state torque achieved by the motor. It is therefore necessary to consider whether the control strategy proposed in this work ensures that the maximum electromagnetic torque is sufficient to overcome the torque load, even in the case of abrupt changes in load torque. This case study examines maximum torque sufficiency of the approach under an abrupt change in load torque.

Herein, two 15 hp IMs are driven using a CVHz drive (the electrical machine, drive and its control parameters are identical to those used in case study I). Motor 1 is designated as the primary motor and motor 2 is designated as the secondary throughout this study. The system is started from a no-load condition. At $t = 4\,\mathrm{s}$, the following unbalanced load torques are applied: $1.0T_{rated}$ is applied to the primary motor and $0.6T_{rated}$ to the secondary. After reaching steady-state and achieving $\Delta\theta_{rm} \approx 0$ position synchronization error, the load in the secondary motor is instantaneously stepped to $0.9T_{rated}$ at $t = 10\,\mathrm{s}$. The resulting dynamic behavior is shown in Figs. 5.15-5.18.

Fig. 5.15 shows the electromagnetic torque of the motors; the electromagnetic of the secondary motor is seen to increase after the step-change in load after $t = 10\,\mathrm{s}$.

Fig. 5.16 shows the normed angle error. After the first torque load condition was applied at $t = 4\,\mathrm{s}$,the normed error reached a peak of 34.1 deg; after the second load condition at $t = 10\,\mathrm{s}$, the maximum normed error was 35.9 deg. As shown in Fig. 5.16, the normed error is driven to zero by the proposed control under both conditions.

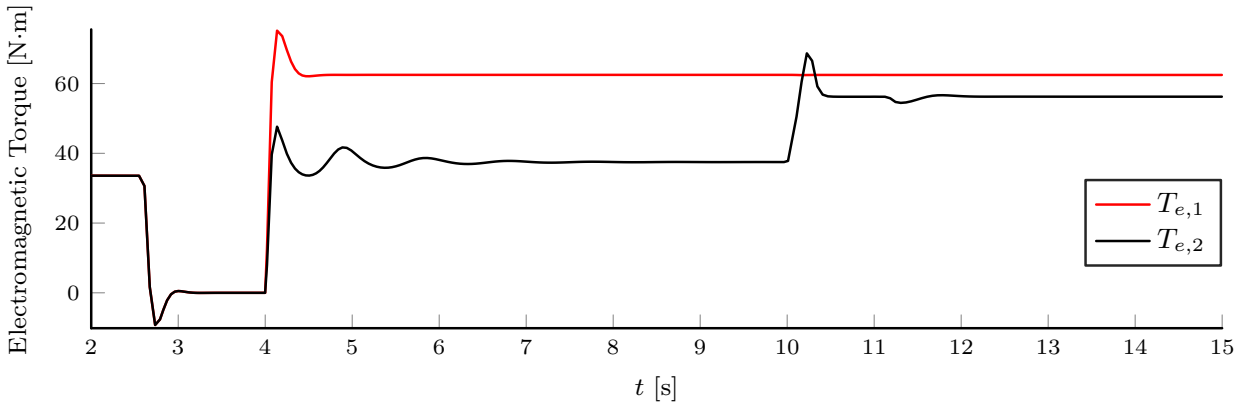

Figure 5.15: Electromagnetic torque: torque sufficiency study.

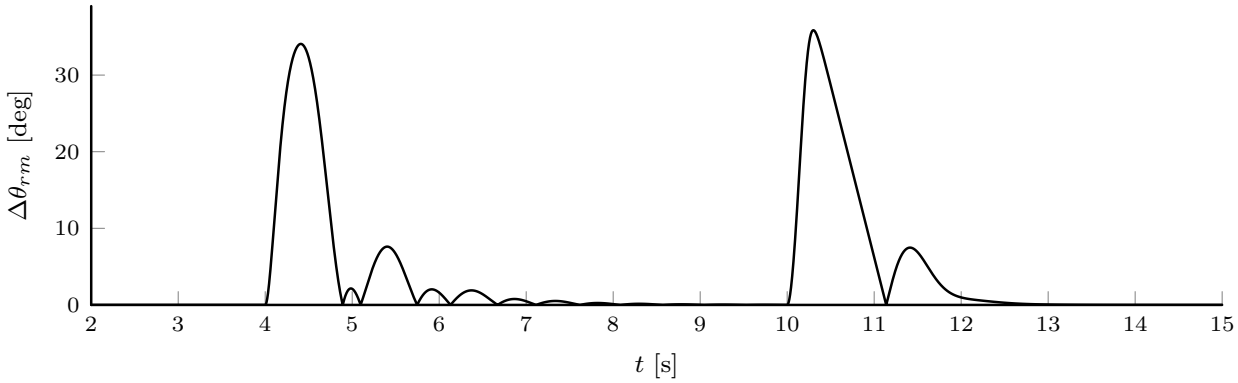

Figure 5.16: Normed angle difference: torque sufficiency study.

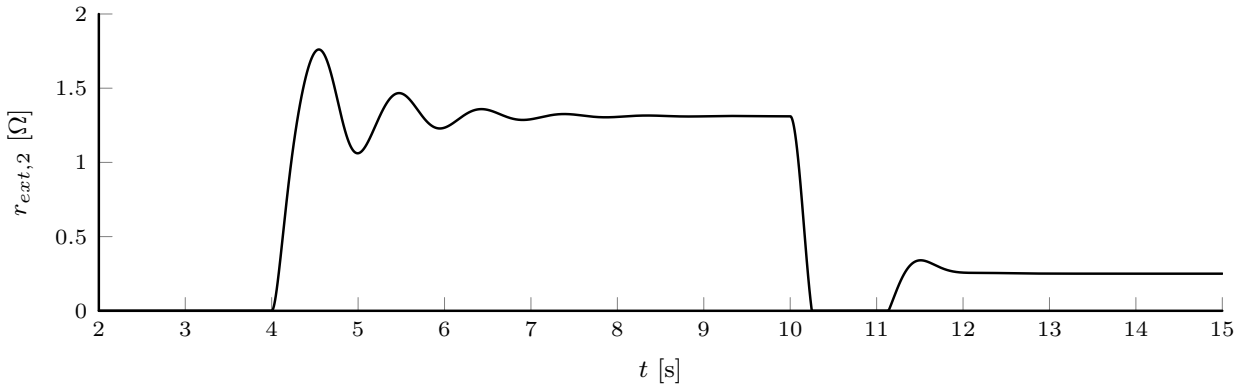

Figure 5.17: External stator resistance of secondary motor: torque sufficiency study.

Fig. 5.17 shows the dynamic external resistance value of the secondary motor (the primary motor resistance is held to zero). The steady-state value of $r_{ext,2} = 1.31\,\Omega$ just prior to the step change in load at $t = 10\,\text{s}$; afterwards, the resistance converges to a decreased steady-state value of $r_{ext,2} = 0.25\,\Omega$. Referring to Fig. 4.2, a decrease in stator resistance results in an increase in

maximum torque of the motor, which is also apparent in Fig. 5.15. Therefore, it can be seen that the action of the proposed control to decrease stator resistance after a change in load torque provides a restoring torque to compensate for an increase in the applied load torque. To further illustrate this point, a graphical depiction of the steady-state electromagnetic torque curves (which are a function of external stator resistance) and the applied torque loads in the study above are shown in Fig. 5.18, demonstrating that the maximum torque for each case is large enough to sufficiently overcome the applied load.

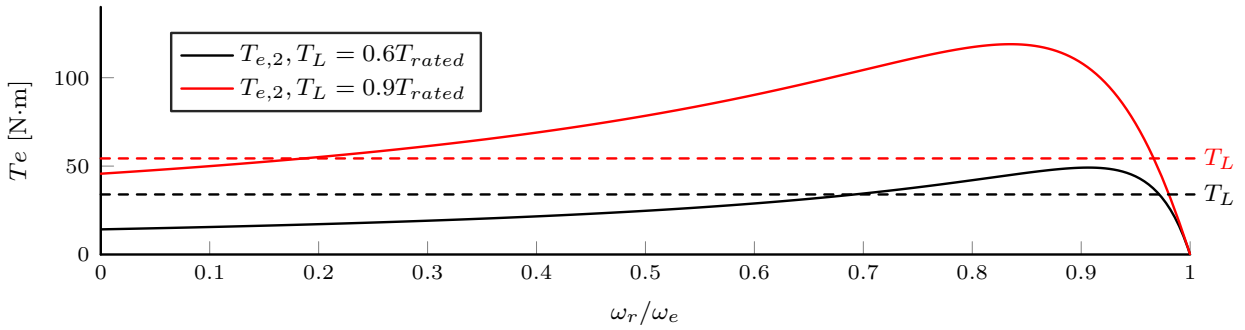

Figure 5.18: Electromagnetic torque of secondary motor for different values of external stator resistance: torque sufficiency study.

5.1.4 Case Study IV: Primary-Secondary Dynamic Selection

This case study aims to account for the possibility of dynamic transitions between primary and secondary motor designations, which can occur under known wind force trajectories during post-deployment of the EM-TRAS system (see Section 6.2). In this scenario, dynamic primary-secondary motor selection and re-synchronization of rotor positions are required. In the proposed approach, when the position error is larger than a pre-defined hysteresis band, the first machine with this corresponding error is selected as the new primary. Fig. 5.19 shows a flowchart that describes the proposed method for primary-secondary motor dynamic selection. At first, one of the motors, say motor 1, is arbitrarily selected as the primary motor, while the others are assigned as secondary. Then the position differences between each secondary motor and the primary are calculated. If one of those differences is above a given threshold, the motor corresponding to that difference

is updated as the primary; otherwise, the current primary motor is kept unchanged. Finally, the external resistances of the secondary motors are determined from the position differences (e.g., using a PI control) and the primary external resistance is set to zero.

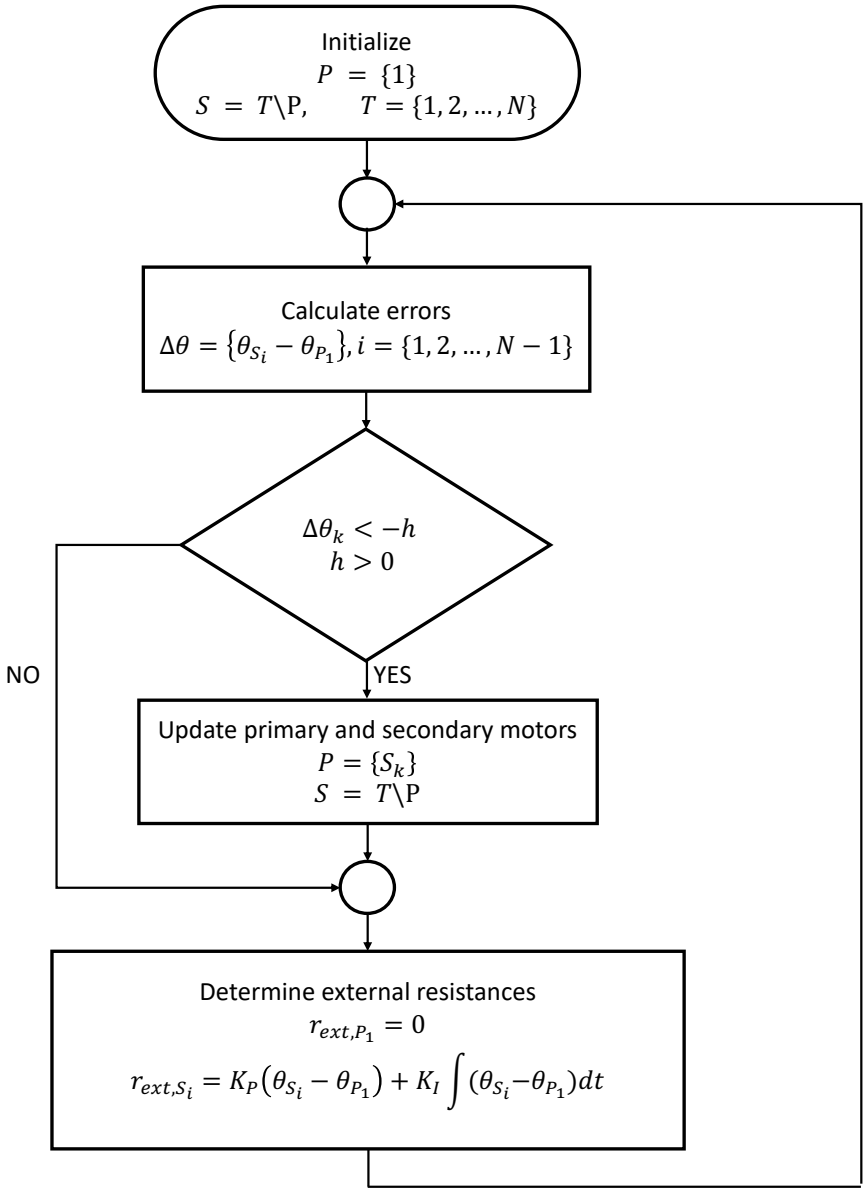

Figure 5.19: Flowchart of the proposed method for primary-secondary motor dynamic selection.

The proposed approach was validated in time-domain transient simulation on a set of three parallel 15 hp IMs, subject to differing load torque profiles, with the central converter implementing IDFOC. Torque loads were simulated as follows: before 2 s all motors had zero load torque; between 2 s and 4 s, $T_{L,1} = 1$ pu, $T_{L,2} = 0.8$ pu, $T_{L,3} = 0.7$ pu; between 4 s and 7 s $T_{L,1} = 0.7$ pu, $T_{L,2} = 1$ pu, $T_{L,3} = 0.8$ pu; after 7 s, $T_{L,1} = 0.8$ pu, $T_{L,2} = 0.7$ pu, $T_{L,3} = 1$ pu.

Fig. 5.20 shows the angle differences of the three IMs during the torque transitions. Note how the position errors present discontinuities right after each of the torque transitions. This is caused by the update in the primary-secondary assignments, which forces the position errors to be calculated with respect to a different primary motor. However, the position errors are driven to zero (or close to) before the next torque transition.

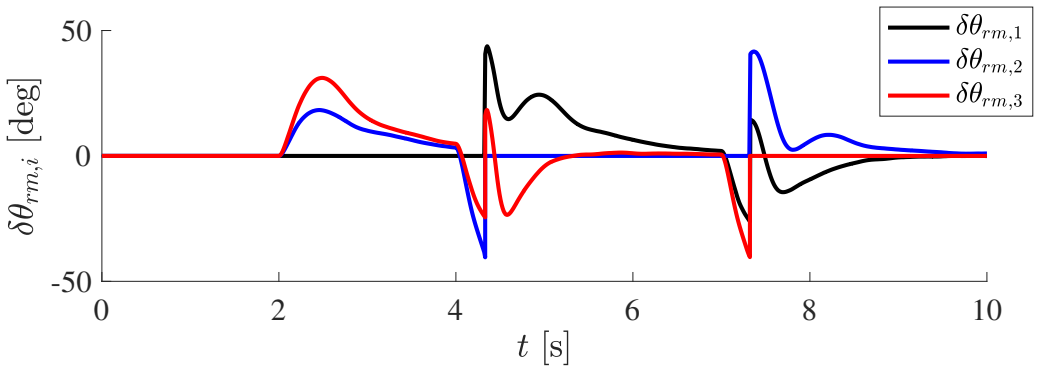

Figure 5.20: Rotor position errors of the induction machines during torque transitions.

Fig. 5.21 shows the normed angle difference. The maximum normed position error reached 48 deg, in the last torque transition.

Fig. 5.22 shows the external resistors' values for the three motors. Note the symmetry in the waveforms of the resistances' responses, which is a direct result of the proposed approach and the load torque transitions used in this case study.

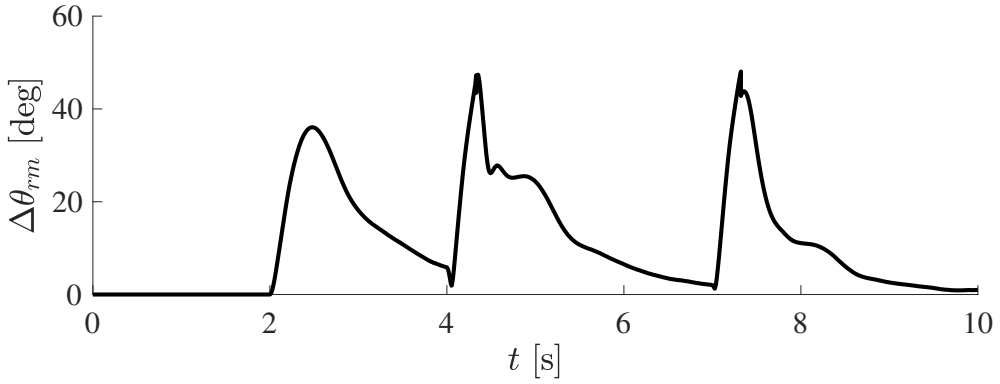

Figure 5.21: Normed angle difference during torque transitions.

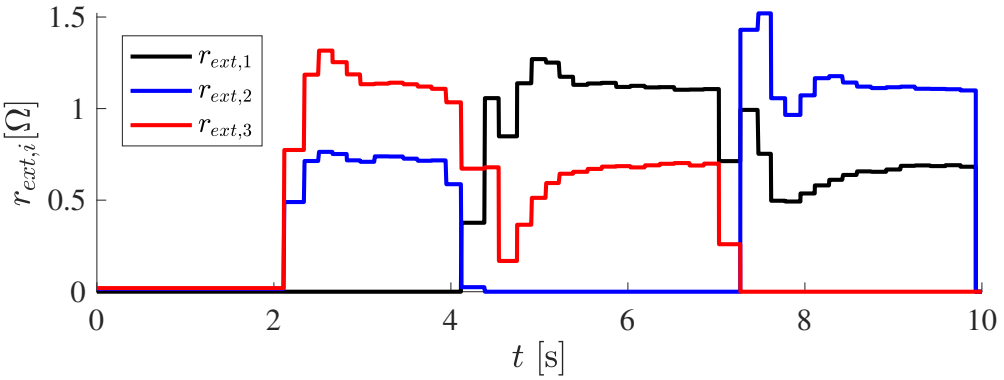

Figure 5.22: External stator resistances during torque transitions.

From the results shown for this case study, it can be seen that the proposed approach was able to correctly assign the primary and secondary machine designations and the resistive control strategy was able to achieve re-synchronization of rotor position at each torque transition.

5.2 $\mathcal{H}_\infty$ Controller Performance

This section describes transient simulation studies used to demonstrate the performance of the control design described in section 4.3. Controller parameters for the primary control strategy implemented by the central converter are given in Tables A.2-A.4. The parameters used in the external resistor circuit control are given in Tables A.5 and A.7. The IMs consisted of identical

15 hp machines, with parameters given in Table A.1. Machine $n=1$ was selected to be the primary machine in these studies; machines $n = \{2, 3\}$ served as secondary machines. In the following analyses, secondary machine speeds are considered to have converged with the primary machine speed when their differences are within (and remain within) 1 rpm. Similarly, position converge is defined for position differences remaining below $0.25°$. The mechanical load connected to each machine was represented by an equivalent mechanical load torque.

In the following studies, after the machines reach steady-state no-load speed (designated $t = 0$ s), load torques of $T_{L,1} = 1.0$ pu, $T_{L,2} = 0.8$ pu, and $T_{L,3} = 0.7$ pu were applied. The external stator resistance circuits for the secondary machines in these studies were controlled by switching signals obtained from the $\mathcal{H}_\infty$ optimal controller.

5.2.1 Case Study I: Voltage-controlled Drive

In this case study, the CCMM converter was controlled using the Compensated Volts-per-Hertz (CVHz) method to provide regulated stator voltages to the parallel IMs. Commanded speed was $\omega^*_{rm} = 1800$ rpm. Fig. 5.23 shows computed rotor speeds for the three machines. As shown in Fig. 5.23, all machines converge to the speed of the primary machine in approximately 1.0 s.

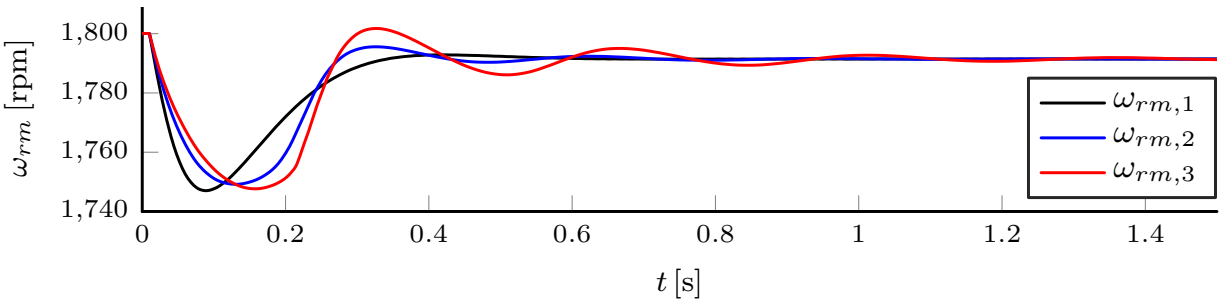

Figure 5.23: Computed rotor speeds using CVHz as primary control.

Fig. 5.24 shows the relative position errors (with respect to the primary machine) for the two secondary machines. The peak errors were $3.9°$ and $6.0°$ for machines 2 and 3, respectively. The transients shown in Fig. 5.24 extinguished in approximately 1.2 s. Machine 3 presented a higher

relative position error than machine 2 because of the higher load torque difference with respect to the primary machine.

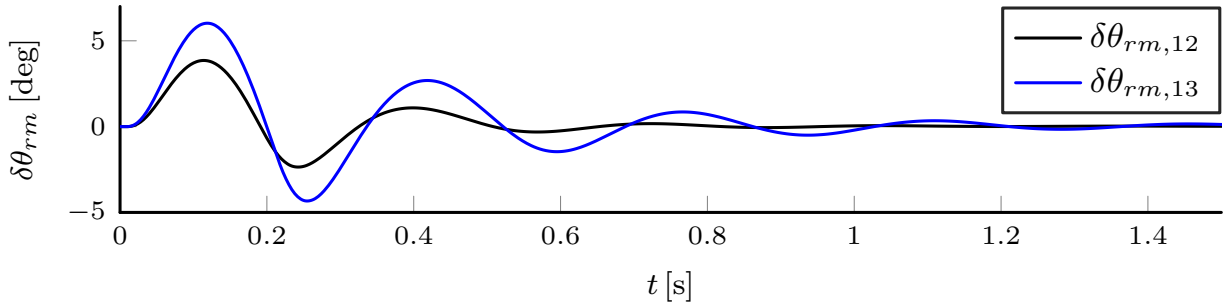

Figure 5.24: Computed relative rotor position error using CVHz.

Fig. 5.25 shows the normed position error. The maximum normed position error was 7.1°.

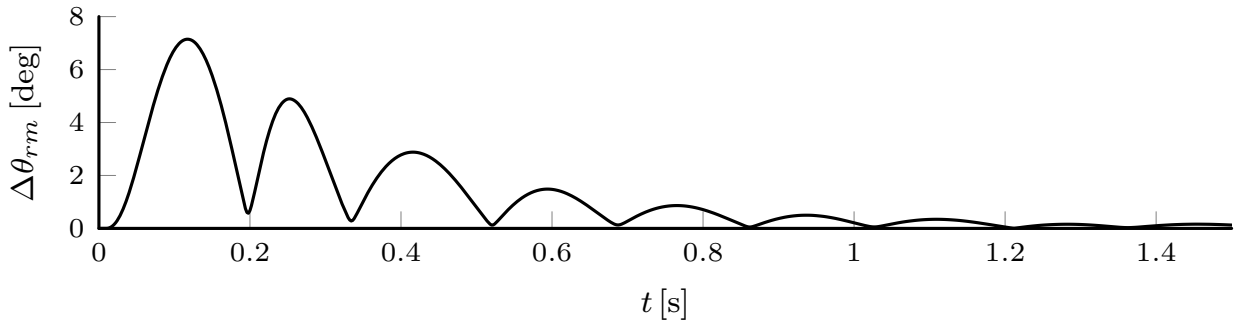

Figure 5.25: Computed norm of rotor position error using CVHz.

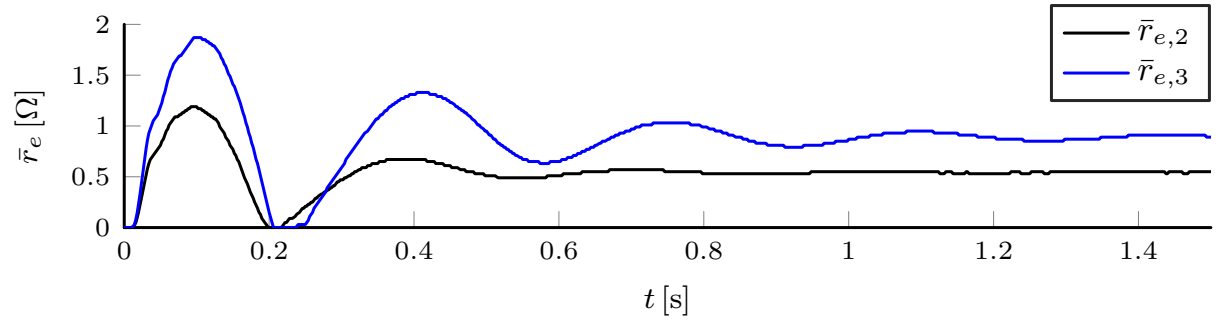

Figure 5.26: Computed fast-average external resistances using CVHz.

Fast-average a-phase external stator resistance of the secondary machines is shown in Fig. 5.26. As shown in Fig. 5.26, $\widetilde{r}_{e,3} > \widetilde{r}_{e,2}$ after the system stabilizes because of the higher load torque difference of machine 3, as expected.

5.2.2 Case Study II: Current-controlled Drive

In this case study, the CCMM converter was controlled using an Indirect Field-Oriented Control (IDFOC) method to provide regulated stator currents to the primary machine. In this control strategy, there is also closed-loop speed control; herein $\omega^*_{rm} = 1800\,\text{rpm}$. Fig. 5.27 shows computed rotor speeds for the three machines. As shown in Fig. 5.27, the transient excursion extinguished in $0.9\,\text{s}$; the reduction in the excursion compared with CVHz is attributable to the addition of closed-loop speed control.

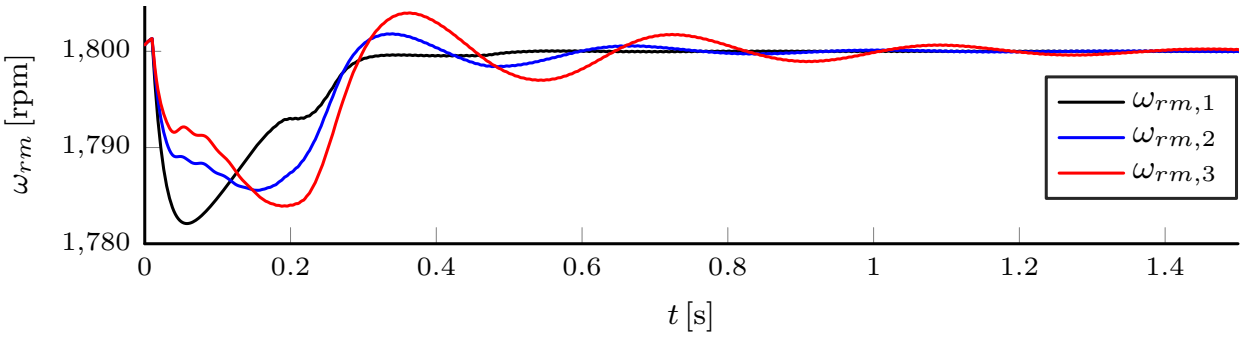

Figure 5.27: Computed rotor speeds using IDFOC as primary control.

Fig. 5.28 shows the relative position errors (with respect to the primary machine) for the two secondary machines. The peak errors were $2.7°$ and $4.3°$ for machines 2 and 3, respectively; these peak errors were approximately 30% less than those observed using the CVHz control. The transient in Fig. 5.28 extinguished in approximately $0.9\,\text{s}$ (faster than the CVHz study). Again, machine 3 presented a higher relative position error than machine 2 because of the higher load torque difference with respect to the primary machine.

Fig. 5.29 shows the normed position error. The maximum normed error in this study was $5.1°$, a decrease of 30% when compared to the CVHz control.

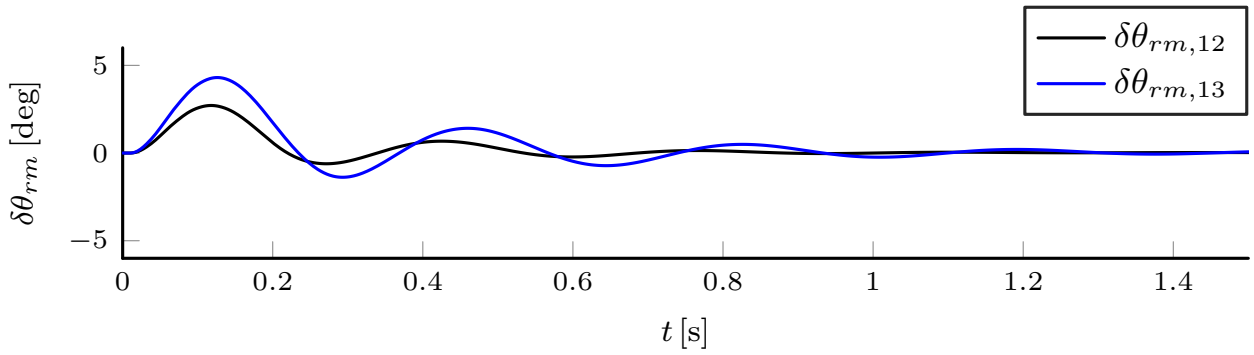

Figure 5.28: Computed relative rotor position error using IDFOC.

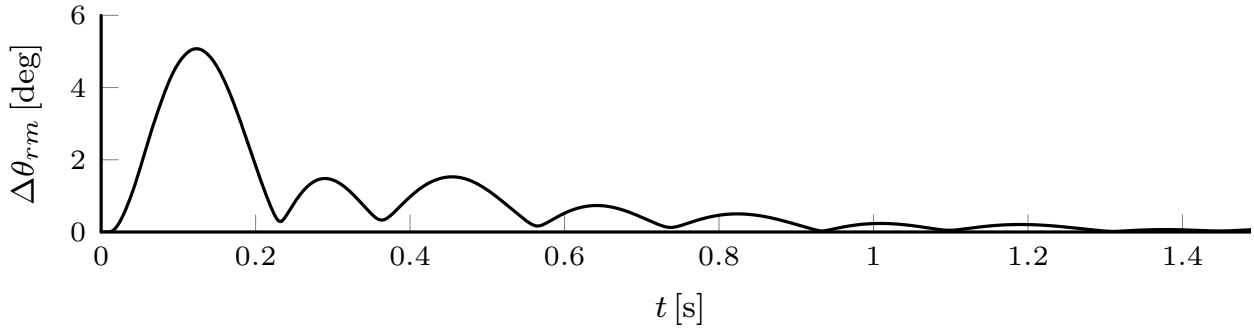

Figure 5.29: Computed norm of rotor position error using IDFOC.

Fast-average a-phase external stator resistance of the secondary machines is shown in Fig. 5.30. As shown in Fig. 5.30, the overshot of the required external resistances was smaller compared to the CVHz control. Again, $\widetilde{r}_{e,3} > \widetilde{r}_{e,2}$ after the system stabilizes because of the higher load torque difference of machine 3, as expected.

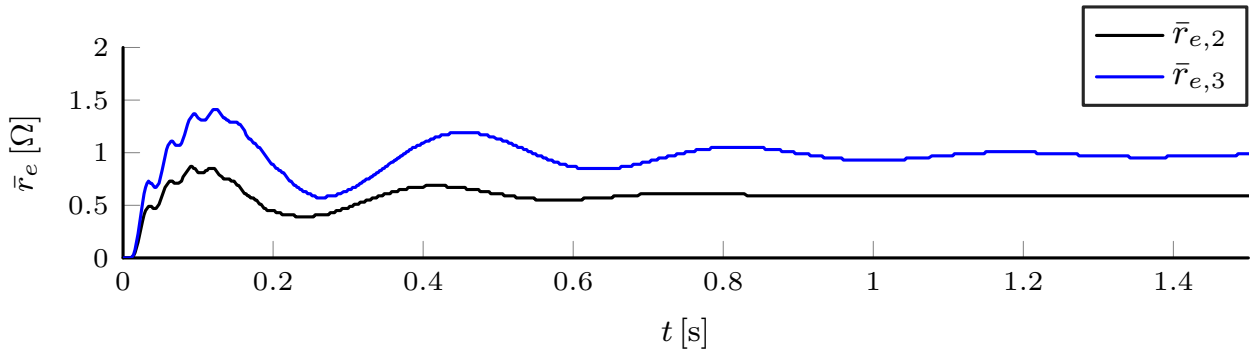

Figure 5.30: Computed fast-average external resistances using IDFOC.

In comparison to the proportional-integral control strategy described in section 5.1, the control response shown in the foregoing case studies is improved for both CVHz and IDFOC. In particular, the maximum normed position error during rotor synchronization was decreased: from $25.7°$ to $7.1°$ using CVHz and $30.7°$ to $5.1°$ using IDFOC. In addition, convergence in the normed position error was achieved faster: $2.39\,\mathrm{s}$ versus $1.15\,\mathrm{s}$ using CVHz and $1.89\,\mathrm{s}$ versus $0.88\,\mathrm{s}$ for IDFOC. A drawback of the proposed control compared to the proportional-integral control is a larger required base resistance: $2\,\Omega$ versus $1.5\,\Omega$. The increase in resistance for the resistor element would marginally impact the initial controller design cost, and potentially result in larger energy loss during synchronization. However, because the thrust-reverse operation is expected to be used infrequently, it is the view of the authors that position synchronization error is a more important metric than energy loss when evaluating alternatives for this application.

Also noted in the performance summarized above when comparing CVHz and IDFOC using the optimal control design, the IDFOC method with closed-loop speed response demonstrated superior control performance in terms of peak relative and normed position errors and smaller required external resistance compared to CVHz. In addition, settling time was lower using IDFOC.

5.3 External resistor analysis

The motivation to use external resistors in series with the stator of the induction machine is that it is possible to decrease the slope of the torque vs. speed curve, as presented in Section 4.1. From Fig. 4.2, it is possible to infer that, for fixed load torque, the steady-state speed of the machine decreases as the external resistance increases in the motor mode ($T_e > 0\,\mathrm{Nm}$), which is the region shown in Fig. 4.2. On the other hand, in the generator mode, as the slope of the curve decreases, the speed is expected to increase. Fig. 5.31 illustrates the same concept as Fig. 4.2 (for the same 15 hp machine), but in the generator mode. Note how the slope of the torque curves also decreases as more external resistance is added to the stator.

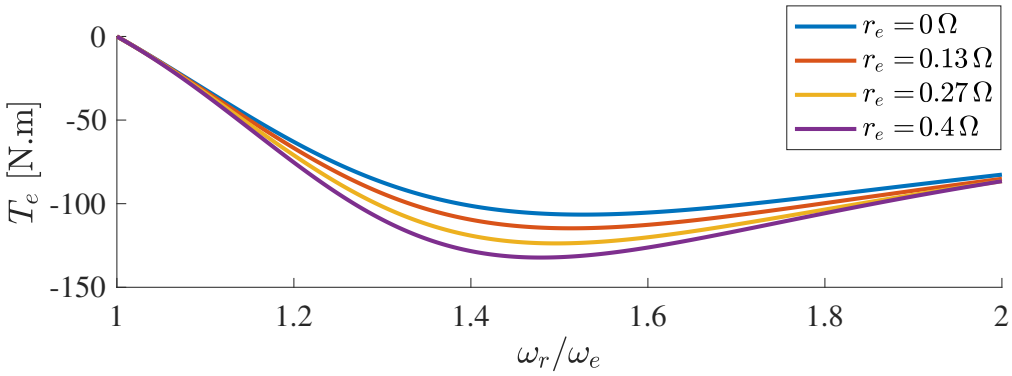

Figure 5.31: Steady-state torque vs. speed for different values of external stator resistance in generator mode.

However, a deeper analysis is done to verify this assumption. Consider the following steady-state equation for the electromagnetic produced by the induction machine [49]:

$$T_e = \frac{3}{\omega_{syn}} \cdot \frac{V_{th}^2}{(r_{th} + r_r/s)^2 + (X_{th} + X_r)^2} \cdot \frac{r_r}{s}, \tag{5.1}$$

where $\omega_{syn} = (2/P)\omega_e$ is the synchronous speed, which corresponds to the rotational velocity of the magnetic fields inside the induction machine, $s = (\omega_{syn} - \omega_{rm})/\omega_{syn}$ is referred as the slip of the machine, the th subscript corresponds to Thévenin equivalent circuit parameters as seen by the rotor, and $X_{\{\cdot\}}$ is the reactance corresponding to the respective inductance (e.g. $X_r = \omega_e L_r$). The value of the stator resistance r_s includes any potentially added external resistor. The Thévenin parameters can be written as:

$$V_{th} = V_s \frac{X_M}{\sqrt{r_s^2 + X_s^2}} \tag{5.2a}$$

$$r_{th} = r_s \frac{X_M^2}{r_s^2 + X_s^2} \tag{5.2b}$$

$$X_{th} = X_M \frac{r_s^2 + X_s X_{ls}}{r_s^2 + X_s^2}. \tag{5.2c}$$

The change in speed resulting from adding external resistors can be analyzed by plotting the mechanical speed as a function of external resistance, for constant load torques. In (5.1), the electromagnetic torque is fixed at a constant value, and the mechanical speed is solved for different values of external resistance. Fig. 5.32 shows a plot of speed as a function of external resistance in the motor mode, while Fig. 5.33 shows the same plot but in the generator mode.

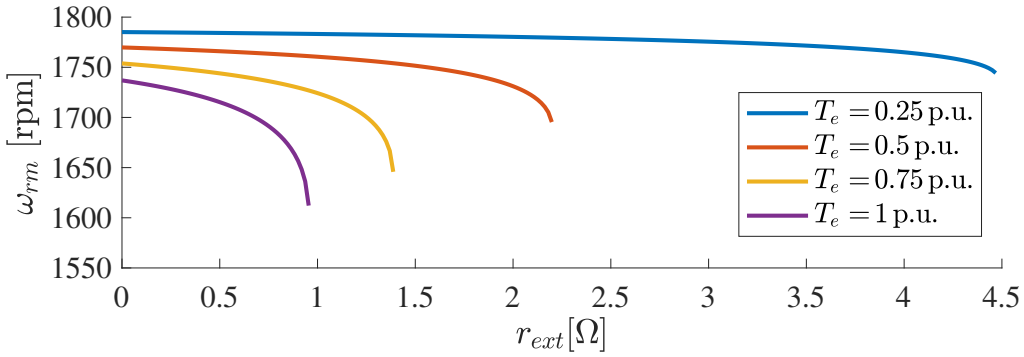

Figure 5.32: Speed as a function of external resistance for different fixed positive torque values.

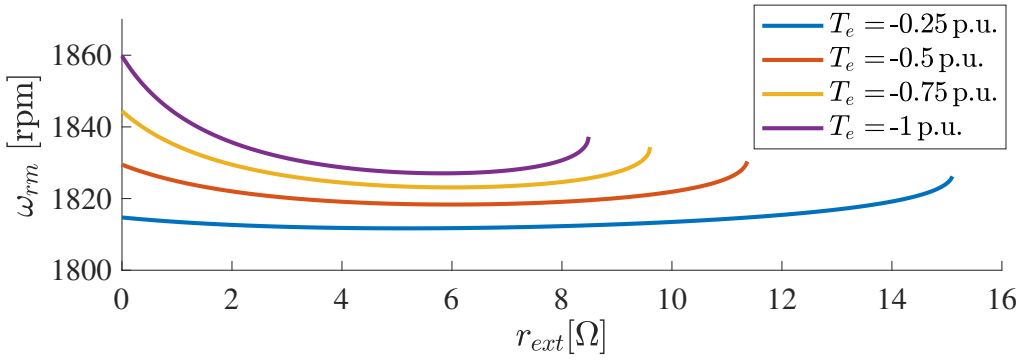

Figure 5.33: Speed as a function of external resistance for different fixed negative torque values.

As expected, in the motor mode, as the external resistance is increased, the speed always decreases. However, in the generator mode, the speed initially decreases before starting to increase. This indicates a reversed effect of the manipulated variable (in this case, the external resistance) in

the controlled variable (mechanical speed) within the initial region of normal operation. That effect can compromise the performance of the position synchronization control, giving rise to unstable operation.

Chapter 6

Hardware Validation

This chapter presents a testbed that was designed and constructed to support the development and validation of new architectures and control algorithms for aerospace electromechanical actuation system alternatives. This chapter also describes the system requirements, design detail, and initial experimental test results performed on the new aerospace actuation testbed.

6.1 Testbed Description

Some of the potential advantages of electromechanical drive alternatives are lighter weight, reduced maintenance, and enhanced system control and diagnostics [1–7]. However, the evaluation of electromechanical drive alternatives requires extensive research and hardware validation. Technical challenges to be addressed in future research and validation activities include: selection of electrical distribution architectures, appropriate choice of electrical machines and control strategies, minimization of space and weight, anomaly detection and mitigation, and achieving equal or better reliability and safety compared to existing drives.

As has been demonstrated by numerical simulations in Chapter 5, the conventional TRAS can be replaced by an electromechanical alternative (EM-TRAS) using a central-converter multi-machine drive architecture. Position synchronization was achieved through the proposed technique, and the control performance could be improved by applying optimal control design tools. To obtain hardware validation for this and other potential aerospace actuation solutions, a testbed was designed and constructed at Colorado State University. What follows is a description of the requirements, conceptual design, detailed design, and the results of initial hardware experiments using the testbed.

High-level system requirements for the testbed were defined as:

1. Emulate up to four parallel, mechanically coupled electromechanical actuation lines;

2. Allow flexibility for incorporating novel electrical motor/generator feedback control concepts;

3. Emulate mechanical failures and wear conditions such as jamming and corrosion;

4. Allow for fully-programmable and independently-controllable load profiles on each actuation line;

5. Include features for safe operation and avoidance of equipment damage;

6. Provide supervisory control and high-speed data acquisition for test automation, user input, and measurement logging.

Fig. 6.1 shows the conceptual design of the testbed to satisfy these requirements in functional block diagram form. It comprises three main subsystems: a motor control cabinet, test stand, and supervisory control and data acquisition (SCADA) system.

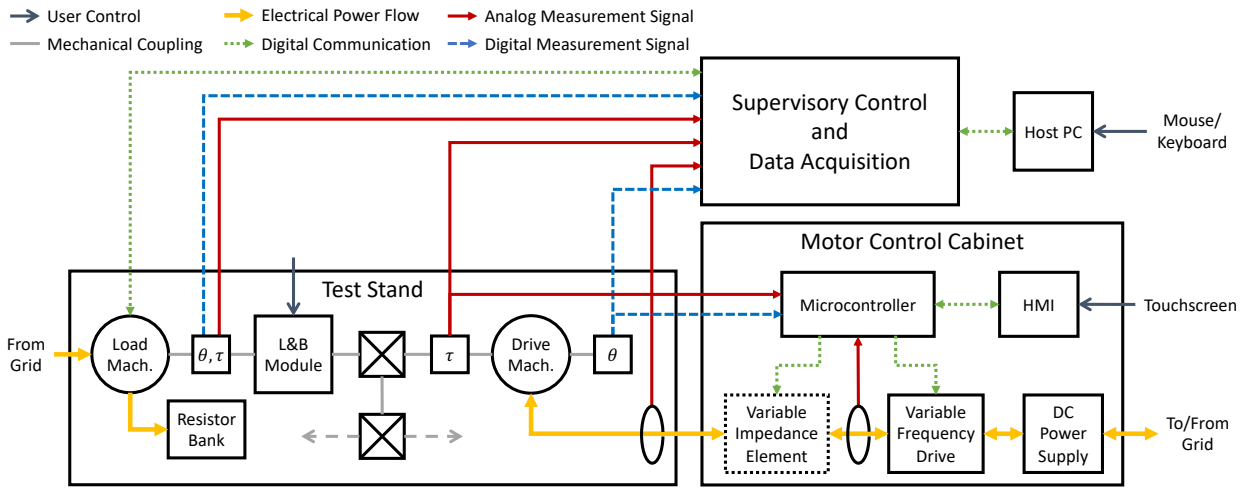

Figure 6.1: Block diagram of the testbed.

As shown in Fig. 6.1, the motor control cabinet comprises the power-electronic drive for the drive motor/generators, indicated by the variable frequency drive (VFD), switching-level feedback

control (microcontroller), converter human-machine interface (HMI), a variable impedance element (used in rotor position synchronization), DC supply, and sensors for measuring voltages and currents of each drive machine. The test stand includes four actuation lines that are mechanically coupled by one-to-one, three-way gearboxes. Each line comprises a drive machine, a load and braking module (L&B) that emulates mechanical anomalies such as jamming, friction, and side-load, a load machine that is responsible for emulating aerodynamic wind forces, a resistor bank, and several sensors for measuring torque (indicated by τ) and rotor position (indicated by θ). The SCADA serves as a test automation platform, stores high-speed measurement data, and provides an interface for user commands.

6.1.1 Motor Control Cabinet

The motor control cabinet houses the power-electronic drive for the drive motor/generators. The front panel of the motor control cabinet is shown in Fig. 6.2. The power-electronic drive includes power-electronic switches and a microcontroller for executing feedback control for the electrical machines. To achieve high-performance control of speed, position, and torque in the drive machines, the converter employs the three-phase fully-controllable bi-directional converter shown in Fig. 3.7.

Fig. 6.3 shows several components of the power-electronic drive. Each leg of the drive consists of Semikron SKM145GB066D IGBT module packs. The IGBTs are driven by Semikron gate drive boards that have protection, isolation, and conditioning features needed to provide the correct voltage levels for switch-

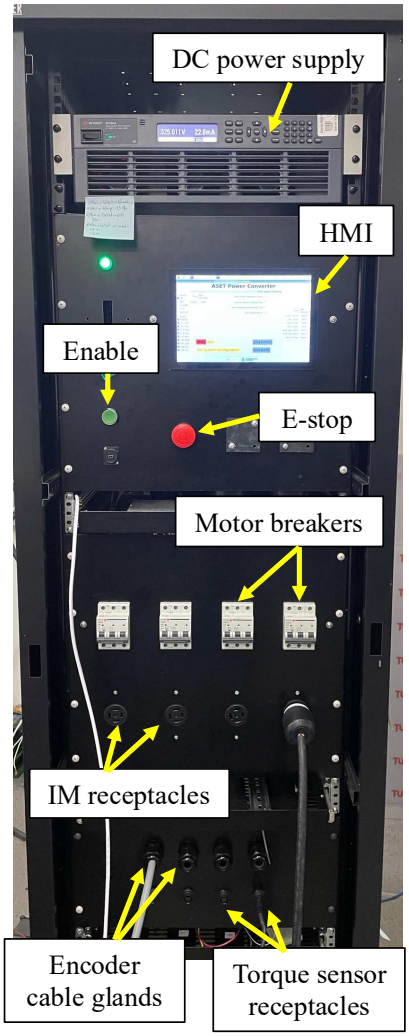

Figure 6.2: Front panel of the motor control cabinet.

ing on and off the IGBTs. The DC voltage is supplied by a Keysight RP7962A 10 kW, 500 V, ± 40 A DC regenerative power supply. The supply was selected to be regenerative (bi-directional) so that the drive machines could operate in motor or generator mode. The DC link capacitor is a 176 mF capacitor bank. Normally-open contactors were installed between the capacitor bank and the DC supply.

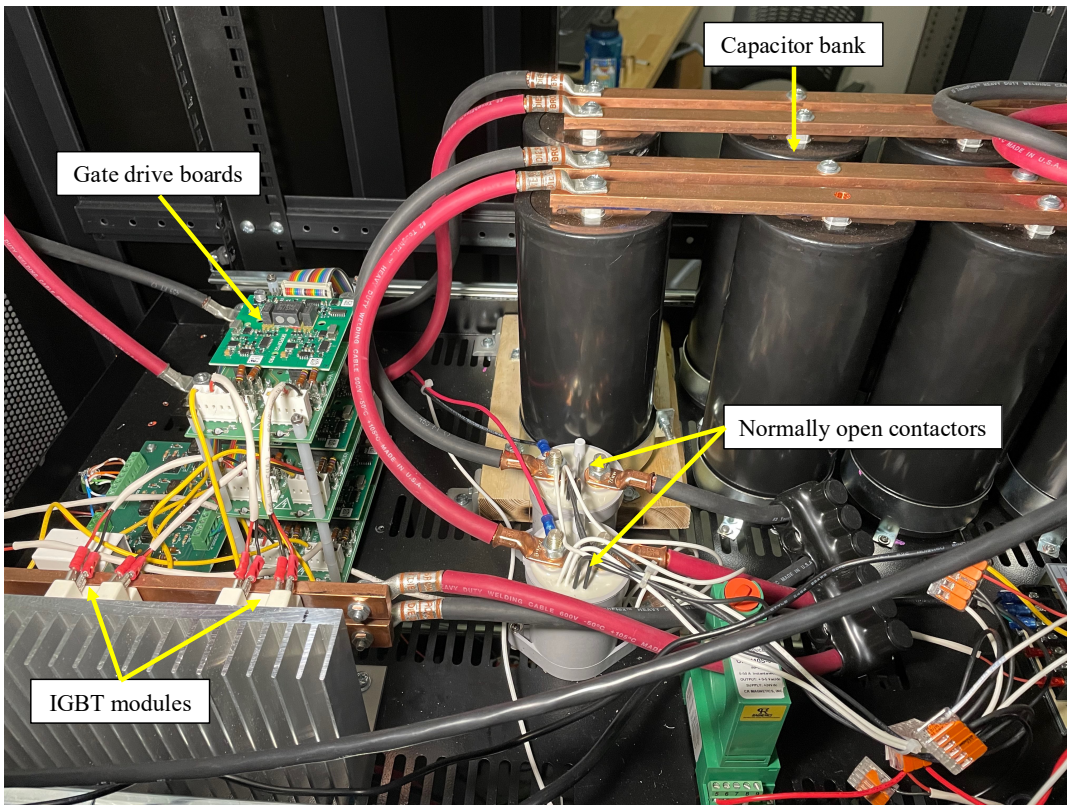

Figure 6.3: Power converter components.

Switching-level control of the drive is accomplished using a Texas Instruments microcontroller (or digital signal processor, DSP), model TMS320F28379D. It has a 200 MHz processor, 24 analog inputs, 12 PWM modules, 169 General-Purpose Input/Output pins, two dual-core processors, and several dedicated modules to implement, for example, encoder signal processing and serial communication. The DSP is responsible for sampling and processing measured signals, running the control algorithms, driving the switching signals for the power converter and the external resistor

circuit, and communicating with the HMI. The code is written in C through a Texas Instruments IDE called Code Composer Studio (CCS).

The converter HMI is programmed in Python and runs on a Raspberry Pi with a touchscreen display. Through the HMI, users can issue commands to the microcontroller, select operation modes, sets control parameters, and access system status. The HMI also displays voltages, currents, speeds, torques, and fault conditions. Fig. 6.4 shows a screenshot of the HMI. The communication protocol used is UART/SCI, an asynchronous serial protocol that allows bidirectional and simultaneous communication between the DSP and the HMI.

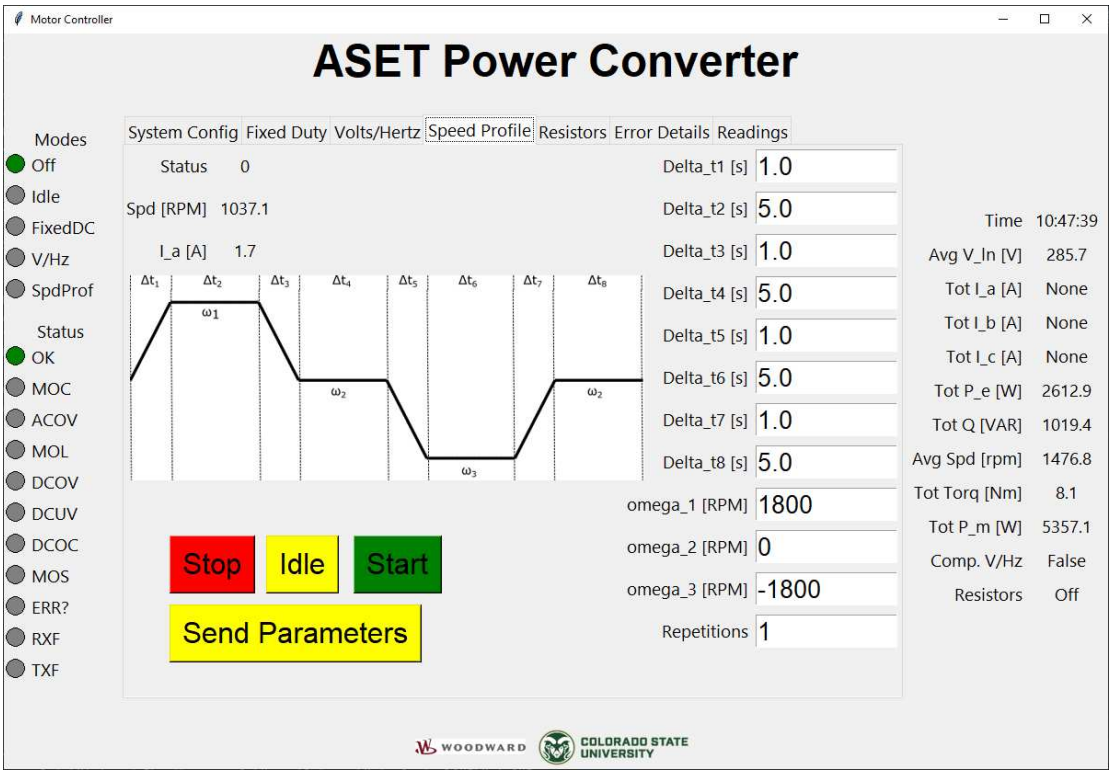

Figure 6.4: Screenshot of the HMI.

An additional feature of the motor control cabinet are circuits for providing variable stator resistances in-line with the drive machine stator windings. The variable resistance control circuit

shown in Fig. 4.3 was built to be used in the testbed. A picture of the implemented variable resistance circuit is shown in Fig. 6.5.

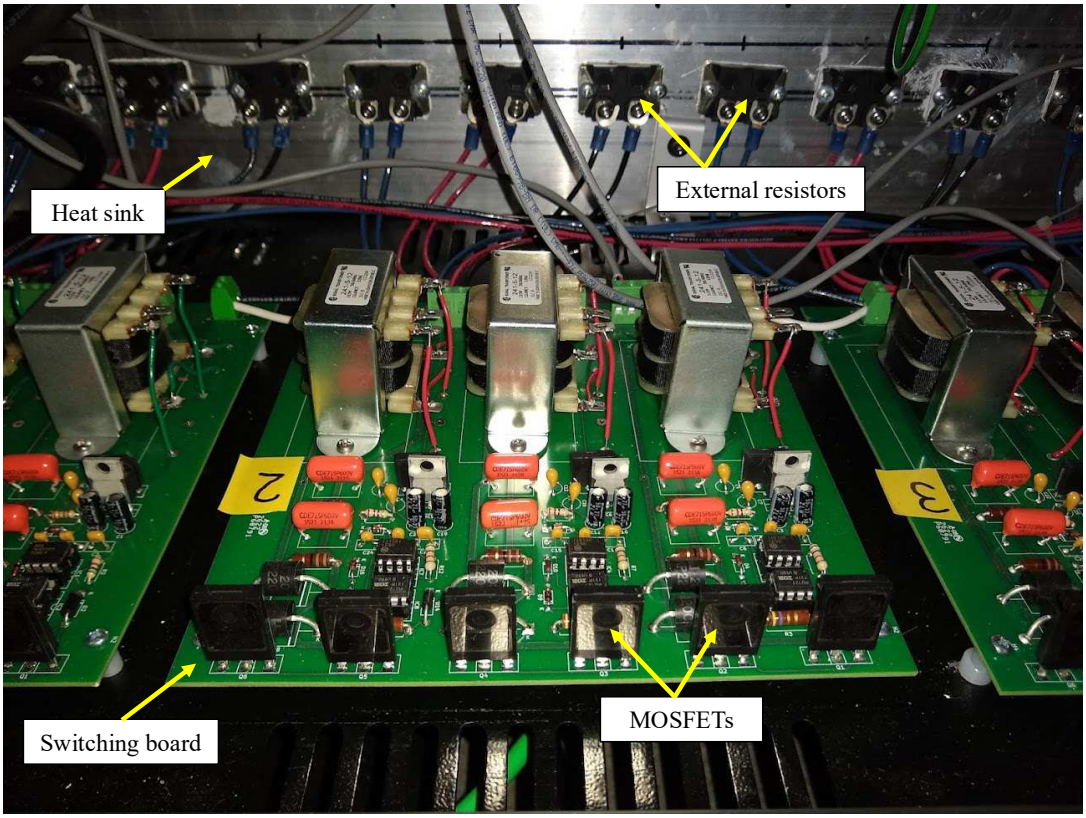

Figure 6.5: Variable resistance switching boards.

6.1.2 Test Stand

The test stand consists of four actuation lines that are mechanically coupled. Fig. 6.6 shows a picture of the physical test stand. Fig. 6.7 shows an illustration of two actuation lines depicting component interactions and sensors.

Each actuation line includes two three-way gearboxes, shown separately in Fig. 6.8a. These gearboxes have a one-to-one gear ratio; their function is to interconnect adjacent lines. This interconnection is done via flexible shafts, which emulate the inherent flexibility of the nacelle. The

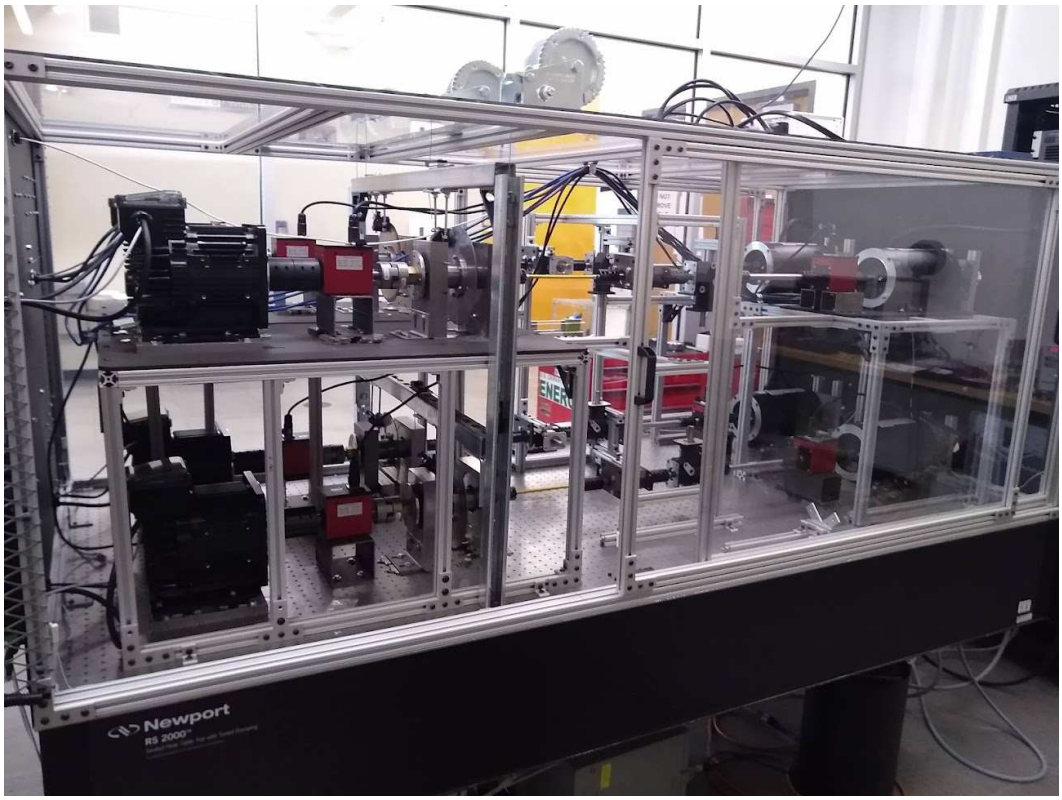

Figure 6.6: Test stand with four actuation lines.

testbed is configurable so that different levels of flexibility can be emulated. Lines can also all be disconnected easily by removing the shafts between the gearboxes.

A load and braking (L&B) module is present in each actuation line, located adjacent to the torque sensor on the load side. Fig. 6.8b shows an illustration of one L&B module. The purpose of the L&B module is to emulate mechanical inertia and friction — including anomalous conditions. Friction and jamming are emulated using a disc brake and braking pads. The friction level is adjusted by means of an external winch that controls the position of the braking pads with respect to the disc brake. A hex nut mounted in one of the casings is rotated to add a controlled misalignment to the actuation line, which also acts as a sideload. Finally, there is an inertia wheel with holes distributed along its surface, allowing bolts to be added in such a way as to create different types and levels of inertia imbalance to the actuation lines.

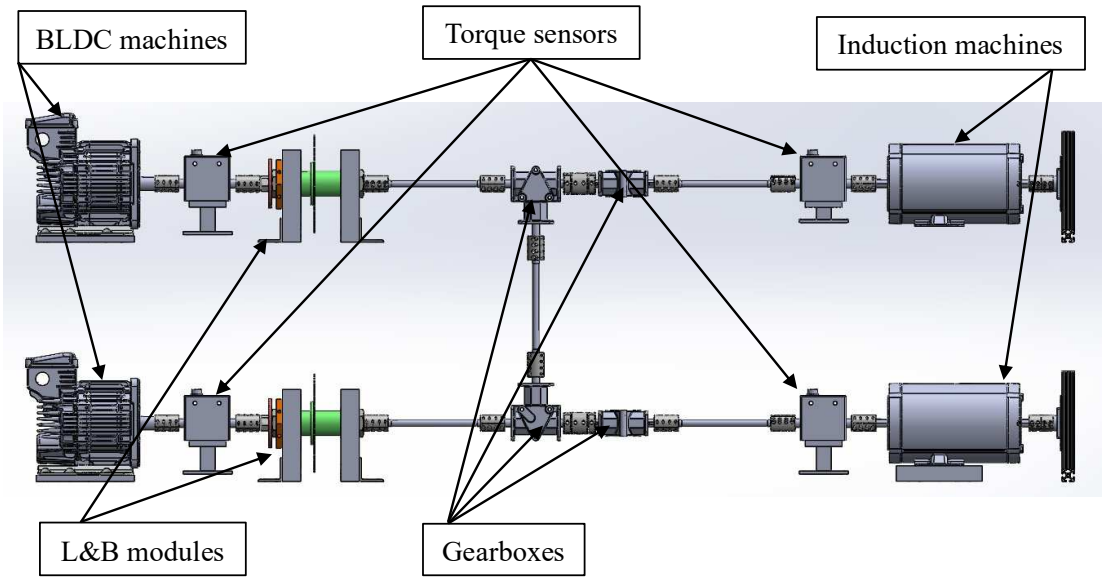

Figure 6.7: Illustration of two coupled actuation lines.

(a) **(b)**

Figure 6.8: (a) Gearbox and (b) load and braking (L&B) module.

The testbed can also emulate backlash using ground coupling keys in any rigid coupling, either restrained to an actuation line or in the interconnections between lines. Varying levels of backlash can be added by using different ground coupling keys.

Different types of electrical machines may be use as the drive motors/generators. In Fig. 6.1, squirrel-cage induction machines (IMs) serve as the drive motors/generators. Since the testbed is a scaled-down version of real aircraft actuation systems, commercial off-the-shelf low-power machines are used. The IMs in Fig. 6.1 are rated for 1 hp, 1725 rpm, with a rated torque of 4 Nm. For the 230 V connection used in the testbed, the rated current is 3.0 A.

Brushless direct-current (BLDC) machines function as the load machines. They are responsible for emulating variable aerodynamic forces (converted to rotational torques) on the actuation lines. A commercial ClearPath CPM-MCVC-D1001P-RLN model was selected for its integrated closed-loop control of position, speed, and torque. Digital input pins allow the torque to be controlled with high accuracy. The BLDCs used in the testbed are rated for 4 Nm continuous torque (and 14 Nm peak torque for short periods), 2820 rpm maximum speed, and 1.32 hp continuous power. A stepdown three-phase transformer is used to power the BLDCs at 230 V (line-line rms). For negative torque production in generator mode, dissipative external ("dump") resistors burn excess power. A set of three 250 W regenerative energy shunts is connected to each BLDC DC link for this purpose.

The testbed is equipped with sensors to measure mechanical variables (angular position and torque) and electrical variables (voltage and current). Each actuation line has two torque sensors measuring the torque at the shafts of the drive and load machines. The torque sensors provide an output voltage signal in the range of ± 5 V corresponding to a measured torque in the range of ± 20 Nm. The driving-side torque signals are measured by the DSP, while both sides are measured by the SCADA. The torque sensors also provide an incremental encoder digital output with 60 pulses per revolution, which is used by the SCADA to quantify differences in speed and position between the load side and driving side of each line. Connected to the other end of the shaft of each driving machine is a 14-bit absolute encoder, which provides a high-resolution position measurement to the DSP and the SCADA. Inside the motor drive cabinet are voltage and current sensors that measure the three-phase output voltage of the power-converter and two phases of the currents of all the driving machines (the third current is calculated by the DSP based on no-

neutral connection). Sensing boards are used to condition all of the sensors' output voltage signals to match the analog input range of the DSP (0 - 3.3 V) and to filter high-frequency components that could cause aliasing problems. Mounted on the test stand are voltage and current sensors that measure one phase of the line-to-line voltage and one phase of the current for each driving machine, feeding output voltage signals in the range of ± 10 V into the SCADA. An optocoupler circuit is used to condition the encoder digital outputs from the load side torque sensors for the SCADA.

6.1.3 Supervisory Control and Data Acquisition

Supervisory control and data acquisition is provided by a National Instruments PXI-1031 with PXI-8016 controller. These operations are achieved using a LabView program. One function of the SCADA program is used to command speed or torque profiles of the load machines, or automated torque control based on loaded position-indexed torque profiles. Another function generates plots and provides data logging for voltage, current, torque, and speed measurements. The PXI unit contains a PXI-6259 analog input module for voltage, current, and torque inputs, a PXI-6509 digital I/O module for control of the load motors, and a PXI-7833R FPGA module with digital inputs for speed and position measurement along with generation of PWM signals for the digital output module.

6.1.4 Safety Features

The testbed also includes several safety features to protect both the user and equipment. The DSP implements an error handling feature that shuts down the system when any measured variable goes above a user-defined threshold. For AC variables, such as voltages and currents, rms values are used, while for slowly varying signals, such as speed and torque, a fast average is calculated. When the DSP detects an error condition, it triggers an error flag and opens the normally-open contactors between the DC power supply and the power-converter, as well as the contactors that energize the BLDCs. Simultaneously, the DSP records a log of the system variables and sends it to the HMI. The test stand also includes an emergency stop (E-stop) button located on the front panel

of the cabinet. When pressed, it opens the same contactors that the DSP opens. Door switches installed on all doors of the test stand are also connected to the aforementioned contactors, opening them in the event of any door being opened.

6.2 Experimental Tests

This section describes several case studies performed using the testbed, to both illustrate the operation of the testbed and to demonstrate the rotor position synchronization method proposed in Chapter 4.

6.2.1 Case Study I – TRAS profile with CVHz

These measurements were taken during emulated EM-TRAS cycles. During a typical EM-TRAS operation, there is a "deploy" cycle followed by a "stow" cycle. Over a deploy cycle, the actuators must accelerate, keep a constant speed, and then decelerate to a complete stop. This results in a smooth and direct position displacement. The stow cycle consists of the reverse operation of the deploy cycle, where the actuators rotate in the opposite direction in order to retract the actuation elements back to the original resting position. Fig. 6.9a shows speed and position for a full deploy-stow cycle, where the dotted red line separates the two individual cycles.

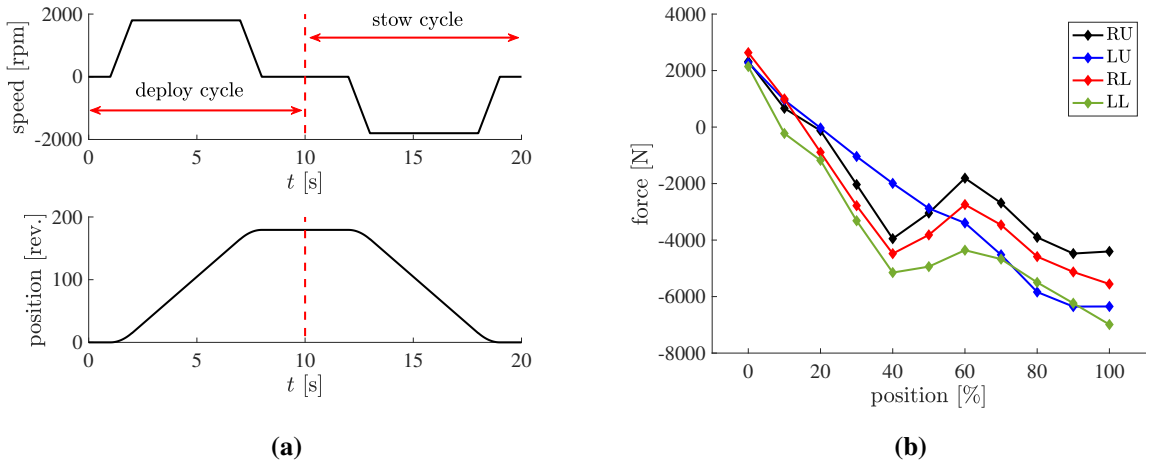

(a) **(b)**

Figure 6.9: TRAS typical characteristics: (a) Force profile and (b) speed and position profiles.

A TRAS deploy and stow cycle is also characterized by a load profile. As the actuation elements move, aerodynamic forces are distributed among them. Fig. 6.9b shows a typical force vs. position deploy profile, for the case where the TRAS comprises four actuation lines. At the beginning of the cycle, the forces are positive because the actuators must overcome the initial wind forces when deploying the actuator arms. After the actuator arms are retracted, wind forces act to further open the actuator arms, resulting in negative applied forces.

For this experiment, the drive machines were driven using the "speed profile" mode in the HMI. This mode allows the user to set a custom speed profile that emulates a typical full deploy and stow cycle. The power converter was set to use Compensated Volts-per-Hertz speed control. Motor 1 was arbitrarily selected to be the primary. The SCADA was used to command each BLDC to produce a load torque based on their individual position, following scaled-down real TRAS load profiles. For the deploy cycle, the load profile shown in Fig. 6.9b was used. The actuators identified as RU, LU, RL, and LL were assigned to the actuation lines one, two, three, and four, respectively. The speed profile shown in Fig. 6.9a was commanded. The actuation lines were not mechanically connected together, the L&B module was not used to add any anomalies, no backlash was included, and only rigid shafts were used. The electronic position synchronization function was not used. Measured torque, speed, position, voltages, and currents for each line were recorded by the SCADA for the whole cycle.

Fig. 6.10 shows the torque, measured by the IM torque sensors, of all the actuation lines during the full cycle. Note the unbalanced load on a typical deploy/stow cycle, which corroborates the need for a position synchronization feature. The load torque applied to motor 4 has the highest negative value at the end of the stow cycle, just before the machines decelerate, while motor 1 experiences the lowest negative load torque. This aligns with the force vs. position profile shown in Fig. 6.9b and the fact that motor 1 and motor 4 correspond to the actuators RU and LL, respectively.

Fig. 6.11 shows the speeds for all actuation lines and the commanded speed during the full cycle; Fig. 6.12 provides a zoomed-in view of the responses right before the machines start to decelerate. They all follow the speed profile commanded by the HMI, with some expected speed

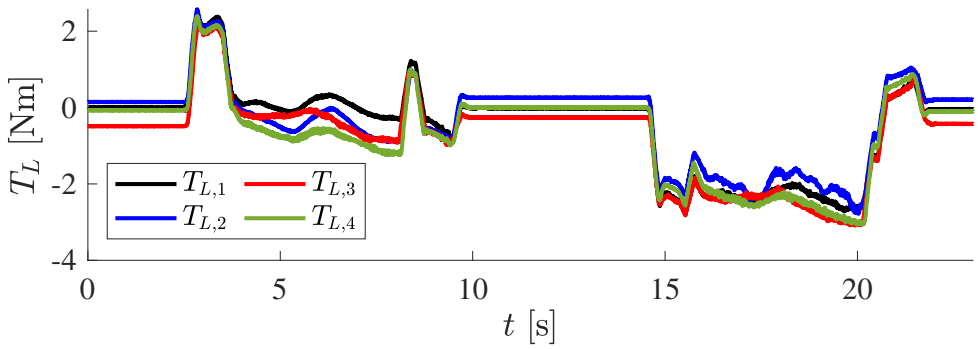

Figure 6.10: Torque measured by the IM torque sensors during a full deploy/stow cycle; CVHz.

error. Even motor 1, which is the primary, presented a persistent speed deviation from the commanded speed. The CVHz, which is used in this test, does not provide a closed-loop speed control, hence the non-zero speed error. Note, however, the different steady-state speeds of the four IMs. Under an unbalanced load torque condition, which corresponds to this experimental test, speed and position synchronization is not achieved, unless a synchronization method is used, such as the one proposed by this work.

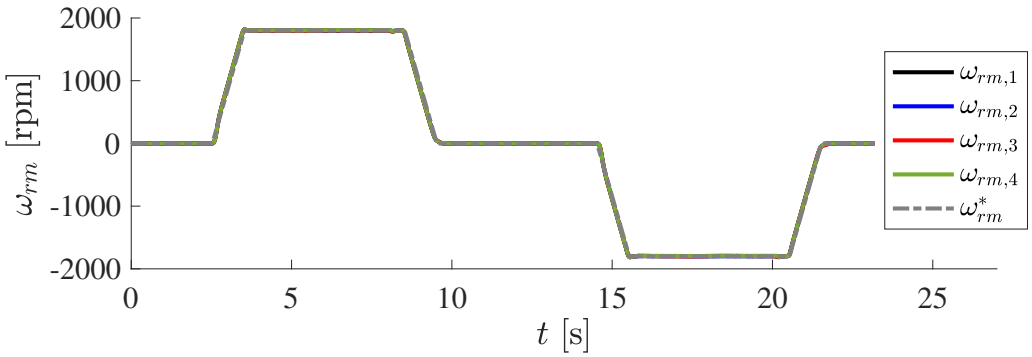

Figure 6.11: Rotor mechanical speed and commanded speed of the four induction machines during a full deploy/stow cycle; CVHz.

Fig. 6.13 shows the position of all the actuation lines during the full cycle. Fig. 6.14 provides a zoomed-in view at the end of the deploy cycle. Due to the differences in load torques, the final

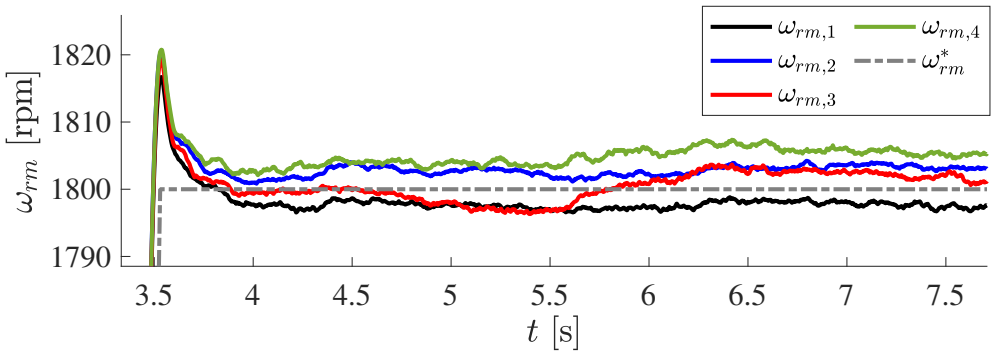

Figure 6.12: Rotor mechanical speed and commanded speed of the four induction machines (zoomed-in) during a full deploy/stow cycle; CVHz.

position is not the same for the actuation lines. Motor 4 has the largest final position, which is consistent with the higher negative load torque it experiences at the end of the deploy cycle.

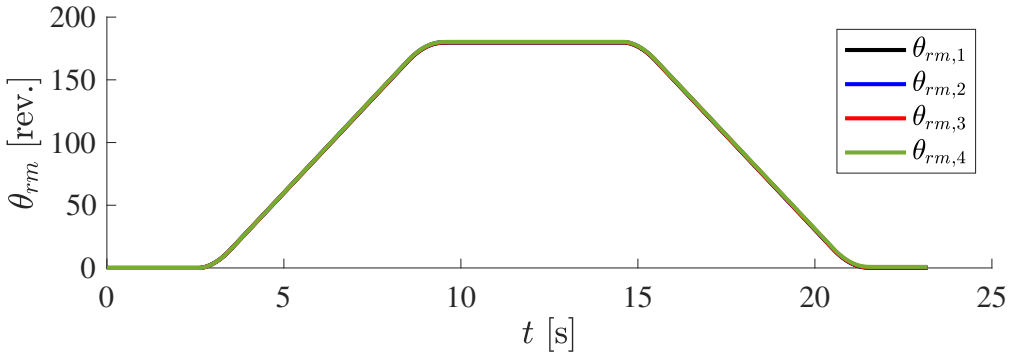

Figure 6.13: Rotor mechanical position of the four induction machines during a full deploy/stow cycle; CVHz.

Fig. 6.15 shows the voltage between the a and b electrical phases during the acceleration time of the deploy cycle. Fig. 6.16 shows the a-phase current of the first IM for the same period. The frequency of the electrical signals ramps up from zero to 60 Hz, which is responsible for speeding up the IMs smoothly during this time.

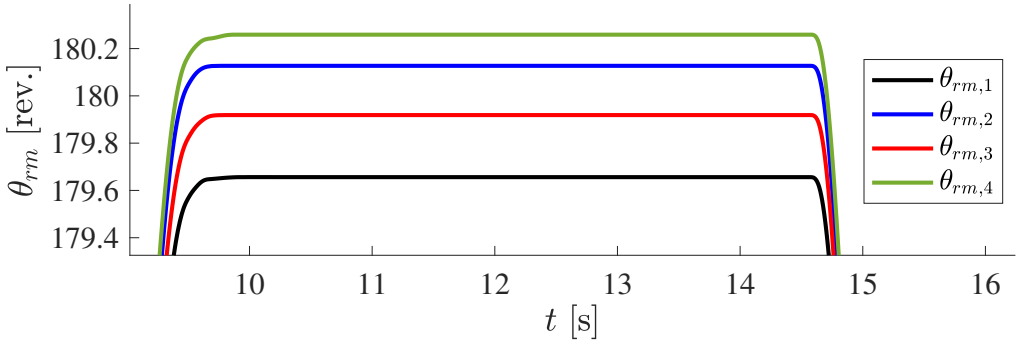

Figure 6.14: Rotor mechanical position of the four induction machines (zoomed-in) during a full deploy/stow cycle; CVHz.

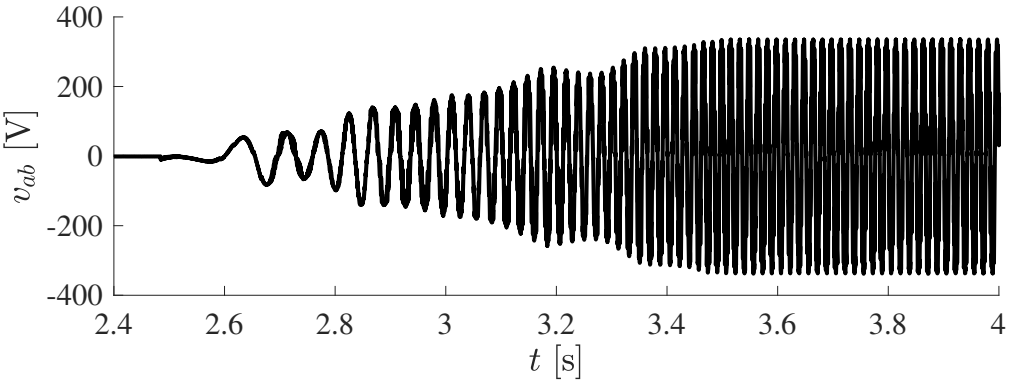

Figure 6.15: Voltage between phases a and b of the first IM during the beginning of the deploy cycle; CVHz.

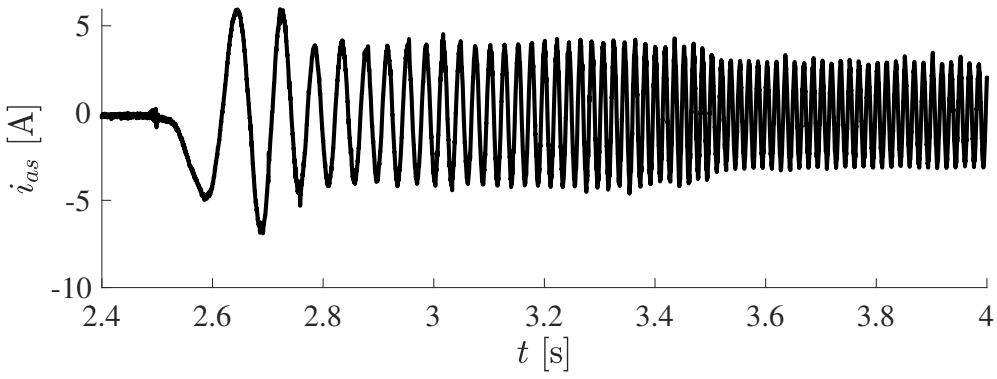

Figure 6.16: Phase a stator current for the first IM during the beginning of the deploy cycle; CVHz.

6.2.2 Case Study II – TRAS profile with IDFOC

This case study is identical to the previous one, with the exception that the central converter uses the IDFOC to control the primary motor. As described in Section 3.1.3, the IDFOC consists of a closed-loop speed control acting alongside a high-performance electromagnetic torque control. In that way, it is expected to see the speed of the primary machine to closely follow the commanded speed.

Fig. 6.17 shows the torque, measured by the IM torque sensors, of all the actuation lines during the full cycle. The response is quite similar to the one observed in the previous case study, since the torque control of the BLDC machines remained the same.

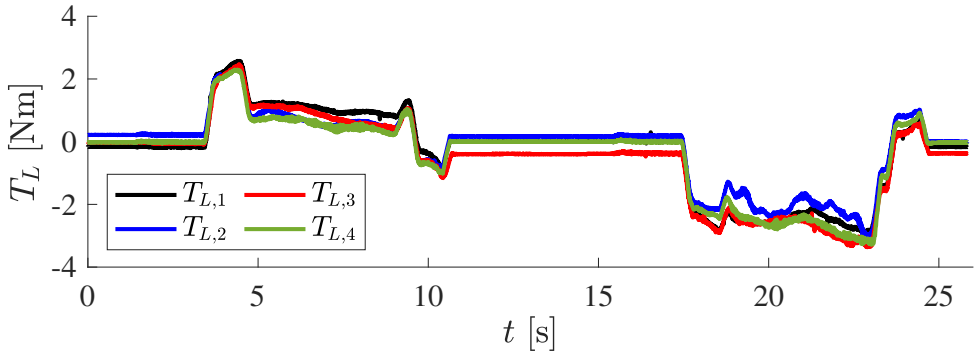

Figure 6.17: Torque measured by the IM torque sensors during a full deploy/stow cycle; IDFOC.

Fig. 6.18 shows two zoomed-in views of the machines' speed responses with the commanded speed. The speed of machine 1 (black solid line) matches the commanded speed during steady-state, and has an underdamped response during the transients (notice the overshoot in Fig. 6.18a). Since there is no position synchronization control applied in this case study, the other machines' speeds will deviate from the primary due to the unbalanced load torque distribution. Notice how machine 3's speed response is close to machine 1. This is explained by the load torque distribution depicted in Fig. 6.9b. The black and red curves have a close proximity, resulting in less speed deviation between these two machines.

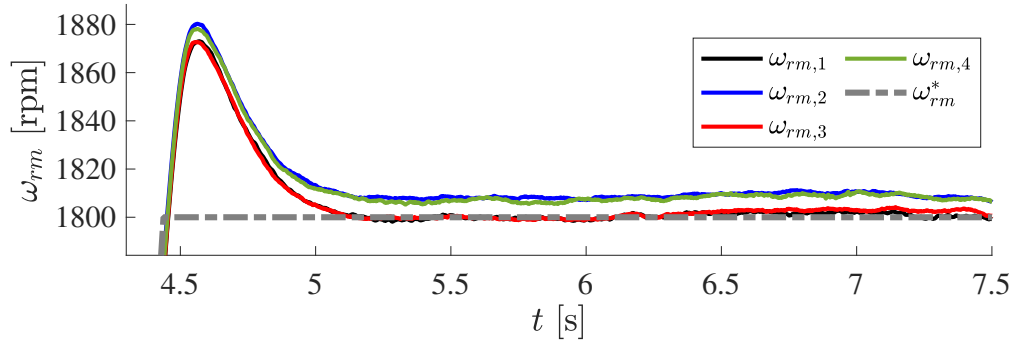

(a)

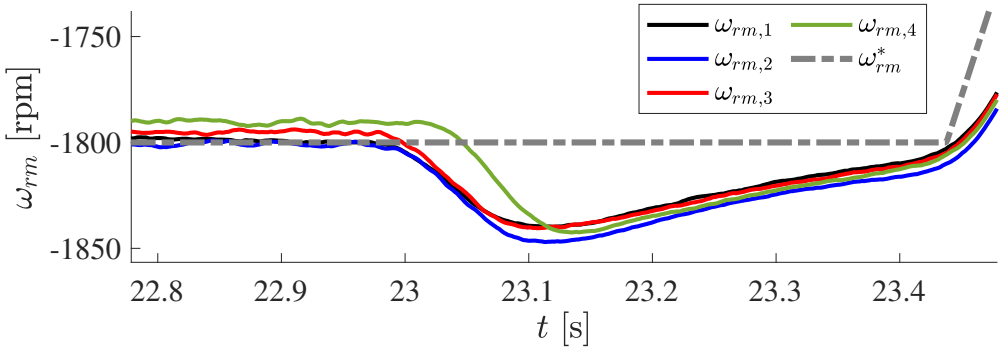

(b)

Figure 6.18: Rotor mechanical speed and commanded speed of the four induction machines (zoomed-in) during a full deploy/stow cycle; IDFOC: (a) deploy and (b) stow regions.

Fig. 6.19 shows the voltage between the a and b electrical phases during the acceleration time of the stow cycle. Fig. 6.20 shows the a-phase current of the first IM for the same period. These two electrical variables resemble their corresponding versions of the previous case. However, in this case study, they present a choppier behavior, a direct effect of the modulation technique used in the IDFOC, which is the hysteresis current-band control.

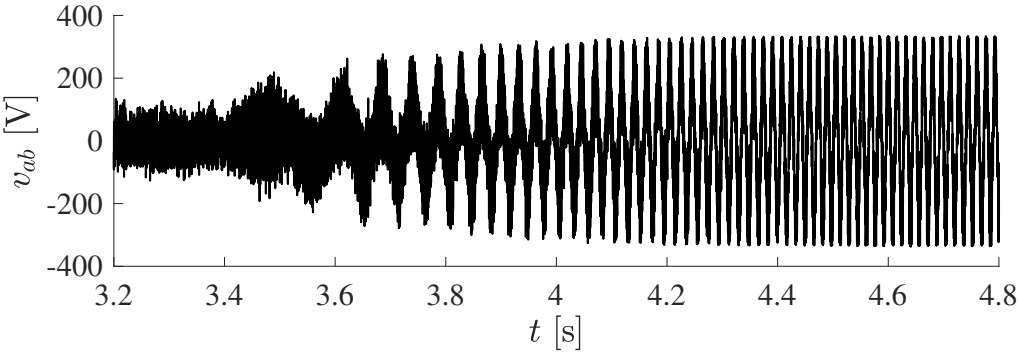

Figure 6.19: Voltage between phases a and b of the first IM during the beginning of the stow cycle; IDFOC.

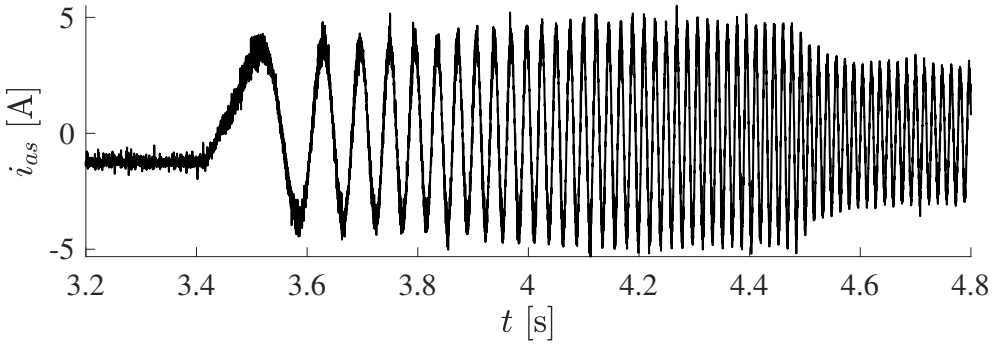

Figure 6.20: Phase a stator current for the first IM during the beginning of the stow cycle; IDFOC.

6.2.3 Case Study III – Position Synchronization, Uneven and Constant Load Torques

In the next two case studies, experiments were performed to validate the position synchronization control proposed in Section 4.1 under the following conditions. The four actuation lines of the testbed were used, with the variable impedance element connected to all of them. The central converter was set for CVHz speed control with a commanded speed of $\omega_{rm}^{*} = 1800\,\text{rpm}$. The primary machine, which is the one utilized by the CVHz for the feedback signals, was assigned dynamically as described in Section 5.1.4.

In this case study, the commanded speed of $\omega_{rm}^{*} = 1800\,\text{rpm}$ was first applied with zero torque load applied to each motor. After reaching steady-state, rated torque ($4\,\text{Nm}$) was applied to all the

actuation lines. Finally, after steady-state operation, torque loads of $T_{L,1} = 4\,\text{Nm}$, $T_{L,2} = 3\,\text{Nm}$, $T_{L,3} = 2\,\text{Nm}$, and $T_{L,4} = 1\,\text{Nm}$ were then applied. Transient responses are shown in Figs. 6.21-6.25.

Fig. 6.21 shows the load torque as measured by the IM torque sensor, for all the actuation lines. As shown, the load torques for each actuation line followed the commanded values defined by the load distribution for this case study, starting at approximately 2 s. The second actuation line presented some torque ripple, which the authors attribute to some mechanical misalignment present in that line. Given that the first actuation line has the highest load torque in this case study, its IM will be assigned as the primary motor by the control algorithm.

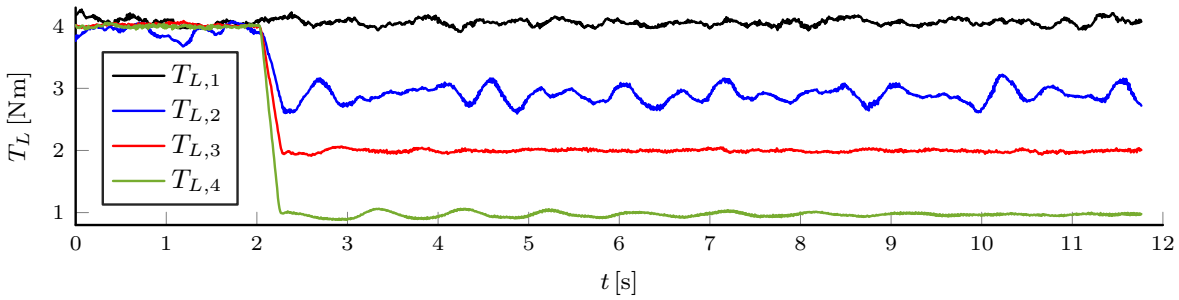

Figure 6.21: Load torque response; constant equally spaced load torques.

Fig. 6.22 shows mechanical rotor speed for all motors while Fig. 6.23 provides a zoomed-in view of the response after the unequal torque loads are applied. As shown in the results, the speeds of all the secondary motors converged to the first motor speed after some transient. Since the load torque of the first motor did not change, its speed remained constant. Line 2 took approximately 0.5 s to achieve speed convergency, while lines 3 and 4 took 1 s and 8 s, respectively. The higher the load torque difference between each secondary motor with respect to the primary motor, the longer the transient response and the speed peak deviation. This is attributed to the bigger external resistance needed to achieve position synchronization, resulting in a higher control effort demanded from the control elements. All IM rotor speeds reach approximately 1794 rpm after

reaching steady-state; the small steady-state speed error (0.3%) with respect to the commanded speed (1800 rpm) is a result of the open-loop speed control used in this study.

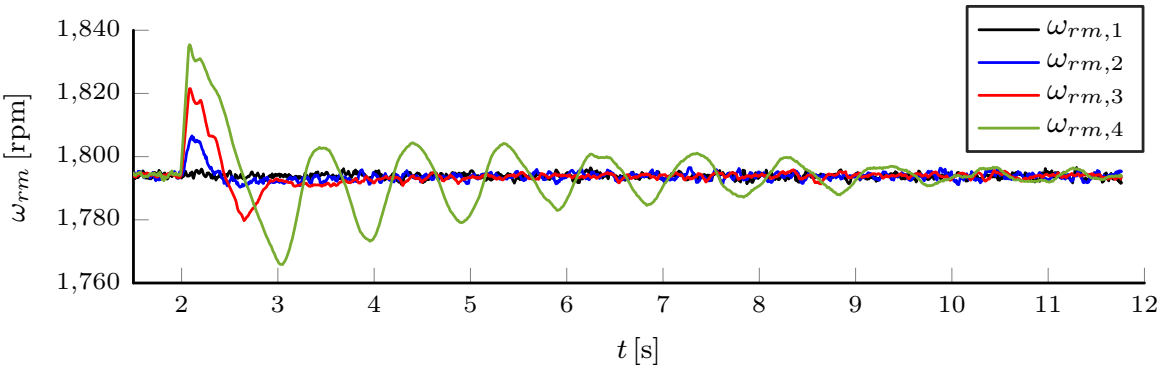

Figure 6.22: Mechanical rotor velocities; constant equally spaced load torques.

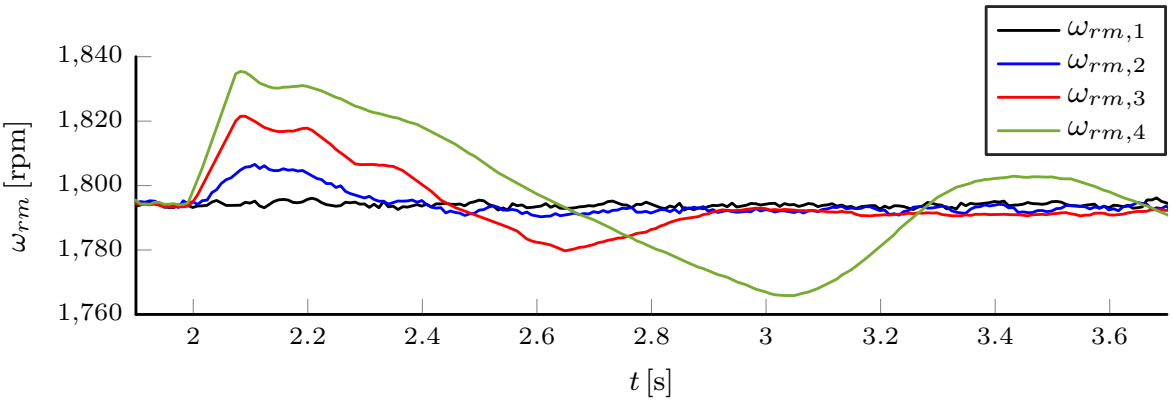

Figure 6.23: Mechanical rotor velocities (zoomed-in); constant equally spaced load torques.

Individual rotor angle differences for the secondary motors, referenced from the primary motor, are shown in Fig. 6.24. Just after $t = 2\,\text{s}$, synchronization errors are initially observed, before being resolved by the proposed control scheme. Similarly to what was observed for the speed responses, the position error also shows a larger transient time and peak value as the load torque difference increases. In this study, the maximum angle differences were $15.8°$, $42.2°$, and $92.3°$ for motors 2, 3, and 4, respectively. The results observed in the experimental studies agree with

those presented using numerical simulations (c.f. Section 5.1.1), demonstrating the ability of the position synchronization method to work under these conditions.

Fig. 6.25 shows the normed angle error; the normed error was observed to reach a peak value of 100° after the unbalanced load torques are applied. It can be seen that line 4 is the one that contributes the most to the high peak error and the longer settling time (approximately 10 s for the error to converge to less than 0.5°.)

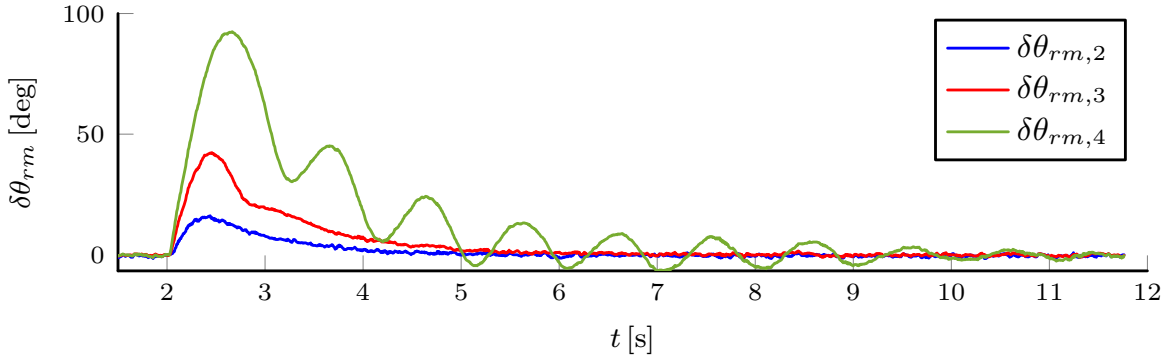

Figure 6.24: Individual angle differences; constant equally spaced load torques.

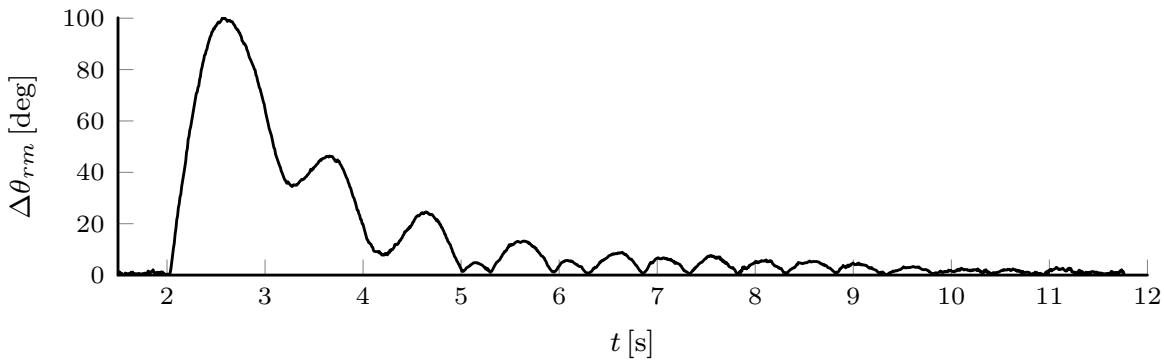

Figure 6.25: Normed angle difference; constant equally spaced load torques.

6.2.4 Case Study IV – Position Synchronization, Dynamic Load Torque Distribution

In this study, the initial conditions correspond to the steady-state operation of the previous case study, *i.e.*, commanded speed of 1800 rpm and the load torque distribution of $T_{L,1} = 4\,\text{Nm}$, $T_{L,2} = 3\,\text{Nm}$, $T_{L,3} = 2\,\text{Nm}$, and $T_{L,4} = 1\,\text{Nm}$. At approximately 2 s, a new load torque distribution was applied: $T_{L,1} = 1\,\text{Nm}$, $T_{L,2} = 4\,\text{Nm}$, $T_{L,3} = 2\,\text{Nm}$, and $T_{L,4} = 2\,\text{Nm}$. The goal was to verify the ability of the control algorithm to dynamically reassign the primary and secondary motors. Before the change in the load torques, the primary motor corresponds to line 1, while, after the change, the second motor has to be reassigned as the primary, since it is the highest loaded one. Furthermore, the main converter control strategy has to switch its controlled motor from line 1 to line 2. The motors' responses are shown in Figs. 6.26-6.29.

Fig. 6.26 shows the load torque as measured by the IM torque sensor, for all the actuation lines. As shown, the load torques followed the commanded values defined by the load distribution for this case study. Again, a small torque ripple was observed in line 2, due to some mechanical misalignments.

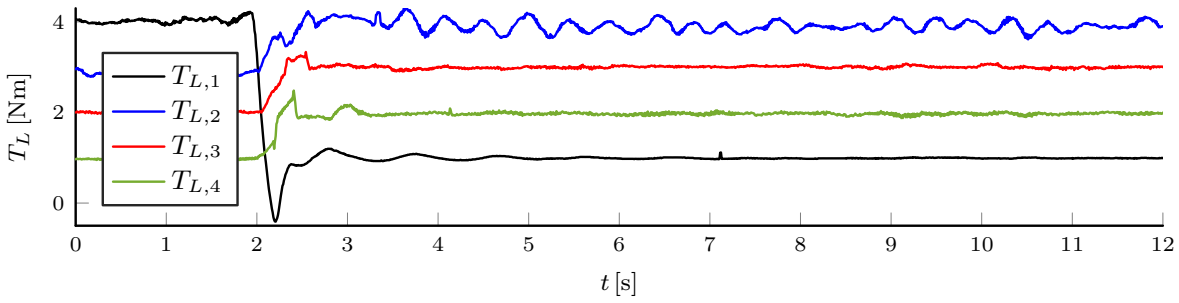

Figure 6.26: Load torque response; dynamic load torque distribution.

Fig. 6.27 shows mechanical rotor speed for all motors. Since the load torques of all the lines changed instantaneously, all the speeds presented some transient response. Motor 1 speed initially increased, while the other speeds dropped. The load torque change corroborates this behavior since line 1 was the only one subject to a decrease in its load torque, while all the other lines experienced

a load torque increase. However, the control strategy was able to drive all the speeds back to approximately 1794 rpm. Again, a longer transient time was observed for the line with the highest load torque difference from the primary motor, in this case, line 1.

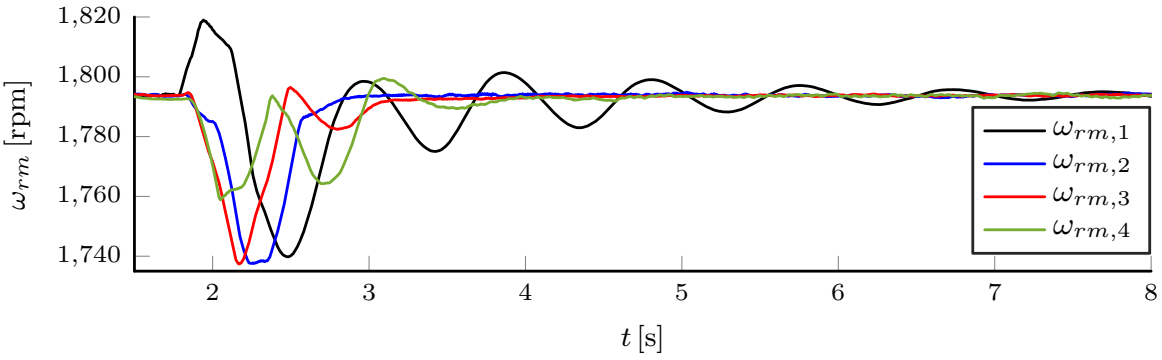

Figure 6.27: Mechanical rotor velocities; dynamic load torque distribution.

Individual rotor angle differences for the secondary motors, referenced from the primary motor, are shown in Fig. 6.28. In this study, the maximum angle differences were $124°$, $-35.5°$, and $63.5°$ for motors 1, 3, and 4, respectively. The initial negative position difference observed for lines 3 and 4 is attributed to the hysteresis delay of the primary/secondary dynamic control assignment. Only after motor 1 presented a positive angle difference of $60°$ with respect to motor 2, did the control algorithm assign motor 2 as the new primary. Also because of the hysteresis delay the peak errors showed higher values compared to the previous case study. Again, the experimental results are in agreement with the simulation results shown in Section 5.1.4.

Fig. 6.29 shows the normed angle error, that presented a peak value of $138°$. Again, one of the lines contributed more to the peak value, this time, line 1. The convergency time was approximately 10 s.

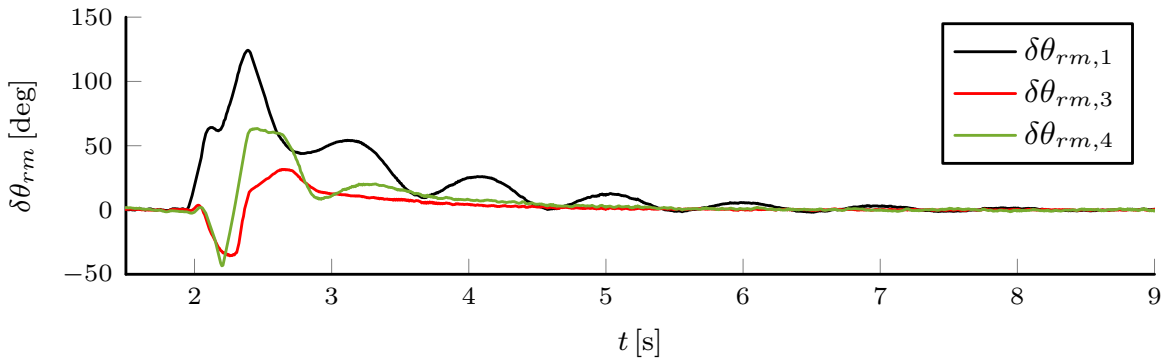

Figure 6.28: Individual angle differences; dynamic load torque distribution.

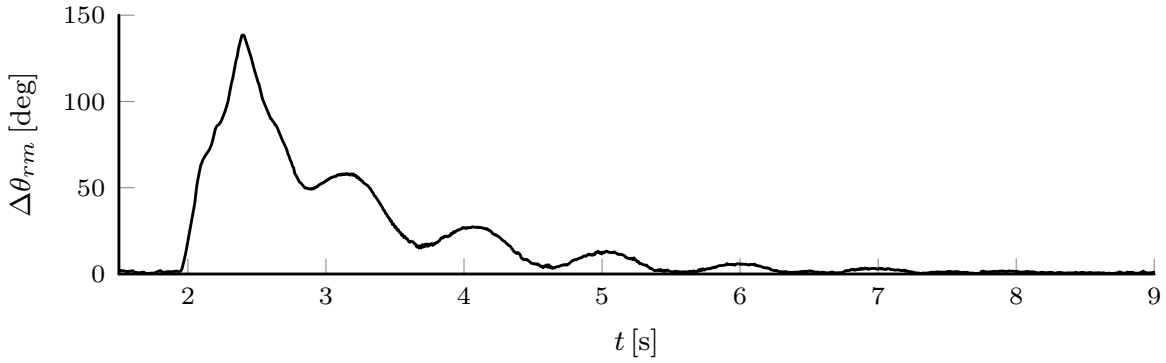

s

Figure 6.29: Normed angle difference; dynamic load torque distribution.

Chapter 7

An Alternative Position Synchronization Method – Voltage-Boost

This chapter describes an alternative position synchronization method, referred to herein as the "voltage-boost" method. It also presents different case studies performed through numerical simulations to demonstrate the method's functionality under different scenarios.

A note on notation. All the electrical subsystems depicted in this chapter are considered to have three electrical phases. Therefore, the electrical variables used to describe those subsystems (e.g., voltages and currents) are assumed to be a set of three-phase variables. Those variables will be noted as lower-case bold letters as in: $\mathbf{f} := [f_a \quad f_b \quad f_c]^T$, where f can be a voltage, v, or a current, i. Also, the voltages with no polarity indication correspond to the potential difference between the point where they appear and a virtual neutral of the machines.

7.1 A Novel Position Synchronization Method: Voltage-boost

Consider the Central Converter Multi-Machine (CCMM) topology shown in Fig. 7.1. Without loss of generality, the particular case of two induction machines is presented. The central converter output voltage, $\mathbf{v}_{\text{cc}}$, is applied to both machines. However, due to the potential different load torques, $T_{L,1}$ and $T_{L,2}$, and the necessity of achieving position synchronization, there is a mismatch between the number of manipulated variables (just one in this case, $\mathbf{v}_{\text{cc}}$) and the number of controlled variables (two in this case, $\theta_{rm,1}$ and $\theta_{rm,2}$). In the Distributed Converter Multi-Machine (DCMM) configuration shown in Fig. 1.2a, the solution for the problem is trivial because there are two independent variables being manipulated: the output voltages of the converters 1 and 2. In the CCMM topology, if it were possible to independently control the terminal voltages of each of the machines, the problem would correspond to that of the DCMM configuration.

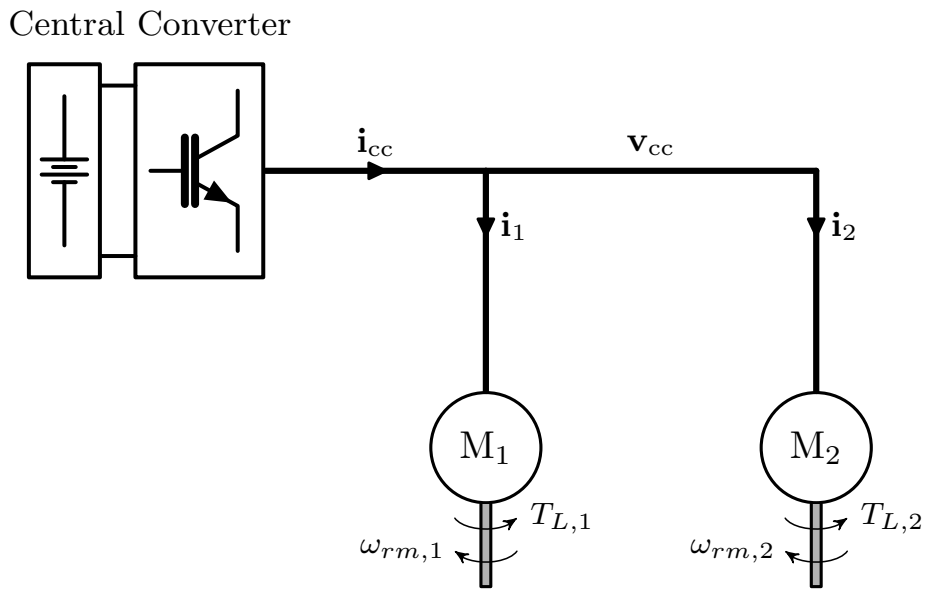

Figure 7.1: Central converter, multi-machine topology with two machines.

The method proposed in Section 4.1 is based on an independent variation of the in-line impedance of each machine by means of a variable three-phase resistance. To achieve a continuous resistance variation, power-electronics switches are connected in parallel with each fixed resistor, and the fast-average value of the in-line resistance is a function of the duty-cycle applied to the switches. For this proposed solution, the main line that powers each machine has to be opened and the circuitry has to be inserted in series. The electrical currents of the machines flow through the external resistors and the switches are directly switching on and off those same currents. There is a high power dissipation in the external resistors, and the switches have to be rated for the rated current of the machines. Moreover, since it is impossible to achieve a negative resistance using only passive elements, all of the machines connected to the central converter have to have the external variable resistance device connected, for the primary/secondary assignment is not necessarily known beforehand.

An alternative method to achieve position synchronization in a CCMM configuration is an independent and non-invasive machine terminal voltage control. Referring to Fig. 7.1, the central converter output voltage $\mathbf{v}_{cc}$ corresponds to the "bulk" of the necessary voltage that has to be

applied to the motors so that their "bulk" speed is controlled. In case their load torques are the same, $T_{L,1} = T_{L,2}$, their rotor speed and angular position will be the same, resulting in a natural position synchronization. As the load torques start to deviate from each other, the speeds (and hence the angular position) also start to deviate, requiring a correction, for example, in the terminal voltage applied to the motors. It can be shown that, in steady-state, the terminal voltage magnitude difference between the two motors is a function of the load torque differences. In fact, if the load torque difference is relatively small, the terminal voltage difference will be only a fraction of the "bulk" voltage $\mathbf{v}_{\text{cc}}$. Therefore, a device that could provide a small extra voltage independently controlled would solve the problem.

To achieve this, a set of an auxiliary converter and a three-phase compact transformer is proposed. The auxiliary converter is connected to the primary of the transformer, and the secondary corresponds to the main cables powering the machines. This configuration resembles a current transducer, used to measure partial discharges on power cables [50] or high-level currents in substations [51], for example. Fig. 7.2 from [50] illustrates such a device. The main current $i_1(t)$ corresponds to one phase of the machine (the primary of the transformer), while $i_2(t)$ would correspond to the current supplied by one phase of the auxiliary converter. The load R_L depicted in the Figure would correspond, instead, to one of the phases of the auxiliary converter.

However, in the position synchronization problem, the goal is to apply induced voltages in series with each machine. Those independently controlled induced voltages would add up to the central converter voltage $\mathbf{v}_{\text{cc}}$, resulting in different terminal voltages for each machine. This solution is presented in Fig. 7.3. The central converter output voltage is $\mathbf{v}_{\text{cc}}$, the in-line induced voltages for machines 1 and 2 are $\mathbf{v}_{\text{i,1}}$, and $\mathbf{v}_{\text{i,2}}$, respectively, and the terminal voltages applied to machines 1 and 2 are $\mathbf{v}_1 = \mathbf{v}_{\text{cc}} + \mathbf{v}_{\text{i,1}}$ and $\mathbf{v}_2 = \mathbf{v}_{\text{cc}} + \mathbf{v}_{\text{i,2}}$, respectively.

Each auxiliary converter can be controlled independently to produce whatever necessary voltage in the primary, which is (roughly) proportional to the induced voltages in each of the machine's lines. To illustrate the concept of the method, let us consider the steady-state torque vs. speed func-

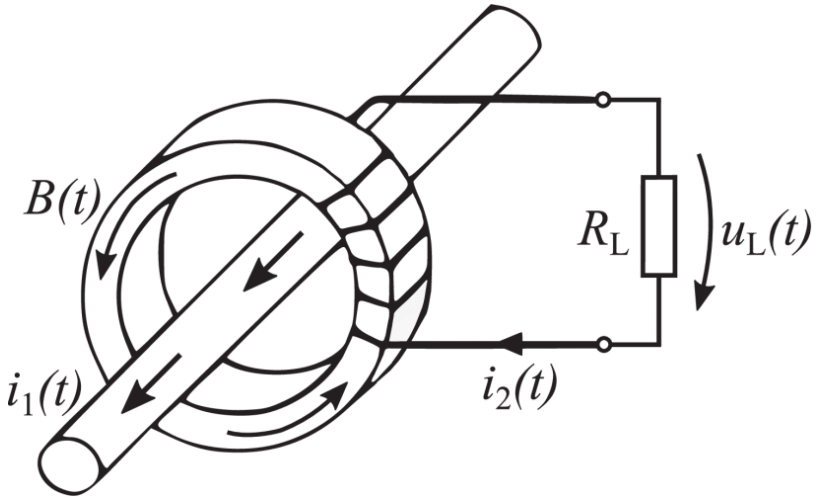

Figure 7.2: Current transducer diagram [50].

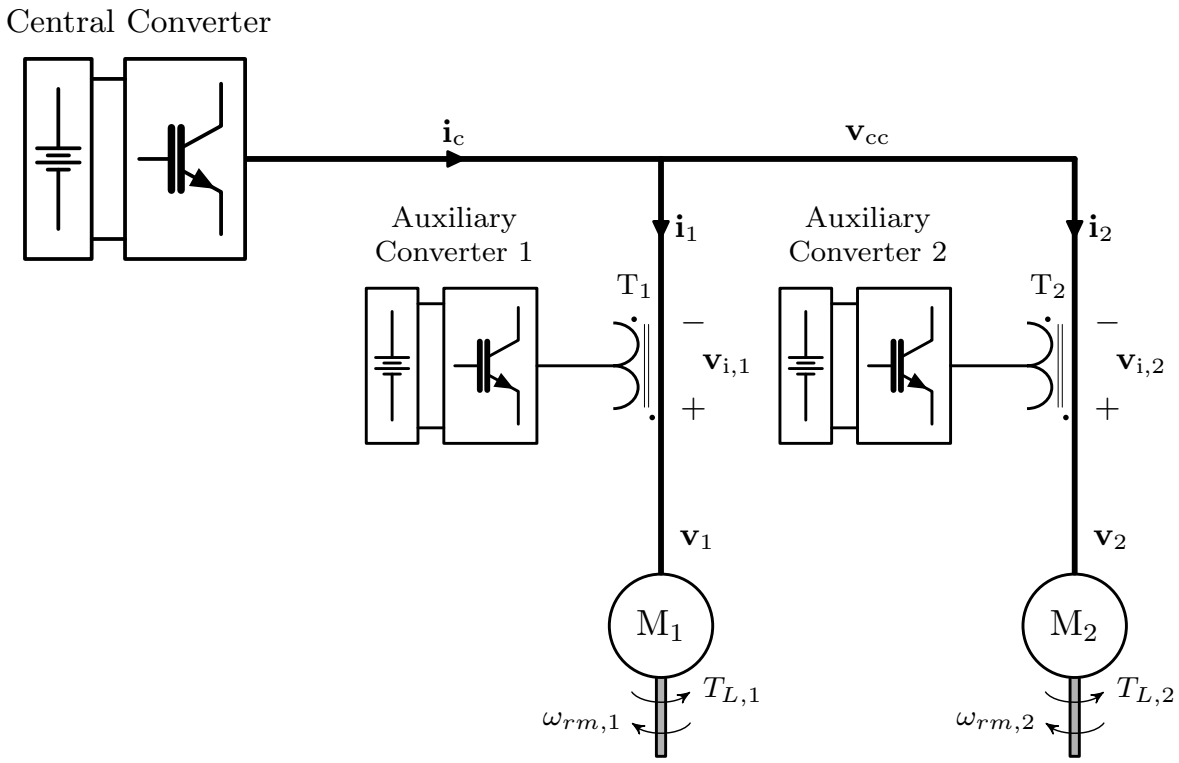

Figure 7.3: CCMM topology with voltage boost synchronization method.

tion of a balanced three-phase induction machine. The steady-state electromagnetic torque of the induction machine can be written as [52]:

$$T_e = \frac{3\frac{P}{2}\frac{\omega_e}{\omega_b}\frac{X_M^2}{\omega_b}r_r' s|\tilde{V}|^2}{\left(r_s r_r' + s\left(\frac{\omega_e}{\omega_b}\right)^2 (X_M^2 - X_s X_r')\right)^2 + \left(\frac{\omega_e}{\omega_b}\right)^2 (r_r' X_s + s r_s X_r')^2}, \tag{7.1}$$

where P is the number of magnetic poles of the machine, ω_e is the input electrical frequency, ω_b is the rated or base frequency of the machine, $|\tilde{V}|$ is the rms magnitude of stator voltage phasor, $X_M := \omega_b L_M$, $X_s := \omega_b L_s$, $X_r' := \omega_b L_r'$ are the machine reactances and L_M, L_s, and L_r' are the machine magnetizing, self-stator, and (stator referred) self-rotor inductances, respectively, r_s and r_r' are the stator and (stator referred) rotor resistance, respectively, and $s := {}^{(\omega_e - \omega_r)}/_{\omega_e}$ is the slip.

Fig. 7.4 shows the electromagnetic torque vs. (normalized) speed of a 15 hp machine (parameters in Table A.1), for different stator terminal voltage magnitudes, $|\tilde{V}|$. An arbitrary load torque curve is also depicted in Fig. 7.4. In steady-state, the operation speed corresponds to the intersection of the machine and the load torque curves. As shown in Fig. 7.4, decreasing the terminal voltage amplitude flattens the steady-state electromagnetic torque curve of the machine. The intersection points move to the left as the voltage decreases, resulting in a speed reduction.

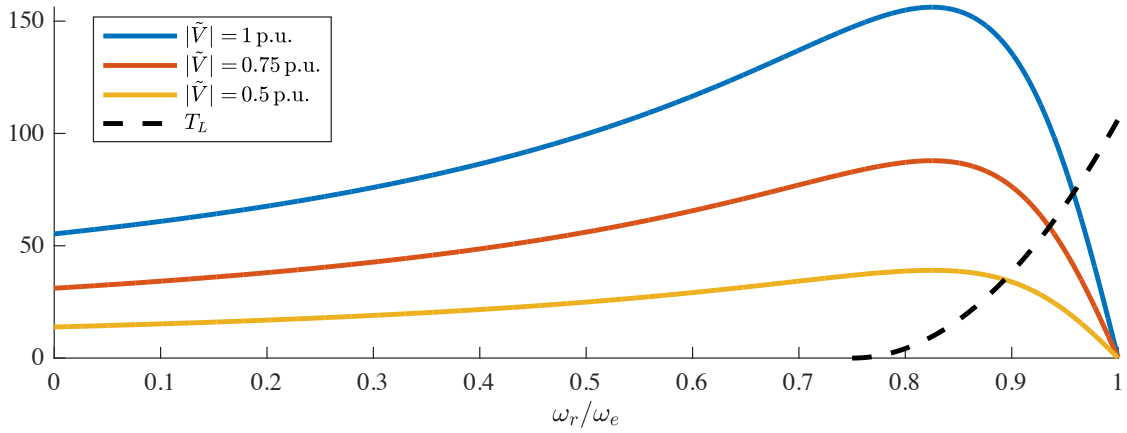

Figure 7.4: Electromagnetic torque vs. (normalized) speed of an induction machine for different amplitude values of stator voltage.

Assuming two induction machines with identical parameters, from (7.1) it can be shown that, to achieve steady-state speed synchronization between the two machines, the following relationship has to hold:

$$|\tilde{V}_1| = |\tilde{V}_2|\sqrt{\frac{T_{L,1}}{T_{L,2}}}, \tag{7.2}$$

where $|\tilde{V}_1|$ and $|\tilde{V}_2|$ are the rms magnitudes of the stator terminal voltages of motors 1 and 2, respectively.

Let us assume a balanced steady-state operation, which can be represented by phasors. In that case, the voltages $\mathbf{v}_{\text{cc}}$, $\mathbf{v}_1$, $\mathbf{v}_2$, $\mathbf{v}_{\text{i},1}$, and $\mathbf{v}_{\text{i},2}$ can be replaced with their corresponding phasors $\tilde{V}_{\text{cc}}$, $\tilde{V}_1$, $\tilde{V}_2$, $\tilde{V}_{\text{i},1}$, and $\tilde{V}_{\text{i},2}$, respectively, arbitrarily choosing phase-a phasor. Another assumption is that all the voltage phasors have the same electrical frequency and are in phase. The steady-state speed synchronization can be achieved for any [1] load torque difference by independently manipulating the two terminal voltages $\tilde{V}_1$ and $\tilde{V}_2$.

From Fig. 7.3, there are three available variables that can be independently varied, $\mathbf{v}_{\text{cc}}$, $\mathbf{v}_{\text{i},1}$, and $\mathbf{v}_{\text{i},2}$. Since only two variables are required to be independently controlled, there is one extra degree of freedom. Therefore, one of the variables can be eliminated from the system and still guarantee speed synchronization. For instance, one of the induced voltages (say, $\tilde{V}_{\text{i},1}$) can be set to zero (by removing the auxiliary converter and the transformer corresponding to the first machine). The system simplifies to $\tilde{V}_1 = \tilde{V}_{\text{cc}}$ and $\tilde{V}_2 = \tilde{V}_{\text{cc}} + \tilde{V}_{\text{i},2}$. By controlling $\tilde{V}_{\text{cc}}$ and $\tilde{V}_{\text{i},2}$, the relationship in (7.2) can still be held. In this case, machine 1 would be assigned as the primary, while machine 2 would be the secondary. The central converter would have machine 1 as its control target, and the position synchronization device would be responsible for fine-tuning the rotor position of machine 2.

Using a PI control to illustrate the method, the control law to ensure position synchronization under the conditions described in the previous paragraph would be:

[1] As long as neither load torque is zero and as long as they both have the same sign, either both positive or either both negative.

$$|\tilde{V}_{i,2}| = K_P \delta\theta_{rm,12} + K_I \int \delta\theta_{rm,12}\,\mathrm{d}t, \tag{7.3}$$

$$\delta\theta_{rm,12} = \theta_{rm,1} - \theta_{rm,2} \tag{7.4}$$

where K_P and K_I are the voltage-boost proportional and integral gains, respectively, and $\delta\theta_{rm,12}$ is the rotor position difference between machines 1 and 2. In case machine 2 is faster than machine 1 (assuming motor operation), $\delta\theta_{rm,12}$ tends to be negative, resulting in a negative induced voltage $|\tilde{V}_{i,2}|$. In turn, this will result in a lower terminal voltage on machine 2 compared to machine 1, leading to a speed reduction in machine 2 (c.f. Fig. 7.4). The induced voltage amplitude, $|\tilde{V}_{i,2}|$, is applied to all three phases, and they have the same electrical frequency and angular position as the central converter output voltages.

In terms of practical implementation, the voltage-boost method presents a couple of advantages compared to the "controllable stator resistors" method. Since the voltage-boost method is based on induced voltages using transformers, there is galvanic insulation between the main circuit of the motors and the auxiliary converters, which adds one extra layer of protection to the system. This also means that the main circuit does not have to be opened or broken for the installation of the required devices. By using the same principle as of a clamp current transducer, it is possible to deploy the required synchronization devices to existing systems, by just clamping the magnetic core to the machines wires. The switches of the auxiliary converter have to handle a scaled-down version of the machine currents, and the scale factor can be adjusted by the number of turns on the primary. Both positive and negative induced voltages can be achieved, which presents the system with additional flexibility and range of operation. In fact, this is the reason why one of the auxiliary converters can be eliminated from the setup shown in Fig. 7.3. By eliminating the first machine auxiliary converter, it is still possible to achieve a lower terminal voltage $\tilde{V}_2$ by inducing a negative voltage. Finally, the proposed method does not impose any limitations when working in the generator mode, as long as both machines are in the same region.

However, there are also some challenges to the practical implementation. The auxiliary converters have to be synchronized with the main converter to ensure frequency and phase alignment. The transformer has to be designed to guarantee the required typical induced voltage levels necessary to ensure the speed synchronization relationship in (7.2). Real transformers impose voltage drops in both the primary and secondary circuits, which can present an additional complexity to the induced voltage control. There is a need for a DC voltage source to power the auxiliary converters. This can become critical if the turns ratio of the transformer is increased. Although the primary current is scaled down by the turns ratio, the primary voltage is scaled up. Depending on the necessary induced voltage, the primary voltage can reach impractical values. However, by thoroughly analyzing the system and anticipating the required induced voltage levels for the expected load torques distribution, custom-made transformers and auxiliary converters can be properly designed to comply with the control demands. Moreover, this design process can also take into account that the same DC voltage that powers the main converter can be used as the DC voltage link for the auxiliary converter.

7.2 Voltage-Boost Method Validation

This section describes case studies used to evaluate the response of the voltage-boost synchronization method. The main purpose is to provide a proof-of-concept of the method and compare its response with the results presented in Chapter 5 under the same operation conditions. In the following case studies, the central converter was modeled as an ideal six-switch, four-quadrant inverter. The voltage-boost device comprises a three-phase inverter (identical to the central converter) and an ideal three-phase transformer. The secondary of the three-phase transformer was connected in series with the respective secondary machine line, while the primary was powered by the three-phase inverter. The gains of the position synchronization PI controller were: $K_P = 0.9$ and $K_I = 3.0$. All the system's remaining parameters can be found in the Appendix A. For the purpose of assessing the method performance, convergency criteria were defined as follows: secondary machine speeds are within 1 rpm difference of the primary machine, and rotor position

difference is below $0.25°$. All the time-domain simulations were performed using MATLAB®, version 2023b.

7.2.1 Case Study I: Constant Equally Spaced Load Torques

The first case study is as follows. Three 15 hp induction machines with identical parameters are connected in parallel with the central-converter. Voltage-boost elements are inserted in machines 2 and 3. The first machine is assigned as the primary, while the other two are the secondary machines. The central converter uses a voltage-control strategy (CVHz) to control the primary motor speed. The commanded speed was a ramp starting at 0 rpm applied from 0.1 s to 2.1 s until 1800 rpm, at no-load condition. After the machines have reached steady-state, an uneven load distribution is applied to the machines, as follows: $T_{L,1} = 1.0$ p.u., $T_{L,2} = 0.8$ p.u., and $T_{L,3} = 0.7$ p.u. This set-up condition is identical to the one presented in Section 5.1.1, so that the two methods can be compared under the same conditions. The results are presented in Fig. 7.5-7.9.

Fig. 7.5 shows the speed response of the three machines, while Fig. 7.6 shows a zoom-in view of the response at the application of the uneven load torque distribution. As can be seen, the machines' speeds ramp up following the commanded speed and settle at 1800 rpm at around 2.5 s. At that point, the unbalanced load torque distribution is applied. Following the load torque application, there is a noticeable speed difference among the machines, as the primary machine speed is corrected by the CVHz control. At the same time, the position synchronization control works to synchronize the machines' rotor positions, leading to a consequent speed synchronization, which can be observed after about 0.9 s.

Fig. 7.7 shows the rotor position differences of each secondary machine with respect to the primary machine. The higher the load torque difference with respect to the primary machine, the higher the peak error and the settling time. In fact, using the convergency definition described above, the settling times were 0.69 s and 0.74 s for machines 2 and 3, respectively, while the peak differences were $6.5°$ and $10.2°$.

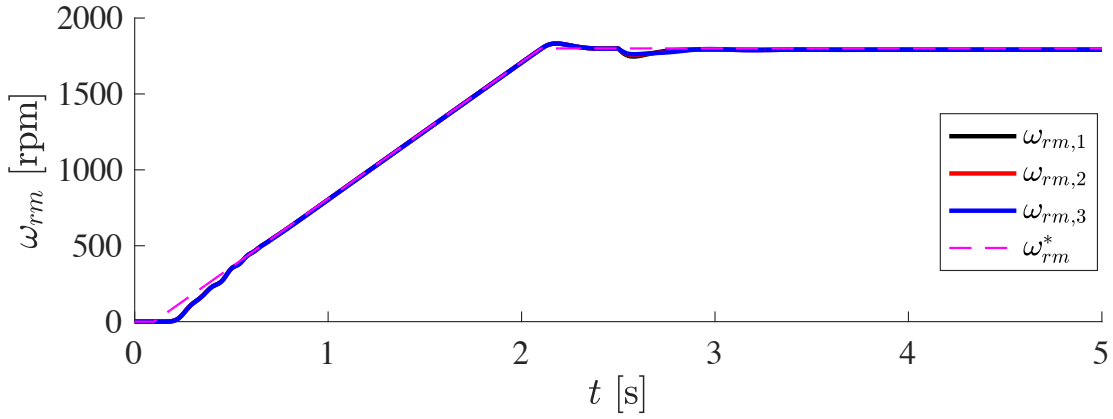

Figure 7.5: Speed response of the three machines along with commanded speed.

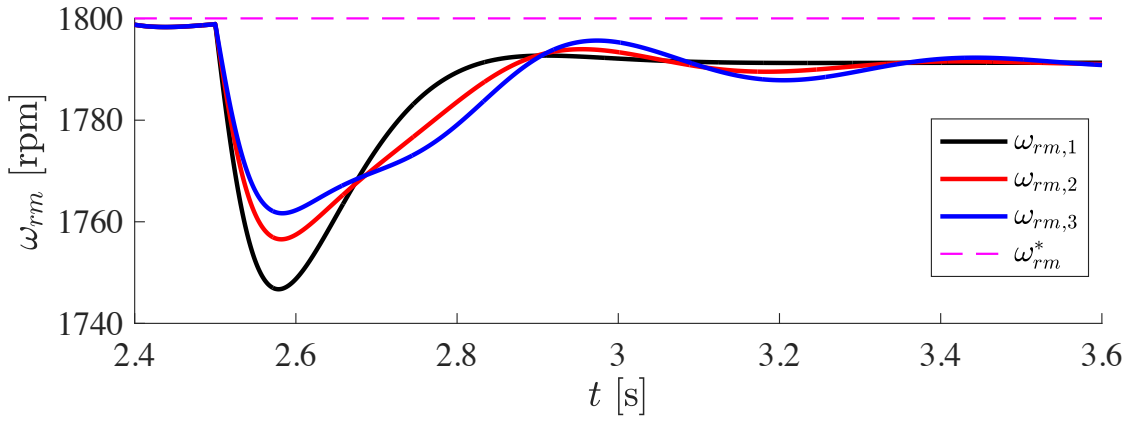

Figure 7.6: Speed response of the three machines along with commanded speed; zoom-in view.

Fig. 7.8 shows the rotor position normed difference. The peak error was $12.1°$, with settling time equal to 0.75 s.

Fig. 7.9 shows the magnitude of the induced voltage in each of the secondary machines. Since the voltage-boost method applies a balanced set of 3-phase voltages, all three phases have the same magnitude. Moreover, the induced voltages are in phase with the central converter output voltage. As expected, machine 3 requires the highest induced voltage to attain position synchronization since it presents a 30% of load torque difference with respect to the primary machine, versus 20% for machine 2. The steady-state values are 20.6 V and 32.0 V for machines 2 and 3, respectively,

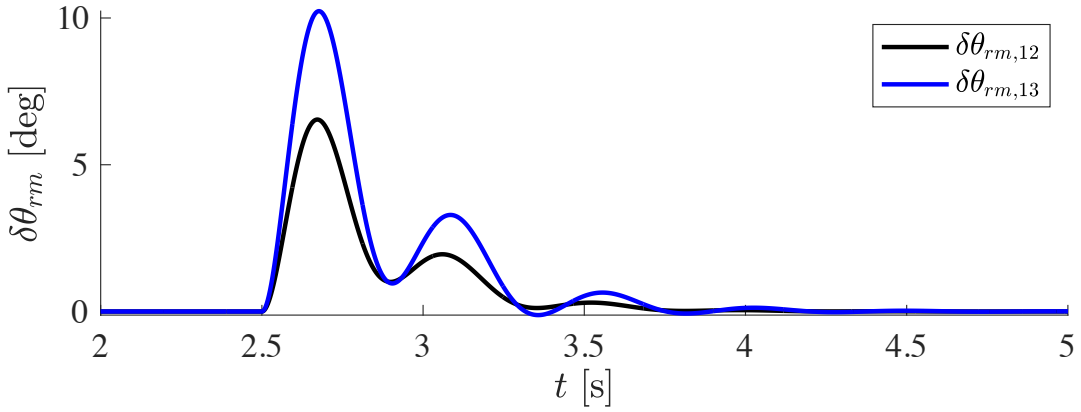

Figure 7.7: Rotor position differences of the secondary machines with respect to the primary machine.

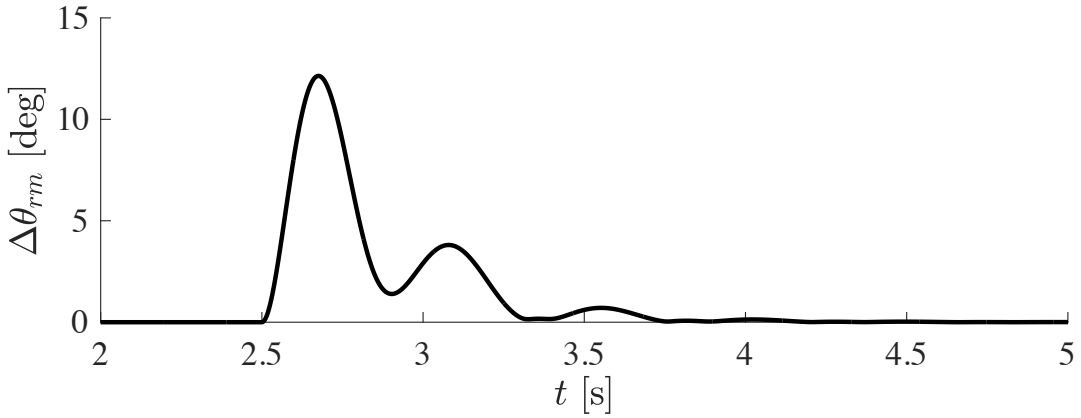

Figure 7.8: Normed position difference.

which corresponds to 11% and 16% of the rated voltage, respectively. Accordingly to (7.2), the theoretical values should be:

$$|\tilde{V}_{i,2}| = 1 - \sqrt{\frac{T_{L,2}}{T_{L,1}}} = 1 - \sqrt{\frac{0.8}{1.0}} \approx 0.1056\,\text{p.u.} \tag{7.5a}$$

$$|\tilde{V}_{i,3}| = 1 - \sqrt{\frac{T_{L,3}}{T_{L,1}}} = 1 - \sqrt{\frac{0.7}{1.0}} \approx 0.1633\,\text{p.u.}. \tag{7.5b}$$

which corresponds to the results obtained from the simulations. The maximum voltage magnitudes required during the transient were 27.3 V (14%) and 43.1 V (22%) for machines 2 and 3, respectively. Under these conditions, a transformer with a 5:1 ratio would meet these voltage requirements, in case the same central converter DC link was to be used for the synchronization converters. Therefore, the current levels observed in the secondary of the transformer would be only about 20% of the motor currents.

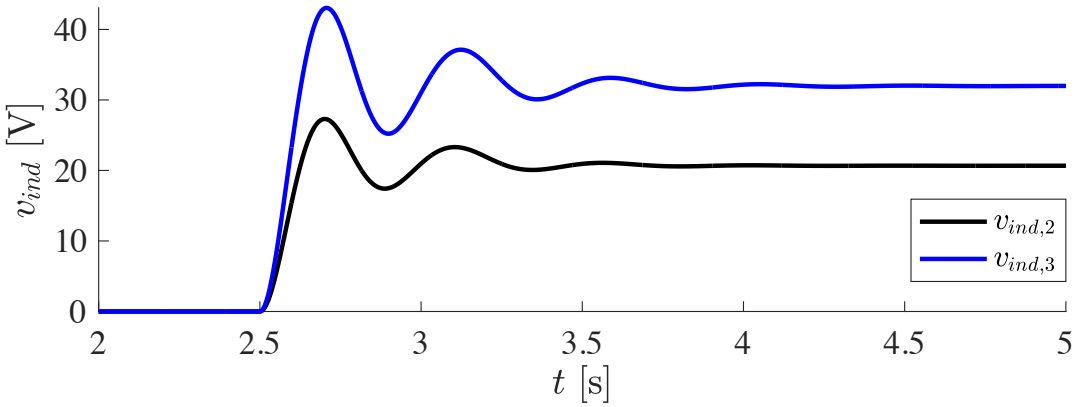

Figure 7.9: Induced voltage magnitudes in each of the secondary machines.

In comparison to the results shown in Chapter 5 the voltage-boost method showed some improvements. For the CVHz control strategy, the peak normed position error was $25.7°$ using the external resistance with PI control and $7.1°$ using external resistance with $\mathcal{H}_\infty$ control, while the voltage-boost method produced a peak normed position error of $12.1°$ using a PI control, a 53% reduction comparing to external resistance method and PI control. In terms of settling time, the observed values were 2.4 s (external resistance and PI), 1.2 s (external resistance and $\mathcal{H}_\infty$ control), and 0.8 s for the voltage-boost method, which demonstrates a significant improvement in the convergency speed. Although the peak error for the proposed method is still higher than the $\mathcal{H}_\infty$ optimal control observed using the external resistance method, there is room for improving the voltage-boost method by optimizing the controller structure.

7.2.2 Case Study II: TRAS Load Torque

For the second case study, time-variant load torques were applied to the induction machines. The load torque profile was based on a typical TRAS force vs. position profile, similar to the one presented in Section 6.2.1, Fig. 6.9b. In this case study, two 15 hp induction machines were used. The voltage boost method was applied to machine 1, while machine 2 was set as the primary, being controlled by the central converter using the CVHz speed control. Fig. 7.10 shows the speed profile commanded by the central converter, which corresponds to half a cycle of a typical TRAS operation.

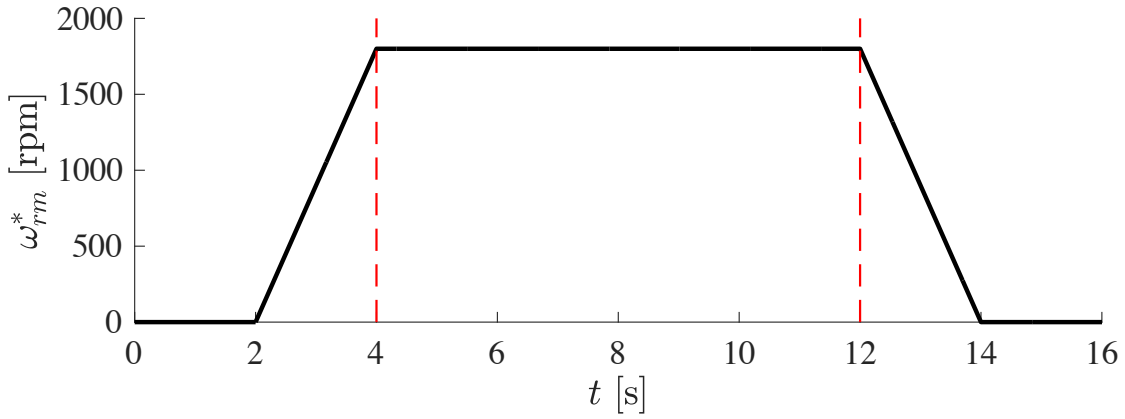

Figure 7.10: Speed profile..

Fig. 7.11 shows the load torques as a function of the percentual rotor position. The final position value, corresponding to 100 % in Fig. 7.11, was defined as the accumulated position displacement for the speed profile given in Fig. 7.10. More specifically:

$$\theta_{rm}(t_{end}) = \int_0^{t_{end}} \omega^*_{rm}(t)\,\mathrm{d}t = 10 \times 1800 \times \frac{\pi}{30} \approx 1,885\,rad. \tag{7.6}$$

To avoid an unstable operation when the machines are decelerating, the load torques were forced to zero for any θ_{rm} equal or above 100 %.

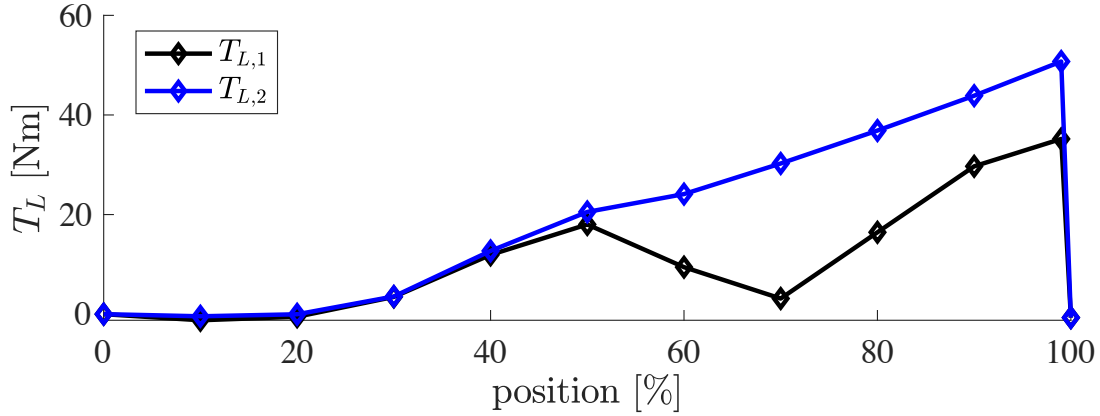

Figure 7.11: Load torque profile as a function of the rotor position.

The results are shown in Fig. 7.12 -7.16. In Fig. 7.12, the rotor position difference between the two machines is presented. The maximum peak errors were 7.6° on the positive portion and -15.0° on the negative. The dynamic response is a function of the time-variant load torques applied to the machines. The position synchronization method controlled the machines in a stable manner and managed to keep the position error within an acceptable range.

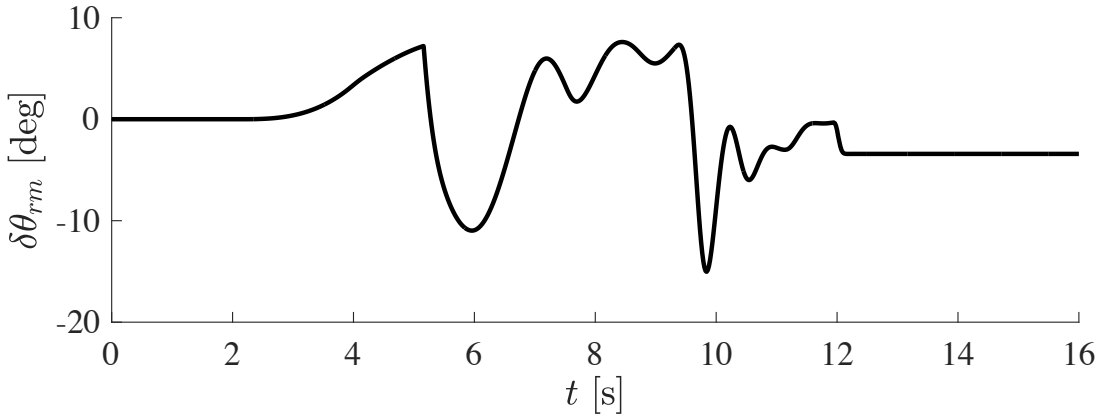

Figure 7.12: Rotor position difference between machines 1 and 2.

Fig 7.13 shows the magnitude of the induced voltage on machine 1. The maximum values were 142.6 V (73 %) on the positive portion and -31.8 V (16 %) on the negative. Despite the high peak in the demanded induced voltage, the duration of these higher values was short (around 1 s).

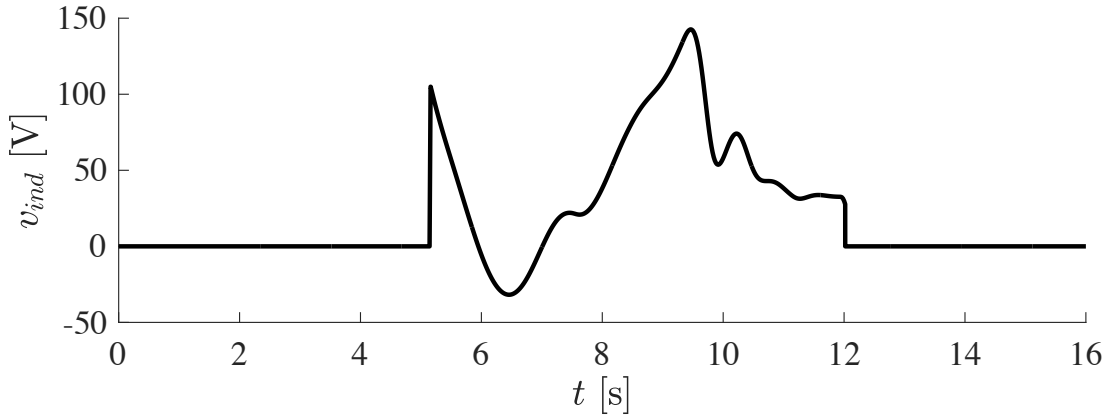

Figure 7.13: Induced voltage on machine 1.

Fig 7.14 shows the speed response of the two machines along with the commanded speed, and Fig 7.15 shows a zoom-in view focusing on the constant speed portion. The two machines followed the reference speed closely. Machine 2, being the primary, stays closer to the commanded speed, while machine 1 oscillates around it, a direct effect of the position synchronization control.

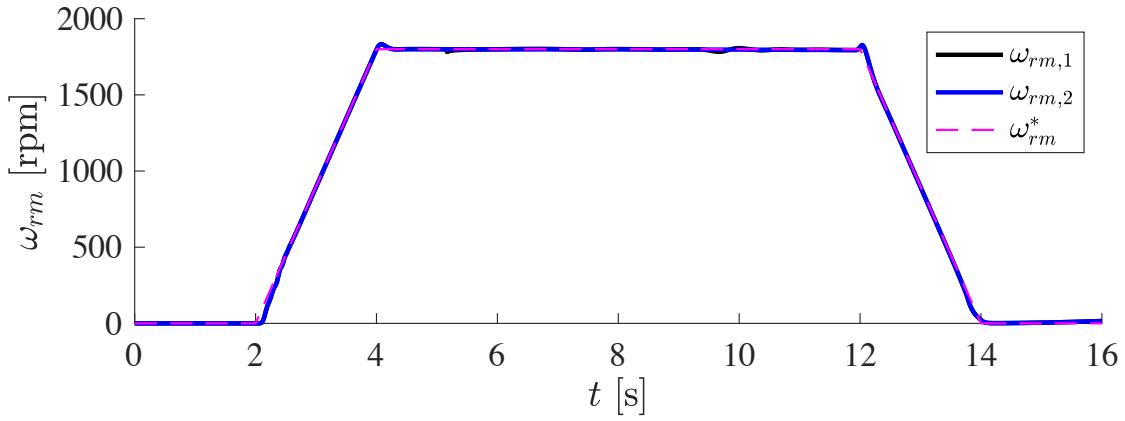

Figure 7.14: Speed response of the two machines along with commanded speed.

Fig 7.16 presents the load torque applied to each machine, as a function of time. The resemblance with Fig 7.11 is evident, showing that the load torques followed the desired profile with the rotor position increase.

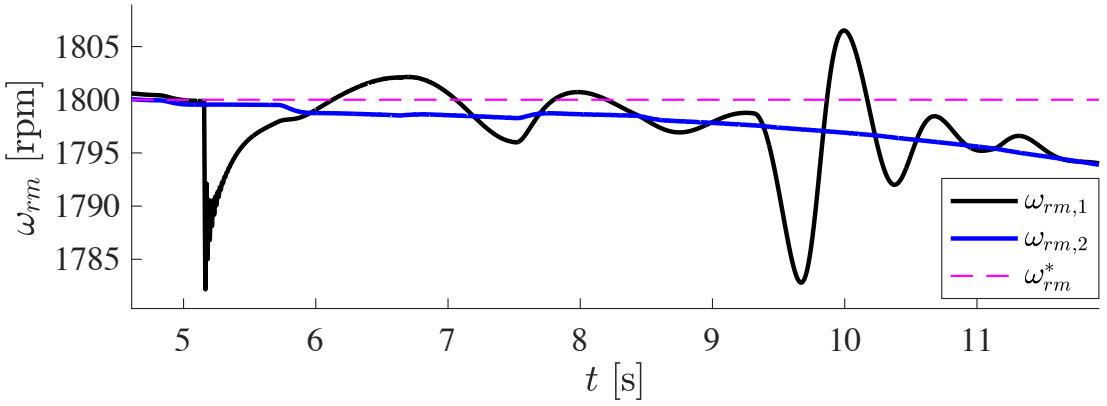

Figure 7.15: Speed response of the two machines along with commanded speed; zoom-in view.

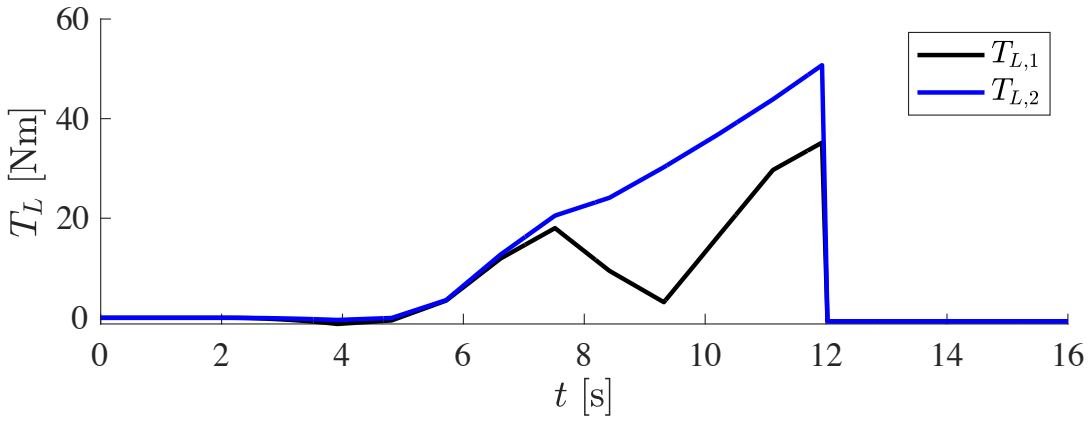

Figure 7.16: Load torque seen by the two machines.

Chapter 8

Conclusions and Future Work

In this dissertation, a control methodology was described to achieve rotor position synchronization in CCMM drives with parallel IMs acting as the actuation motors. Since all of the actuation motors in a CCMM architecture are connected to the central converter in parallel, independent position control was achieved by feedback control of external variable resistors in series with the IM stator windings. The change in total stator resistance of the motors was shown to alter the effective input impedance of the motors, as seen by the converter, in addition to their electromagnetic torque versus speed profile. This ability to alter the electromagnetic torque profile as a function of external stator resistance was used to provide independent adjustment of motor speeds, enabling fine rotor position synchronization through the use of feedback control.

In addition to its simplicity, a benefit of the proposed position control methodology is that it can be combined with supervisory speed control strategies. In particular, the approach was demonstrated in time-domain numerical case studies using two well-known voltage- and current-control strategies: Compensated Voltz-per-Hertz and Indirect Field-Oriented Control, respectively. Although the change in external stator resistance results in a potential decrease in maximum torque provided by the motors, an additional case study illustrated how the feedback control automatically accommodates increases in applied load torque to ensure sufficient torque production (up to the torque rating of the machine).

The results of these initial case studies indicated that continued refinement of the proposed approach may provide a promising solution for EM-TRAS applications. That served as a motivation to apply optimal control design to linearized IM models. Minimization of the $\mathcal{H}_\infty$ norm with defined control variables and noisy measurement signals was used to determine the weighted modified plant representation. The performance of the optimized controller was validated in time-domain simulation with the central converter in both voltage- and current-control modes (CVHz and IDFOC, respectively). Primary findings were that control performance in terms of maximum

and normed position errors was improved compared to the non-optimal PI control, at the expense of marginally larger required external resistance. Using the proposed controller for the resistor circuits, when the central converter also employed an IDFOC primary control strategy, performance was found to be superior in terms of peak relative and normed position errors, smaller required external resistance, and shorter settling time compared to the use of a CVHz primary control strategy.

Potential drawbacks of the proposed control (beyond higher external resistance) are (*i*) complexity of the control design and (*ii*) energy dissipation in the external stator resistance element to achieve synchronization.

This dissertation also described the requirements, conceptual design, and implementation of a new testbed for performing experiments to validate electromechanical actuation system designs for aircraft. High-level system requirements were presented and a detailed description of each hardware subsystem and their component interactions to achieve the requirements were presented. Also described were the testbed supervisory control, data acquisition, and several safety features. Experimental results were presented, demonstrating the use of the testbed to emulate an EM-TRAS deploy and stow operation. The "controllable stator resistors" method was also tested using the testbed, under different case studies. Both numerical simulations and experimental results are in agreement, demonstrating the ability of the position synchronization method to synchronize up to four induction machines under uneven load torques.

An alternative position synchronization method referred to as the "voltage-boost" method was presented and described, as an alternative to the "controllable stator resistors" method. Its main characteristics are the non-invasive deployment, low-power converter and compact three-phase transformer, galvanic insulation from the machine's power cables, and flexibility to achieve both positive and negative actuation signals. Using numerical simulations, initial findings show the ability of the method to achieve position synchronization under different conditions, and to present the same – and, in some cases, even better – performance than the previous solutions.

8.1 Future Work

Future work (currently underway) will further explore the "voltage-boost" method. $\mathcal{H}_\infty$ control design will be applied to this alternative method to obtain an optimal controller, and simulation results will be compared with the resistive method. Studies on the physical design of the method's device components, specifically the compact three-phase transformer, will be conducted. The performance of the method will be assessed when using a non-ideal transformer, and the impacts of the transformer's internal impedances voltage drops will be evaluated.

The testbed can be used in its current form, or with minor modifications, to perform experimental validation of electromechanical drive alternatives and advanced control strategies for a variety of aerospace actuation problems. For example, future work will use the testbed to validate the "voltage-boost" method proposed in this work. Given that the testbed can emulate mechanical anomalies, such as jamming, other lines of investigation consist of how electronic position synchronization methods perform compared to traditional position synchronization solutions (e.g. synchronization shafts) under fault conditions.

Bibliography

[1] J. Rosero, J. Ortega, E. Aldabas, and L. Romeral, "Moving towards a more electric aircraft," *IEEE Aerospace and Electronic Systems Magazine*, vol. 22, no. 3, pp. 3–9, 2007.

[2] A. Barzkar and M. Ghassemi, "Electric power systems in more and all electric aircraft: A review," *IEEE Access*, vol. Vol. 8, pp. 169 314–169 332, 2020.

[3] P. Wheeler and S. Bozhko, "The more electric aircraft: Technology and challenges." *IEEE Electrification Magazine*, vol. 2, no. 4, pp. 6–12, 2014.

[4] K. Ni, Y. Liu, Z. Mei, T. Wu, Y. Hu, H. Wen, and Y. Wang, "Electrical and electronic technologies in more-electric aircraft: A review," *IEEE Access*, vol. 7, pp. 76 145–76 166, 2019.

[5] X. Roboam, B. Sareni, and A. D. Andrade, "More electricity in the air: Toward optimized electrical networks embedded in more-electrical aircraft," *IEEE Industrial Electronics Magazine*, vol. 6, no. 4, pp. 6–17, 2012.

[6] K. Emadi and M. Ehsani, "Aircraft power systems: technology, state of the art, and future trends," *IEEE Aerospace and Electronic Systems Magazine*, vol. 15, no. 1, pp. 28–32, 2000.

[7] A. AbdElhafez and A. Forsyth, "A review of more-electric aircraft," in *International Conference on Aerospace Sciences and Aviation Technology*, vol. 13, no. AEROSPACE SCIENCES & AVIATION TECHNOLOGY, ASAT-13, May 26–28, 2009. The Military Technical College, 2009, pp. 1–13.

[8] O. Bennouna and N. Langlois, "Modeling and simulation of electromechanical actuators for aircraft nacelles," in *2013 9th International Symposium on Mechatronics and its Applications (ISMA)*, 2013, pp. 1–5.

[9] A. Debiane, J. Daclat, R. Denis, G. Dauphin-Tanguy, and J. Mare, "Presage: Virtual testing platform application to thrust reverser actuation system," in *3rd International Conference on Systems and Control*, 2013, pp. 1127–1133.

[10] D. Grasselt and K. Höschler, "Safety assessment of aero engine thrust reverser actuation systems," in *22nd International Symposium on Air Breathing Engines (ISABE-2015)*, 2015. [Online]. Available: http://hdl.handle.net/2374.UC/745815

[11] G. Zames, "Feedback and optimal sensitivity: Model reference transformations, multiplicative seminorms, and approximate inverses," *IEEE Transactions on automatic control*, vol. 26, no. 2, pp. 301–320, 1981.

[12] C. d. A. Lima, J. Cale, and K. E. Shahroudi, "Rotor position synchronization in central-converter multi-motor electric actuation systems," *Energies*, vol. 14, no. 22, 2021. [Online]. Available: https://www.mdpi.com/1996-1073/14/22/7485

[13] C. Lima, Z. Miller, R. Bushue, V. Kapoor, D. Neitenbach, C. Lute, J. Cale, and K. E. Shahroudi, "Testbed for emulation of aerospace actuation systems," in *Pipeline Research Council International (PRCI) Meeting*, Fort Collins, CO (USA), May 10 2022.

[14] C. Lima and J. Cale, "Rotor position synchronization control in central-converter multi-motor topologies," in *IEEE Power and Energy Systems General Meeting, 2022*, Denver, CO (USA), July 17–21 2022.

[15] C. Lima, Z. Miller, A. Riley, C. Lute, R. Bushue, B. Chan, M. Susman, A. Santos, S. Madcadi, J. Cale, and K. E. Shahroudi, "A novel electromechanical actuation testbed for emulation of aerospace actuation systems," in *33rd Aerospace Testing Seminar*, El Segundo, CA (USA), May 15 2023.

[16] C. Lima and J. Cale, "Control design for position synchronization in central converter multi-machine actuators," in *Proc. of the International Conference on Electrical, Computer, Communications and Mechatronics Engineering (ICECCME 2023)*, Tenerife, Spain, July 19–21 2023.

[17] P. M. Kelecy and R. D. Lorenz, "Control methodology for single inverter, parallel connected dual induction motor drives for electric vehicles," in *Proceedings of 1994 Power Electronics Specialist Conference-PESC'94*, vol. 2. IEEE, 1994, pp. 987–991.

[18] K. Matsuse, H. Kawai, Y. Kouno, and J. Oikawa, "Characteristics of speed sensorless vector controlled dual induction motor drive connected in parallel fed by a single inverter," *IEEE Transactions on Industry Applications*, vol. 40, no. 1, pp. 153–161, 2004.

[19] P. Ghani, M. Arasteh, and H. R. Tayebi, "Analysis of electromechanical model of traction system with single inverter dual induction motor," in *2016 7th Power Electronics and Drive Systems Technologies Conference (PEDSTC)*. IEEE, 2016, pp. 99–104.

[20] B. M. Joshi and M. C. Chandorkar, "Two-motor single-inverter field-oriented induction machine drive dynamic performance," *Sadhana*, vol. 39, no. 2, pp. 391–407, 2014.

[21] M. Jafari, K. Abbaszadeh, and M. Mohamadian, Mustafa, "A novel dtc-svm approach for two parallel-connected induction motors fed by matrix converter," *Turkish Journal of Electrical Engineering & Computer Sciences*, vol. 26, no. 3, pp. 1599–1611, 2018.

[22] R. Gunabalan and V. Subbiah, "Speed -sensorless vector control of parallel connected induction motor drive fed by a single inverter using natural observer," *International Journal of Electrical and Computer Engineering*, vol. 4, no. 8, pp. 1193 – 1198, 2010. [Online]. Available: http://waset.org/Publications?p=44

[23] R. Gunabalan, P. Sanjeevikumar, F. Blaabjerg, O. Ojo, and V. Subbiah, "Analysis and implementation of parallel connected two-induction motor single-inverter drive by direct vector control for industrial application," *IEEE Transactions on Power Electronics*, vol. 30, no. 12, pp. 6472–6475, 2015.

[24] R. Gunabalan, V. Subbiah, and P. Sanjeevikumar, "Vector control of three-phase parallel connected two motor single inverter speed sensorless drive," *Turkish Journal of Electrical Engineering and Computer Sciences*, vol. 24, pp. 4027–4041, 06 2016.

[25] R. Gunabalan and V. Subbiah, "Single inverter fed speed sensorless vector control of parallel connected two motor drive," *Automatika*, vol. 57, no. 2, pp. 416–427, 2016. [Online]. Available: https://doi.org/10.7305/automatika.2016.10.1155

[26] R. Gunabalan, P. Sanjeevikumar, F. Blaabjerg, P. W. Wheeler, O. Ojo, and A. H. Ertas, "Speed sensorless vector control of parallel-connected three-phase two-motor single-inverter drive system," *FACETS*, vol. 1, no. 1, pp. 1–16, 2017.

[27] H. Kubota and K. Matsuse, "Speed sensorless field-oriented control of induction motor with rotor resistance adaptation," *IEEE Transactions on Industry Applications*, vol. 30, no. 5, pp. 1219–1224, 1994.

[28] H. Kubota, K. Matsuse, and T. Nakano, "Dsp-based speed adaptive flux observer of induction motor," *IEEE transactions on industry applications*, vol. 29, no. 2, pp. 344–348, 1993.

[29] M. A. Valenzuela and R. D. Lorenz, "Electronic line-shafting control for paper machine drives," *IEEE Transactions on Industry Applications*, vol. 37, no. 1, pp. 158–164, 2001.

[30] F. J. Perez-Pinal, C. Nunez, R. Alvarez, and I. Cervantes, "Comparison of multi-motor synchronization techniques," in *30th Annual Conference of IEEE Industrial Electronics Society, 2004. IECON 2004*, vol. 2, 2004, pp. 1670–1675 Vol. 2.

[31] F. J. Perez-Pinal, "Improvement of the electronic line-shafting," in *2004 IEEE 35th Annual Power Electronics Specialists Conference (IEEE Cat. No.04CH37551)*, vol. 5, 2004, pp. 3260–3265 Vol.5.

[32] F. J. Perez-Pinal, C. Nunez, and R. Alvarez, "A novel speed control approach in parallel-connected induction motor by using a single inverter and electronic virtual line-shafting," in *2005 IEEE 36th Power Electronics Specialists Conference*, 2005, pp. 1339–1345.

[33] F. J. Perez-Pinal, C. Nunez, and R. Alvarez, "Multi-motor synchronization technique applied in traction devices," in *IEEE International Conference on Electric Machines and Drives, 2005.* IEEE, 2005, pp. 1542–1548.

[34] E. A. Polcuch, "Near synchronous controlled induction motor drive actuation system," U.S. Patent 9,190,942 B2, Nov. 17, 2015.

[35] P. C. Krause, O. Wasynczuk, S. D. Sudhoff, and S. Pekarek, *Analysis of electric machinery and drive systems*. Wiley Online Library, 2002, vol. 2.

[36] P. Krein, *Elements of Power Electronics, 2nd. ed.* Oxford University Press, 2014, vol. 2.

[37] S. N. Vukosavic, *Digital control of electrical drives*. Springer Science & Business Media, 2007.

[38] G. K. Dubey, *Fundamentals of electrical drives*. Alpha Science Int'l Ltd., 2001.

[39] R. W. Erickson and D. Maksimovic, *Fundamentals of power electronics*. Springer Science & Business Media, 2007.

[40] N. Mohan, T. M. Undeland, and W. P. Robbins, *Power electronics: converters, applications, and design*. John wiley & sons, 2003.

[41] J. Gadewadikar, F. L. Lewis, K. Subbarao, K. Peng, and B. M. Chen, "H-infinity static output-feedback control for rotorcraft," *Journal of Intelligent and Robotic Systems*, vol. 54, no. 4, pp. 629–646, 2009. [Online]. Available: https://doi.org/10.1007/s10846-008-9279-5

[42] L. Song, J. Li, Z. Wei, K. Yang, E. Hashemi, and H. Wang, "Longitudinal and lateral control methods from single vehicle to autonomous platoon," *Green Energy and Intelligent Transportation*, p. 100066, 2023. [Online]. Available: https://www.sciencedirect.com/science/article/pii/S2773153723000026

[43] G. Willmann, D. F. Coutinho, L. F. A. Pereira, and F. B. Libano, "Multiple-loop h-infinity control design for uninterruptible power supplies," *IEEE Transactions on Industrial Electronics*, vol. 54, no. 3, pp. 1591–1602, 2007.

[44] M. Z. U. Rahman, V. Leiva, C. Martin-Barreiro, I. Mahmood, M. Usman, and M. Rizwan, "Fractional transformation-based intelligent h-infinity controller of a direct

current servo motor," *Fractal and Fractional*, vol. 7, no. 1, 2023. [Online]. Available: https://www.mdpi.com/2504-3110/7/1/29

[45] T. Roy and R. K. Barai, *Control-Oriented LFT Modelling and H-infinity Control of Differentially Driven Wheeled Mobile Robot*. Singapore: Springer Nature Singapore, 2023, pp. 111–133. [Online]. Available: https://doi.org/10.1007/978-981-19-7462-5_8

[46] J. Doyle and G. Stein, "Multivariable feedback design: Concepts for a classical/modern synthesis," *IEEE transactions on Automatic Control*, vol. 26, no. 1, pp. 4–16, 1981.

[47] S. Skogestad and I. Postlethwaite, *Multivariable feedback control: analysis and design*. John Wiley & Sons, 2005.

[48] J. Doyle, K. Glover, P. Khargonekar, and B. Francis, "State-space solutions to standard H_2 and H_∞ control problems," *IEEE Transactions on Automatic Control*, vol. 34, no. 8, pp. 831–847, 1989.

[49] P. C. Sen *et al.*, *Principles of electric machines and power electronics*. John Wiley & Sons, 2021.

[50] M. Fritsch and M. Wolter, "Saturation of high-frequency current transformers: Challenges and solutions," *IEEE Transactions on Instrumentation and Measurement*, vol. 72, pp. 1–10, 2023.

[51] J. C. Das and R. Mullikin, "Design and application of a low-ratio high-accuracy split-core core-balance current transformer," *IEEE Transactions on Industry Applications*, vol. 46, no. 5, pp. 1856–1865, 2010.

[52] P. Krause, O. Wasynczuk, and Sudhoff, *Analysis of Electric Machinery*. Hoboken, NJ: Wiley, IEEE Press, 1995.

Appendix A

Induction Machine and Control Parameters

Table A.1: Parameters for 15 hp Induction Machine.

Description	**Symbol**	**Value**
Machine poles	P	4
Rated torque	T_{rated}	61.1 [N·m]
Stator resistance	r_s	0.06 [Ω]
Rotor resistance (referred)	r'_r	0.15 [Ω]
Stator leakage inductance	$L_{\ell s}$	1.17 [mH]
Rotor leakage inductance (referred)	$L'_{\ell r}$	1.14 [mH]
Magnetizing inductance	L_M	33.4 [mH]
Windage and friction loss coefficient	B_m	5.41×10^{-4} [N·m·s]
Rotor inertia	J	0.45 [kg·m^2]

Table A.2: Parameters for Compensated Volts-per-Hertz Control.

Description	Symbol	Value
Low-pass filter time constant	τ_{LPF}	0.1 [s]
Slew-rate limiter minimum	$\alpha_{\min}$	- 75.4 [rad/s^2]
Slew-rate limiter maximum	$\alpha_{\max}$	75.4 [rad/s^2]
Base rotor speed	ω_b	377 [rad/s]
Base voltage (rms)	V_b	139 [V]
Converter DC input voltage	v_{dc}	339 [V]
PWM switching frequency	f_s	3 [kHz]

Table A.3: Parameters for Indirect Field-oriented Control.

Description	Symbol	Value
Torque limiter upper max	$T_{e,\max}$	$2T_{rated}$
Torque limiter lower max	$T_{e,\min}$	$-2T_{rated}$
Hysteresis band tolerance	h_b	0.1 [A]
Converter DC input voltage	v_{dc}	339 [V]

Table A.4: Parameters for Speed Control.

Description	Symbol	Value
Speed control proportional gain	K_{scp}	26.7 [N·m·s/rad]
Speed control integral gain	K_{sci}	8.33 [1/s]

Table A.5: Parameters for External Resistor Circuit and Control.

Description	**Symbol**	**Value**
Base resistance	r	2.0 [Ω]
PWM switching frequency	f_s	5 [kHz]

Table A.6: Parameters for External Resistor Proportional-Integral Control.

Description	**Symbol**	**Value**
Proportional gain	$K_{P,2}$	15 [Ω/rad]
Integral gain	$K_{I,2}$	30 [Ω/rad·s]
Proportional gain	$K_{P,3}$	15 [Ω/rad]
Integral gain	$K_{I,3}$	30 [Ω/rad·s]]

Table A.7: Optimal Controller Parameters

Description	**Values**
Poles [s^{-1}]	$-4557, -309.3, -87.17, -0.0728, -85.15 \pm j400, -38.12 \pm j189$
Zeros [s^{-1}]	$-27.37, -14.1, -6283, -26.1 \pm j372.5, -52.0 \pm j20.8$
DC Gain [(s·rad)$^{-1}$]	-3.321×10^7

Appendix B

Induction Machine Linearization Model

The full generalized plant model referred to in section 4.3 is represented as follows:

$$\widehat{\mathbf{P}} = \begin{bmatrix} \mathbf{A}_P & \mathbf{B}_{P,1} & \mathbf{B}_{P,2} \\ \mathbf{C}_{P,1} & \mathbf{D}_{P,11} & \mathbf{D}_{P,12} \\ \mathbf{C}_{P,2} & \mathbf{D}_{P,21} & \mathbf{D}_{P,22} \end{bmatrix} \tag{B.1}$$

$$\mathbf{A}_P = \begin{bmatrix} \mathbf{A} & \mathbf{0}_{6\times 6} \\ \mathbf{0}_{6\times 6} & \mathbf{A} \end{bmatrix}, \tag{B.2}$$

where $\mathbf{A}$ was defined in section 4.2.2, and:

$$\mathbf{B}_{P,1} = \begin{bmatrix} \mathbf{B}_{P,1a} & \mathbf{B}_{P,2a} \end{bmatrix}^T \tag{B.3}$$

$$\mathbf{B}_{P,1a} = \begin{bmatrix} 1 & 0 & 0 & 0 & 0 & 0 \\ 0 & 0 & 0 & 0 & -1/J' & 0 \\ 0 & 0 & 0 & 0 & 0 & 0 \\ 0 & 0 & 0 & 0 & 0 & 0 \end{bmatrix}^T \tag{B.4}$$

$$\mathbf{B}_{P,1b} = \begin{bmatrix} 1 & 0 & 0 & 0 & 0 & 0 \\ 0 & 0 & 0 & 0 & 0 & 0 \\ 0 & 0 & 0 & 0 & -1/J' & 0 \\ 0 & 0 & 0 & 0 & 0 & 0 \end{bmatrix}^T \tag{B.5}$$

$$\mathbf{B}_{P,2} = \begin{bmatrix} \mathbf{0}_{6\times 1} & \mathbf{B}_{P,2b} \end{bmatrix}^T, \tag{B.6}$$

where:

$$\mathbf{B}_{P,2b} = \begin{bmatrix} \left(\frac{L_M}{L_{rr}}\right)\lambda^e_{qr0} - \lambda^e_{qs0} & \left(\frac{L_M}{L_{rr}}\right)\lambda^e_{dr0} - \lambda^e_{ds0} & \mathbf{0}_{1\times 4} \end{bmatrix}^T \tag{B.7}$$

$$\mathbf{C}_{P,1} = \begin{bmatrix} \mathbf{0}_{1\times 5} & -\frac{2}{P} & \mathbf{0}_{1\times 5} & \frac{2}{P} \\ \mathbf{0}_{1\times 5} & 0 & \mathbf{0}_{1\times 5} & 0 \end{bmatrix} \tag{B.8}$$

$$\mathbf{C}_{P,2} = \begin{bmatrix} \mathbf{0}_{1\times 5} & -\frac{2}{P} & \mathbf{0}_{1\times 5} & \frac{2}{P} \end{bmatrix} \tag{B.9}$$

$$\mathbf{D}_{P,11} = \begin{bmatrix} \mathbf{0}_{2\times 4} \end{bmatrix}, \quad \mathbf{D}_{P,12} = \begin{bmatrix} 0 & 1 \end{bmatrix}^T \tag{B.10}$$

$$\mathbf{D}_{P,21} = \begin{bmatrix} 0 & 0 & 0 & 0 & 1 \end{bmatrix}^T, \quad \mathbf{D}_{P,22} = \begin{bmatrix} 0 \end{bmatrix}. \tag{B.11}$$